

# Naval Research Laboratory

Washington, DC 20375-5320



AD-A268 456



NRL/FR/8121--93-9537

## UVPI Imaging from the LACE Satellite: The Nihka Rocket Plume

H. W. SMATHERS AND D. M. HORAN

*Space Systems Development Department  
Naval Center for Space Technology*

J. G. CARDON AND E. R. MALARET

*Applied Coherent Technology Corporation  
Herndon, VA*

J. E. BRANDENBURG

*Research Support Instruments  
Alexandria, VA*

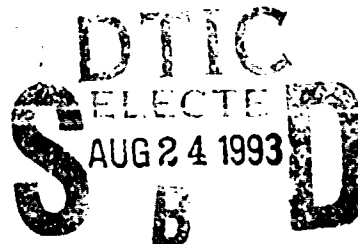
R. E. CAMPION

*AlliedSignal Technical Services Corporation  
Alexandria, VA*

R. R. STRUNCE, JR.

*Star Technologies Corporation  
Great Falls, VA*

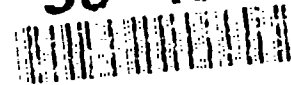
July 12, 1993



original contains color  
images; all DTIC reproductions  
will be in black and  
white

Approved for public release; distribution unlimited.

93-19524



93 8 23 01 7

# DISCLAIMER NOTICE



THIS DOCUMENT IS BEST QUALITY AVAILABLE. THE COPY FURNISHED TO DTIC CONTAINED A SIGNIFICANT NUMBER OF COLOR PAGES WHICH DO NOT REPRODUCE LEGIBLY ON BLACK AND WHITE MICROFICHE.

PAGES \_\_\_\_\_  
ARE  
MISSING  
IN  
ORIGINAL  
DOCUMENT

# REPORT DOCUMENTATION PAGE

Form Approved  
OMB No. 0704-0188

Public reporting burden for this collection of information is estimated to average 1 hour per response, including the time for reviewing instructions, searching existing data sources, gathering and maintaining the data needed, and completing and reviewing the collection of information. Send comments regarding this burden estimate or any other aspect of this collection of information, including suggestions for reducing this burden, to Washington Headquarters Services, Directorate for Information Operations and Reports, 1215 Jefferson Davis Highway, Suite 1204, Arlington, VA 22202-4302, and to the Office of Management and Budget, Paperwork Reduction Project (0704-0188), Washington, DC 20503.

1. AGENCY USE ONLY (Leave Blank)		2. REPORT DATE July 12, 1993		3. REPORT TYPE AND DATES COVERED Interim	
4. TITLE AND SUBTITLE UVPI Imaging from the LACE Satellite: The Nihka Rocket Plume				5. FUNDING NUMBERS PE - 63217C PMA - N1305	
6. AUTHOR(S) H.W. Smathers, D.M. Horan, J.G. Cardon, <sup>1</sup> E.R. Malaret, <sup>1</sup> J.E. Brandenburg, <sup>2</sup> R.E. Campion, <sup>3</sup> and R.R. Strunce, Jr. <sup>4</sup>					
7. PERFORMING ORGANIZATION NAME(S) AND ADDRESS(ES) Naval Research Laboratory Washington, DC 20375-5320				8. PERFORMING ORGANIZATION REPORT NUMBER NRL/FR/8121--93-9537	
9. SPONSORING/MONITORING AGENCY NAME(S) AND ADDRESS(ES) Strategic Defense Initiative Organization Washington, DC 20301-7100				10. SPONSORING/MONITORING AGENCY REPORT NUMBER	
11. SUPPLEMENTARY NOTES <sup>1</sup> Applied Coherent Technology Corp. <sup>3</sup> AlliedSignal Technical Services Corp. <sup>2</sup> Research Support Instruments <sup>4</sup> Star Technologies Corp.					
12a. DISTRIBUTION/AVAILABILITY STATEMENT Approved for public release; distribution unlimited.				12b. DISTRIBUTION CODE	
13. ABSTRACT (Maximum 200 words)  The Nihka flight was the first demonstration of the ability of the Ultraviolet Plume Instrument (UVPI), carried aboard the LACE (Low-power Atmospheric Compensation Experiment) satellite, to observe missiles in flight above the atmosphere. The UVPI is a small, plume-tracking instrument flown on the Naval Research Laboratory's LACE satellite, which was launched on 14 February 1990. The Nihka was launched from the Wallops Island Launch Facility in Virginia to coincide with a LACE pass. The two cameras of the UVPI were used to observe the Nihka in the ultraviolet. These cameras were a tracker camera, viewing over a relatively wide field and broad spectrum, and a plume camera that has a narrow field of view (0.180° by 0.135°) and can observe sources through any of four filters. A three-stage sounding rocket (called Black Brant X) was used for the test. The third stage, or Nihka, reached 190 km altitude and was successfully detected and tracked by the UVPI from a range of 448 to 463 km. The Nihka plume was successfully tracked for 3.23 seconds; 91 images of plume data (each 1/30 of a second) were acquired by using the first plume-camera filter in the 235 to 350 nm range.					
14. SUBJECT TERMS Nihka rocket Ultraviolet Plume Instrument UVPI LACE (Low-power Atmospheric Compensation Experiment) Rocket plume imaging				15. NUMBER OF PAGES 85	
				16. PRICE CODE	
17. SECURITY CLASSIFICATION OF REPORT UNCLASSIFIED	18. SECURITY CLASSIFICATION OF THIS PAGE UNCLASSIFIED	19. SECURITY CLASSIFICATION OF ABSTRACT UNCLASSIFIED	20. LIMITATION OF ABSTRACT UL		

# CONTENTS

EXECUTIVE SUMMARY.....	E-1
1.0 INTRODUCTION.....	1
1.1 Background.....	1
1.2 UVPI Capability.....	1
1.3 Scientific Objectives for UVPI.....	3
1.3.1 Radiometrics.....	3
1.3.2 Spatial Features.....	4
1.3.3 Temporal Features.....	4
1.3.4 Spectral Features.....	4
1.4 Experiment Concept.....	4
1.4.1 Nihka Description and Launch Plan.....	4
1.4.2 Radiometrics.....	5
2.0 NIHKA OBSERVATION.....	6
2.1 Trajectory and Vehicle Performance Data.....	7
2.2 Tracking and Pointing Performance Data.....	11
2.2.1 Mode Sequencing Overview.....	11
2.2.2 Tracker Servo Response.....	14
2.2.3 Tracker Jitter.....	16
3.0 EXTRACTION OF RADIOMETRIC QUANTITIES.....	17
3.1 Data Calibration Procedure.....	17
3.1.1 Statistical Discrimination Of Photoevents.....	18
3.2 Relation of Photoevents to Source Radiance.....	20
3.3 Peak Normalized Radiance Approximation.....	21
3.4 Reference Spectrum for Aluminum-Loaded Propellants.....	22
3.5 Use of the Reference Spectrum to Calculate a Scaling Constant.....	23
3.6 Centroid Wavelength Determination.....	24
3.7 Calculations of Radiance and Radiant Intensity.....	25
3.8 Summary of Radiometric Conversion Constants.....	25
4.0 PLUME DATA.....	26
4.1 Data Collection Interval.....	27
4.1.1 Description.....	27
4.1.2 Calibration Parameters.....	27
4.2 Intensity History Overview.....	27
4.3 Single Images.....	29
4.4 Composite Plume Camera Images and Contour Plots.....	30
4.5 Calibrated Tracker Camera Images.....	39
4.6 Error Analysis for Radiometric Observations.....	46
4.6.1 Error Resulting from Measurement Noise.....	46
4.6.2 Error in Gain Conversion Factor.....	47
4.6.3 Calculation of Total Error.....	47
4.7 Noise-Equivalent Radiance.....	49
5.0 SPATIAL FEATURES.....	50
5.1 Delineation of Plume Central and Outer Regions.....	50
5.2 Plume Extent and Point Spread Function.....	52
5.3 Comparison of Results to CHARM 1.3 Predictions.....	54
6.0 TEMPORAL FEATURES.....	58
6.1 Plume Camera Intensity Plots.....	58
6.2 Tracker Camera Intensity Plots.....	59
7.0 SPECTRAL ANALYSIS OF PLUMES.....	60
7.1 Observed Spectral Radiant Intensities.....	60
7.2 Discussion.....	61
8.0 ANOMALOUS EVENTS.....	61
8.1 Possible Earlier Explosion.....	61
8.2 Nihka Burnout Anomaly.....	62

## CONTENTS (cont'd)

9.0	SUMMARY AND CONCLUSIONS .....	65
9.1	Summary.....	65
9.2	Achievement of Objectives.....	66
9.2.1	General Objectives.....	66
9.2.2	Spatial Features.....	67
9.2.3	Temporal Features.....	67
9.2.4	Spectral Features.....	67
9.3	Conclusions.....	68
	ACKNOWLEDGMENTS.....	68
	REFERENCES.....	69
	APPENDIX A: Nihka Trajectory Parameters.....	71
	APPENDIX B: Telemetry Frames and Camera Parameters .....	77
	APPENDIX C: CHARM Input File for Nihka.....	81
	GLOSSARY.....	84

<b>Accession For</b>		<input checked="" type="checkbox"/>
RTIS GRA&I		<input type="checkbox"/>
DTIC TAB		<input type="checkbox"/>
Unannounced		
Justification		
By _____		
Distribution/		
Availability Codes		
Diet	A-1	Special

DTIC QUALITY INSPECTED 3

## FIGURES

1	Tracker camera: net quantum efficiency curve.....	2
2	Plume camera: net quantum efficiency curves.....	2
3	Black Brant X rocket.....	5
4	Ground trace of the LACE satellite on Nihka plume observation pass.....	6
5	Ground trace of rocket and projected field of view of UVPI tracker camera.....	7
6	Altitude and velocity vs time.....	9
7	Range vs time.....	9
8	Aspect angle vs time.....	9
9	Angle of attack vs time.....	10
10	Nihka thrust vs time.....	10
11	Orientation angle in UVPI tracker camera vs time.....	10
12	Track and mission modes vs frame.....	11
13	Frame vs time.....	12
14	Azimuth gimbal angles vs frame.....	12
15	Elevation gimbal angles vs frame.....	13
16	Block diagram of tracking sequence.....	13
17	Track gate/target size X vs frame.....	14
18	Track gate/target size Y vs frame.....	14
19	Gain coefficients vs frame.....	15
20	Tracker error response vs time.....	15
21	X and Y tracker errors vs frame.....	16
22	Y tracker error (TV lines) vs X tracker error (pixels).....	16
23	X and Y tracker errors vs time.....	17
24	Y tracker error vs X tracker error in microradians.....	17
25	Composite image using no statistical discrimination.....	19
26	Composite image using statistical discrimination.....	19
27	Emissivity curve for aluminum particles in rocket plumes.....	22
28	Assumed reference spectrum.....	23
29	Tracker and plume camera gain.....	28
30	Tracker and plume camera exposure times.....	28
31	Spectral radiant intensity, plume camera, central region.....	28
32	Spectral radiant intensity, plume camera, total.....	28
33	Spectral radiant intensity, tracker camera.....	28
34	Single unprocessed plume camera images of the Nihka plume.....	29
35	Single image of the Nihka plume.....	30
36	Plume camera image of ground-based beacon illustrating the point spread function.....	31
37	Plume camera contour plot for ground-based beacon.....	33
38	Composite plume camera image.....	35
39	Plume camera contour plot.....	37
40	Tracker camera contour plot for ground-based beacon.....	40
41	Tracker camera contour plot.....	41
42	Tracker camera image of ground-based beacon illustrating the point spread function.....	43
43	Composite tracker camera image.....	45
44	Highlighted plume central region for Nihka.....	51
45	Photoevents as a function of defined central region size.....	51
46	Plume camera PSF for ground-based beacon.....	52
47	Axial profile through plume camera PSF for ground-based beacon.....	53
48	Axial profile along plume central region, plume camera.....	53
49	Tracker camera PSF for ground-based beacon.....	54
50	Axial profile through tracker camera PSF for ground-based beacon.....	54
51	CHARM 1.3 image prediction for PC-1 before and after smearing.....	51
52	CHARM 1.3 contour plot prediction for PC-1 after smearing.....	57
53	CHARM 1.3 predicted axial profile before and after smearing.....	57
54	Nihka, plume camera, total field-of-view intensity.....	59

## FIGURES (cont'd)

55	Nihka, plume camera, central region intensity.....	59
56	Nihka, tracker camera.....	60
57	Measured spectral radiant intensity for the Nihka, plume camera field of view .....	61
58	Composite tracker camera image showing flash and two streaks.....	63
59	Composite plume camera image showing anomalous bright object and Nihka plume.....	63
60	Target Size During Stable Tracking of Nihka Plume.....	64
61	Centroid Error During Stable Tracking of Nihka Plume .....	64

## TABLES

1	Instrument Characteristics.....	3
2	Expected Intensities for Nihka.....	6
3	Sequence of Events During Nihka Observation Pass.....	8
4	Sequence of Tracking Events During Nihka Burn.....	11
5	Tracker Servo Response.....	15
6	Tracker Jitter Statistics.....	16
7	Plume Camera Filter, $\lambda_m$ , and Peak Quantum Efficiency.....	21
8	$P_k/\tau$ and $L_{pn}$ for Brightest Pixel.....	21
9	Photoevents per Second From Nihka Plume and Reference Spectrum Model for Brightest Pixel and Ratios of These Values.....	24
10	Centroid Wavelength, $\lambda_c$ , for Various Spectra.....	24
11	Summary of Formulas Defining Conversion Constants.....	26
12	Conversion Constants for the Reference Spectrum.....	26
13	Radiometric Values for One Photoevent Per Second.....	26
14	Definition of the Data Interval.....	27
15	Parameters Associated with the Data Interval.....	27
16	Basic Parameters.....	38
17	Plume Camera Apparent Peak Radiometric Values.....	38
18	Apparent Velocity Vector Direction During Observation.....	39
19	Percent Error per Image Resulting from Measurement Noise, $\epsilon_N$ .....	47
20	Error in $1/G_g$ for Tracker and Plume Cameras.....	47
21	Plume Central Region Radiometric Percent Errors for Plume Camera.....	48
22	Central Region Plus Outer Region Radiometric Percent Errors for Plume Camera.....	48
23	Radiometric Percent Errors: Tracker Camera Over 19 x 19 Pixel Window.....	48
24	Total Radiometric Percent Errors, $\epsilon_T$ .....	49
25	Plume Camera NER Per Pixel for Data Interval.....	50
26	Tracker Camera NER Per Pixel.....	50
27	Central Region Extent in Plume Camera.....	50
28	Observed Axial Length of Plume Central Region.....	52
29	Peak Radiance Comparison.....	58
30	Comparison of Measured to Predicted Plume Length.....	58
31	Summary of Plume Camera Average Radiant Intensity.....	59
32	Summary of Tracker Camera Average Radiant Intensity.....	60
33	Measured Spectral Radiant Intensity.....	61

## EXECUTIVE SUMMARY

The observation of the Nihka rocket plume was the first demonstration of the ability of the Ultraviolet Plume Instrument (UVPI) [1] to observe missiles in flight above the atmosphere. The UVPI is a small, plume-tracking instrument flown on the Naval Research Laboratory's Low-power Atmospheric Compensation Experiment (LACE) satellite, which was launched on 14 February 1990. The Nihka rocket was launched from the Wallops Island Launch Facility in Virginia. The launch time and trajectory were selected to synchronize the flight with a LACE pass.

Missile tracking in the ultraviolet is advantageous because of extremely low Earth and solar backgrounds, extremely sensitive photodetectors that do not require cryogenic cooling, and very high optical resolution, which is possible with optics of relatively modest size.

The UVPI system aperture is only 10 cm in diameter. However, it can detect and image missile plumes at a 500-km range. The two cameras of the instrument use narrowband filters, image intensifiers, and charge-coupled devices (CCD) to observe sources in the ultraviolet (UV). The primary function of the tracker camera, viewing over a relatively wide field ( $1.97^\circ$  by  $2.62^\circ$ ) and broad spectrum (255 to 450 nm), is to locate and track a source for higher resolution observation by the plume camera. The plume camera has a narrow field of view ( $0.180^\circ$  by  $0.135^\circ$ ) and observes sources through any of four filters with passbands of 195 to 295 nm, 220 to 320 nm, 235 to 350 nm, and 300 to 320 nm. The wavelengths shorter than 310 nm are essentially invisible from the ground because of atmospheric absorption. The limiting resolution of the tracker camera is about  $230 \mu\text{rad}$ , and that of the plume camera about  $90 \mu\text{rad}$ , equivalent at 500-km range to 115 m and 45 m, respectively.

A three-stage sounding rocket (called Black Brant X) was used for the test. The first and second stages of the three-stage rocket fired only at low altitude (below 40 km). They were not expected to be visible in the ultraviolet from space. The third stage, or Nihka, which used an aluminized solid-fuel motor reached 190-km altitude and was successfully detected and tracked by the UVPI from a range of 448 to 463 km.

The Nihka plume was successfully tracked for 3.23 s, and 96  $1/30$ -s images of plume data were acquired by using the plume-camera filter in the 220 to 320-nm range, termed the PC-1 filter band. The image quality and tracking accuracy were of sufficient quality to permit the superposition of images for plume radiance determination. Image superposition to enhance the signal level is needed for accurate radiometry because of the small telescope aperture.

The spectral radiance and spectral radiant intensities of the Nihka plume were extracted from these images. Absolute values were obtained from an assumed spectral shape, namely, one derived from a physical model of the plume as a nearly transparent stream of micron-sized alumina particles at their melting points. This spectral shape serves as the reference model spectrum. The UV signal detected by using the PC-1 filter appeared to show an excess relative to that expected from the reference spectrum normalized to the broadband tracker-camera signal. This apparent UV excess relative to the reference spectrum is consistent with data gathered on the Stryi flight [2], which also showed an apparent excess in the far UV relative to the reference spectrum. The Nihka data did show an identifiable UV bright outer region of the plume similar to the UV luminous outer region seen on the Stryi flight [2]. As in the case of the Stryi flight, the luminous outer region appeared to be the primary source of the excess UV emission.

The time dependence of the plume central-region radiant intensity measured in PC-1 in the plume camera showed no pronounced trends or variations for the Nihka stage. However, the outer-region signal showed a pronounced upward ramp for the same period.

The tracker camera, within its relatively limited resolution, obtained radiant intensity data to 450-nm wavelength. These data, with the plume-camera data in the 220 to 320-nm band, support the conclusions that the UV luminous outer region of the Nihka plume became more radiant with time.

Two anomalous events were observed during the UVPI Nihka observation period. The first event was a bright flash, possibly associated with a second-stage burnout "chuffing" event. The second was a bright object appearing in one frame of the plume camera near the end of the Nihka third-stage burn. This object was brighter than the Nihka plume itself and somewhat removed from its flight path.

This base of UV Nihka radiometric data will be a foundation for further analysis to provide refined interpretations and evaluation. Comparison with models and with data from sensors on other platforms and with data from other test flights will also yield improved radiometric results and an enhanced phenomenological understanding of UV emission by solid rocket motors in the upper atmosphere.

## **UVPI IMAGING FROM THE LACE SATELLITE THE NIKHA ROCKET PLUME**

### **1.0 INTRODUCTION**

#### **1.1 Background**

The Ultraviolet Plume Instrument (UVPI) carried aboard the Low-power Atmospheric Compensation Experiment (LACE) satellite launched in February 1990 was designed to collect rocket plume imagery in the ultraviolet band. A Nihka solid-fuel rocket motor, which was the third stage of a Black Brant X sounding rocket, was selected for the first in a series of rocket-plume observation tests. The overall objective of the observation was to gather data at moderate altitude (around 100 km) from space to enhance the current level of understanding of plume physics and chemistry and to help answer questions about radiance, spatial extent, and temporal variability of plumes. More specific objectives are listed in Section 1.3, which describes the Nihka mission plan. A Glossary is located at the end of this report.

#### **1.2 UVPI Capability**

The Ultraviolet Plume Instrument (UVPI) is carried aboard the Low-power Atmospheric Compensation Experiment (LACE) spacecraft. The UVPI's mission is to collect images of rocket plumes in the ultraviolet waveband and to collect background image data on Earth, Earth's limb, and celestial objects. Background object imagery collected with the UVPI includes the day and night Earth limb air glow, aurora, sunlit and moonlit clouds, solid Earth scenes with varying solar illumination, cities, and stars. A detailed description of UVPI can be found in the UVPI description and data methodology report [1] and in the Strypi plume report [2].

The UVPI sensor head assembly [3,4] contains two coaligned camera systems that are used in concert to acquire the object of interest, control UVPI, and acquire UVPI images and radiometric data. The two camera systems are the tracker camera and the plume camera, which are discussed briefly below. The two cameras share a fixed 10-cm diameter Cassegrain telescope that uses a gimbaled plane steering mirror to view a field of regard that is a 50° half-angle cone around the nadir. In addition, UVPI contains a second plane mirror on the instrument door. The mirror can be set at an angle of approximately 45° relative to the nadir and used in conjunction with the steering mirror to view the Earth limb and stars near the limb. The configuration of the UVPI and the radiometric response of UVPI are discussed in Refs. 1 and 2; characteristics of the UVPI have been previously reported [4,5].

The tracker camera is an intensified charged-coupled device (CCD) camera, which is sensitive over a wide wavelength range extending from 255 to 450 nm. Figure 1 shows the overall response of the tracker camera as a function of wavelength, including the effects of the bandpass filter in the camera system, the photocathode response, and the other optical elements. This camera has a relatively wide total field of view of 1.97° by 2.62°; images over this full field of view can be recorded at a 5 Hz image rate. The tracker camera can also be operated in a mode where the transmitted field of view is restricted to the central 17% of the full field of view, and the image rate is increased to 30 Hz. The intensifier gain and the exposure time of the camera can be controlled to provide a radiometric dynamic range greater than 10<sup>6</sup>.

The plume camera is also an intensified CCD camera operating in the ultraviolet. The plume-camera optical train contains a filter wheel with four selectable filters that have bandpasses within the 195 to 350 nm range. Figure 2 shows the overall response of the plume camera for each of these four filters. The plume camera has a total field of view of  $0.180^\circ$  by  $0.135^\circ$  with a correspondingly higher resolution than can be achieved by the tracker camera. Plume camera images can be recorded or transmitted at either 5 or 30 Hz, depending on the desired field of view. The intensifier gain can be controlled to provide a radiometric dynamic range greater than  $10^6$ . Table 1 summarizes the instrument characteristics and telemetry rates.

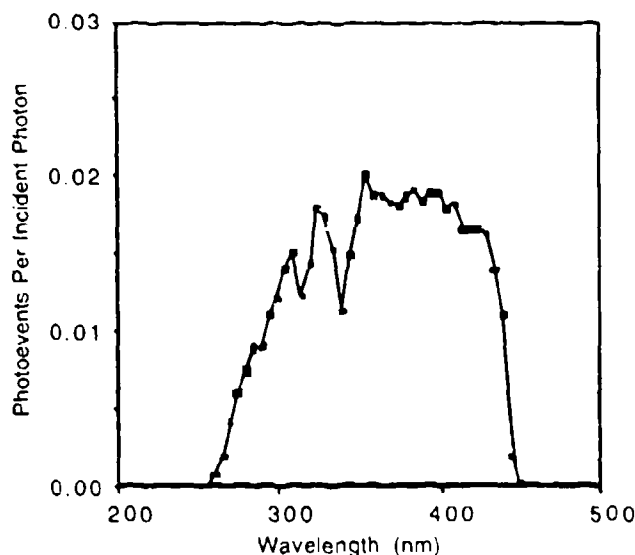


Fig. 1 - Tracker camera: net quantum efficiency curve

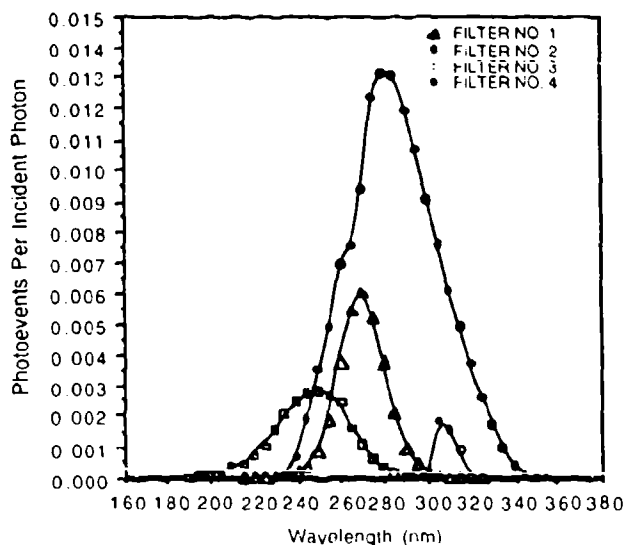


Fig. 2 - Plume camera: net quantum efficiency curves

Table 1 - Instrument Characteristics

Parameter	Tracker Camera	Plume Camera
Shared telescope type	Maksutov Cassegrain	Maksutov Cassegrain
Telescope diameter	10 cm	10 cm
Focal length	60 cm	600 cm
Field of view	2.62° x 1.97°	.180° x .135°
Field of regard	100° x 97°	100° x 97°
Field of view per pixel	182 x 143 $\mu$ radian	12.5 x 9.8 $\mu$ radian
Pixel footprint @ 500 km	91 x 72 m	6.2 x 4.9 m
System resolution (FWHM)	220 to 250 $\mu$ radian	80 to 100 $\mu$ radian
Spectral region	255-450 nm	195-350 nm
Number of filters	1	4
Photocathode material	Bialkali	Cs Te
Time for filter change	n/a	1.7 s
Digitization	8 bits/pixel	8 bits/pixel
Digital data rate	2.5 Mbps	2.5 Mbps
Image rate: normal	5 per second	5 per second
zoom*	30 per second	30 per second
Pixels: normal	251 x 240	251 x 240
zoom	91 x 112	91 x 112
Pixel exposure time	0.16 to 33.3 ms	33 ms
Frames integrated	n/a	1-6
Exposure range	>10 <sup>6</sup>	>10 <sup>6</sup>

\*Reduced field of view.

### 1.3 Scientific Objectives for UVPI

The primary goal of the Nihka mission [6] for UVPI was to collect spatially resolved, radiometric UV plume data. This was to be accomplished for the third, or Nihka, stage of the Black Brant X rocket by using UVPI's capabilities for tracking and imaging a moving target at long range. The one plume-camera filter chosen to take data was filter 1 (which has a band pass in the mid-UV band) because these data can be obtained only from a space-based sensor, and this band of emission has the best potential for high signal-to-background contrast. Pointing accuracy was optimized because this simplifies registration of images when superposed, a necessary procedure for improving statistics.

A secondary goal was to observe any serendipitous special events such as transients, puffs, chuffing, clouds, or contrails. The brightness, size, frequency, and persistence of such phenomena would provide useful information.

The specific objectives of the mission, related to UVPI data, are given in the following subsections. They revolve around a number of questions concerning plume radiance, spatial extent, temporal variability, and spectral shape of the UV emissions [7-9]. The objectives are grouped under headings reflecting these subjects.

#### 1.3.1 Radiometrics

The following objectives are basic to those listed in the subsequent subsections:

- Obtain isoradiance contours from the plume camera for the Nihka-stage plume.
- Obtain radiant intensity measurements from the plume camera for the Nihka-stage plume based on the entire field of view of the plume camera and on a subregion corresponding approximately to a plume core.

- Compare radiometric measurements for the Nihka-stage plume with other measurements or expectations.
- Provide radiometric measurements for non-plume, transient phenomena, if any.

### 1.3.2 *Spatial Features*

- Obtain the length of the Nihka plume and investigate implications for cooling rate and emissivity of particles.
- Obtain the shape of the shock boundary/mixing layer of the rocket.
- Identify asymmetries in plume shape and investigate angle-of-attack and uneven burning as possible causes.

### 1.3.3 *Temporal Features*

- Identify temporal trends in radiometrics and investigate possible dependence on rocket velocity and altitude.
- Investigate radiometric fluctuations to determine whether short-term variations in brightness are observed.
- Identify changes with time in the shape of the plume's outer regions, if any, and investigate possible dependence on rocket velocity and altitude.
- Identify persistence and cumulative effects, if any, in plume or nonplume phenomena.

### 1.3.4 *Spectral Features*

- Compare the plume central region's emission within a filter bandpass with a reference spectral shape prediction normalized to the tracker camera measured emissions.
- Relate tracker camera measurements to visible and infrared measurements made by other sensors.
- Gather data on the emission spectrum for the plume's outer regions, if any.

## 1.4 **Experiment Concept**

### 1.4.1 *Nihka Description and Launch Plan*

The target vehicle was a three-stage, suborbital rocket called Black Brant X. Its three stages were a Terrier booster, a Black Brant second stage, and a Nihka third stage. In addition, a Star 6B solid-fueled rocket mounted in the payload was to be fired before the third stage ignited to separate the payload from the third stage. Figure 3 is a schematic of the vehicle. The third stage had two 150-W quartz-halogen bulbs that supported the payload's mission but were not expected to be seen by the UVPI.

The Nihka third stage, which was the target of this UVPI observation, is a 12,000-lb thrust class, solid-fueled rocket motor manufactured by Bristol Aerospace Limited of Winnipeg, Manitoba, Canada. The solid propellant is 69.5% ammonium perchlorate, 18% aluminum powder, and 12.5% hydroxyl terminated poly butadiene (HTPB) binder. The Nihka rocket motor is 56.6 in. long, 17.3 in. in diameter, and weighs approximately 900 lb. The motor case is welded steel sheet with forged steel end domes. The nozzle is steel, with a throat insert of graphite-phenolic composite and a silica-phenolic composite exit cone. The nozzle has a 27.9 expansion ratio, a 19.6° divergence and an exit diameter of 15 in. Nominal burning time for the Nihka is 17.8 s; nominal pressure during burning is 910 lb per square in., absolute.

The Black Brant X rocket was scheduled for launch on 25 August 1990 at 07:04:10 GMT from Wallops Island, Virginia. The launch time was requested by the UVPI observation team to match the time of the LACE satellite's overflight.

The planned sequence of events called for the separation of the third, or Nihka, stage and payload from the second stage about 24 s after the second-stage burnout. Eleven seconds later the payload, known as the probe, was to be separated from the Nihka stage and drift away. About 30 s later the Star 6B motor on the probe was to fire to move the probe into position. The Star 6B was to burn for about 7 s. About 9 s after the Star 6B burnout, the probe was to reorient by 180° and find

the quartz-halogen bulbs on the Nihka rocket. These events were to occur several tens of seconds before the ignition of the Nihka stage and the UVPI observation of it.

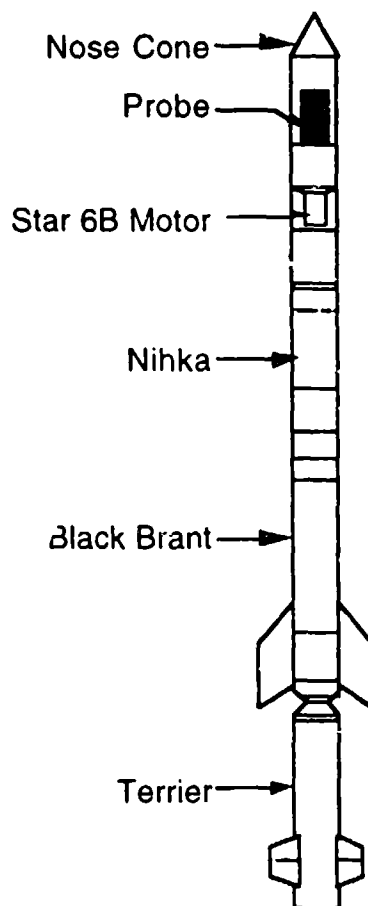


Fig. 3 - Black Brant X rocket

#### 1.4.2 Radiometrics

The Nihka rocket-motor propellant is a composite consisting of an oxidizer, powdered aluminum, and a small amount of hydrocarbon binder. The combustion products for such rocket motors are  $\text{Al}_2\text{O}_3$  particles,  $\text{H}_2\text{O}$ ,  $\text{CO}$ ,  $\text{CO}_2$ , and other gases. The temperature inside the rocket motor chamber is typically 3200 K, which is hot enough to melt the  $\text{Al}_2\text{O}_3$  (melting point = 2320 K) but not hot enough to vaporize it (boiling point approximately = 3700 K). As the exhaust exits the rocket nozzle it cools, and the  $\text{Al}_2\text{O}_3$  begins to solidify. The temperature of the exhaust decreases further as it moves away from the rocket [7].

In the ultraviolet, the emission from the plume central regions of solid-fuel rocket motors with aluminum is expected to be dominated by thermal emission from hot particles of  $\text{Al}_2\text{O}_3$ . In a simplified model, the temperature of the  $\text{Al}_2\text{O}_3$  particles is taken to be constant at the solidification temperature of 2320 K because the latent heat of fusion causes the temperature of the particles to pause momentarily at this point as they cool. In the outer region, other thermophysical processes can produce emission bands arising from exhaust gases or atmospheric constituents, and these will contribute to the spectrum.

Even in the simplified model, in which the  $\text{Al}_2\text{O}_3$  particles in the plume are assumed to be at a uniform temperature of 2320 K, the plume emission is different from a 2320 K blackbody for two primary reasons. First, the plume consists of a rather transparent cloud of particles, and the total emission from the cloud is substantially less than would be the case from a solid object the same size as the plume. Second, the  $\text{Al}_2\text{O}_3$  particles are typically a few microns in size and are inefficient emitters of visible and longer wavelengths. The effective emissivity for 2.3-micron particles of  $\text{Al}_2\text{O}_3$  is considered typical of particles in the plume. This is further discussed in Section 3.

The rocket's emission was estimated for the PC-1 bandpass by using a modified version of the CHARM 1.3 code. This result, together with the tracker camera prediction, is given in Table 2. This information was used for planning the mission.

Table 2 - Expected Intensities for Nihka

Filter	Aspect Angle	W/sr	Photoevents/Frame
PC-1	60°	16.0	20.7

## 2.0 NIHKA OBSERVATION

The UVPI and LACE delayed-execution commands and the associated pointing functions were transmitted to the spacecraft and UVPI at about 13:45 GMT on 24 August from the LACE ground site located at Vandenberg Air Force Base (VAFB), California. The delayed-execution commands turned the UVPI on, initialized its computer, and set its clock; these operations were done prior to acquisition of the LACE spacecraft's RF signal at the LACE ground site located in Maryland. Figure 4 shows the ground trace of the LACE spacecraft. Figure 5 shows the ground trace of the rocket and the UVPI tracker camera's field of view projected on the surface of Earth. The ground site at VAFB was in contact with the LACE spacecraft when the UVPI turned on and confirmed that the UVPI was operating normally. At acquisition of the signal at the Maryland site, the UVPI was executing a star scan. The purpose of this star scan was to measure the spacecraft's yaw attitude component. The roll and pitch attitude components that were used for this observation were predictions based on data taken from the LACE attitude sensors earlier that day.

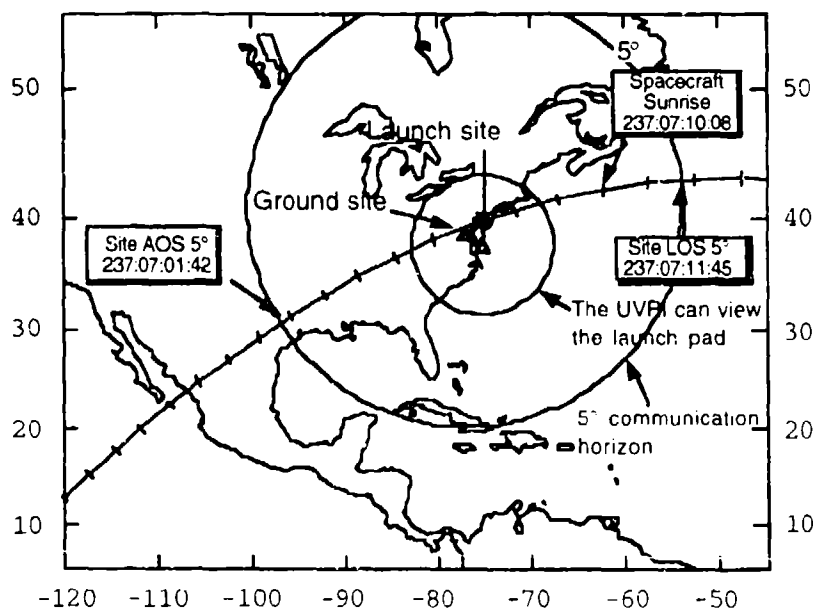


Fig 4 - Ground trace of the LACE satellite on Nihka plume observation pass

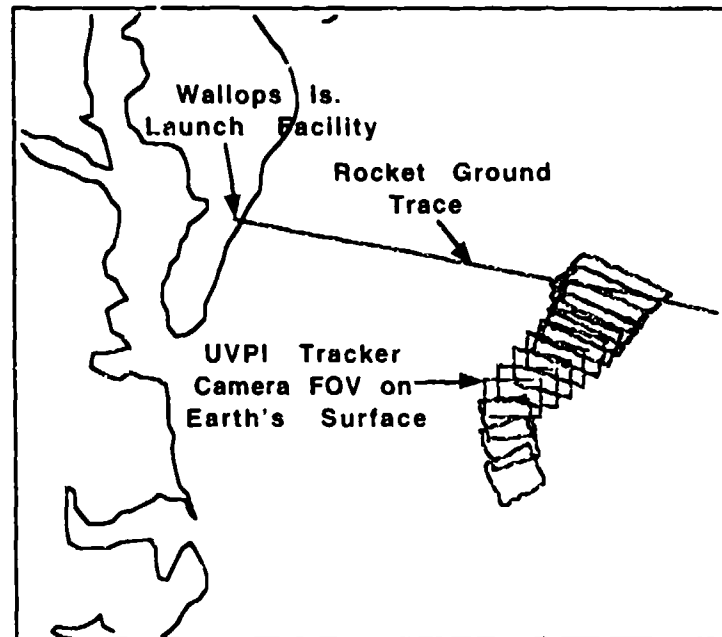


Fig. 5 - Ground trace of rocket and projected field of view of UVPI tracker camera

Immediately after the rocket launch, the actual launch time was relayed to the UVPI observation team by telephone from within the rocket launch facility. A final UVPI pointing function was then computed based on the measured LACE yaw, the actual rocket launch time, and the high precision orbital elements obtained just prior to the pass. This final rocket pointing function was designed to point with a circular scan pattern having a radius of  $1.1^\circ$  and a period of 16 s about the nominal rocket trajectory.

Table 3 lists the major and critical events that took place during this observation pass. When the Nihka rocket plume was first visible in the UVPI tracker camera, a prepared sequence of commands was transmitted to the UVPI. These commands had the UVPI acquire and track the rocket plume target, begin using the zoom mode of image transmission, and interleave the tracker-to-plume frames at a ratio of 2:8. The plan was to have the entire observation taken by using plume-camera filter number 1 because of the short burn duration of the Nihka rocket stage.

The total flight time for the Black Brant X rocket lasted about 12 minutes; final stage burnout occurred 192 s after liftoff.

## 2.1 Trajectory and Vehicle Performance Data

Figure 6 shows the Black Brant X rocket's altitude and velocity as a function of time based on the trajectory that was used to generate the UVPI pointing function. Appendix A provides detailed data on the Nihka trajectory. At Nihka burnout, altitude reached 180 km and velocity reached 2.6 km/s. The difference in location from the prelaunch trajectory and the actual location of the rocket during the Nihka motor burn ranged from about 5 to 7 km. Figure 7 shows the UVPI-to-target range, which is about 448 km at Nihka burnout. Aspect angle during the Nihka burn is shown in Fig. 8 and is about  $56^\circ$  at Nihka burnout. The aspect angle is the angle between the line of sight of UVPI and the longitudinal axis of the rocket. An aspect angle of  $0^\circ$  means that UVPI is looking directly at the nose of the rocket. Figure 9 shows the angle of attack of the Nihka rocket during its burn. The angle of attack is the angle between the rocket's thrust and velocity directions. Figure 10 shows the Nihka

thrust level, and Fig. 11 shows the orientation angle in the UVPI tracker camera during the time of the Nihka motor burn. The orientation angle is  $-59^\circ$  at Nihka burnout. The orientation angle is the angle of the longitudinal axis of the rocket, as viewed in the UVPI tracker camera's field of view, where  $0^\circ$  is horizontal pointing to the right and  $+90^\circ$  is pointing up.

Table 3 - Sequence of Events During Nihka Observation Pass

Time (GMT)	Event
7:01:54	LACE signal reception begins
7:01:55	Start tape recorder
7:01:55	Point to az = $+5.5$ , el = $4.5$
7:02:00	Point to az, el = $1.6$
7:02:05	Point to star, $\mu$ Horolgii
7:04:10	Black Brant X launch
7:04:54	2nd stage burnout
7:05:25	Tape recorder reels change
7:05:32	Open door fully
7:06:00	Set lost track function
7:06:02	Point to Nihka along nominal trajectory
7:06:17	Star 6B ignition, planned
7:06:25	Star 6B burnout, planned
7:06:29	Nihka beacon on, planned
7:06:56	UVPI commanded to 2:2 tracker:plume ratio
7:07:06	Nihka ignition, planned
7:07:07.49	First indication of Nihka off camera
7:07:08.29	First sight of Nihka in tracker camera
7:07:12.3	Begin closed-loop track of Nihka
7:07:12.7	First image of Nihka in plume camera
7:07:15.33	UVPI commanded to zoom mode
7:07:18.74	UVPI commanded to 2:8 tracker:plume ratio
7:07:22.61	Nihka burnout, observed
7:08:25	Stop tape recorder
7:09:31	Park gimbaled mirror
7:09:34	Close door
7:10:19	Move to filter #4
7:10:24	LACE enters sunlight
7:11:53	LACE signal lost

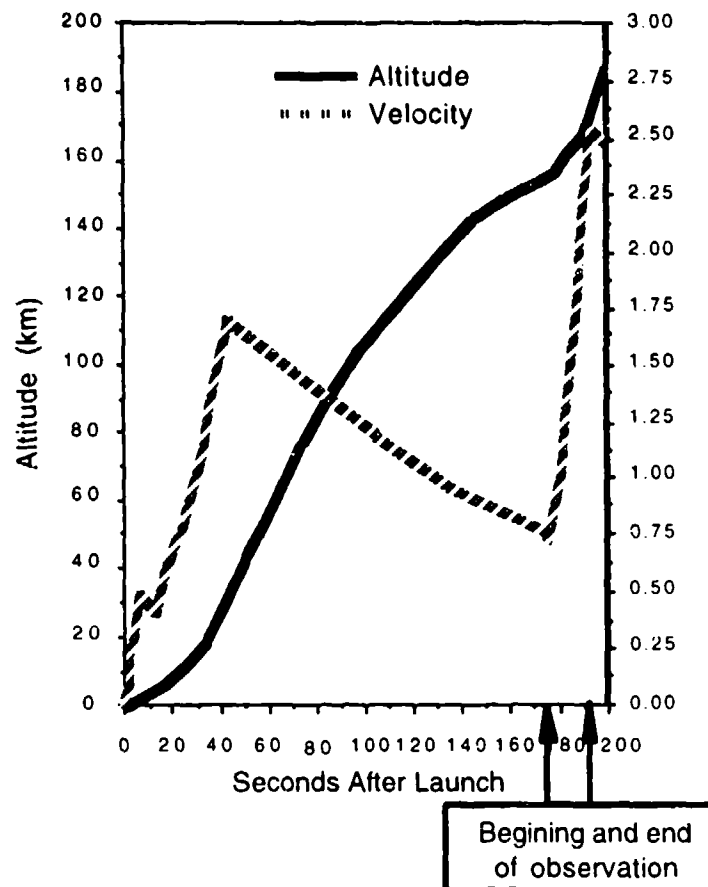


Fig. 6 - Altitude and velocity vs time

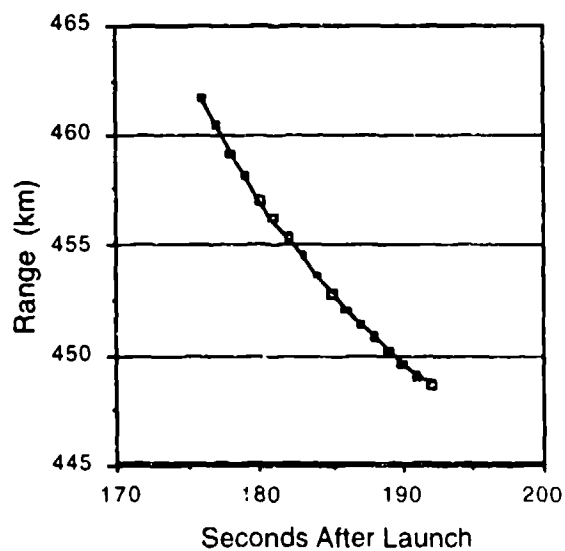


Fig. 7 - Range vs time

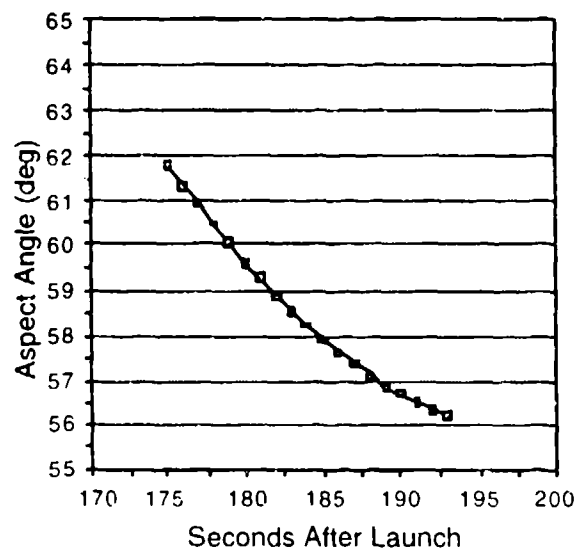


Fig. 8 - Aspect angle vs time

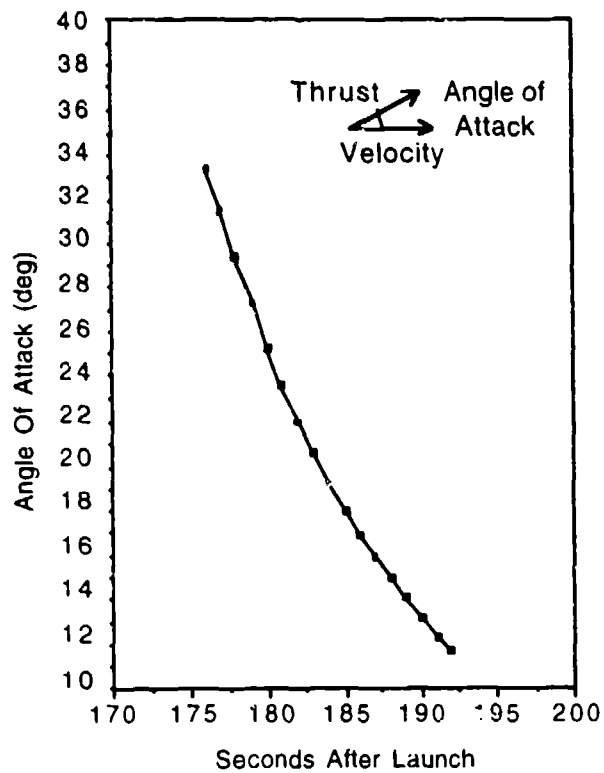


Fig. 9 - Angle of attack vs time

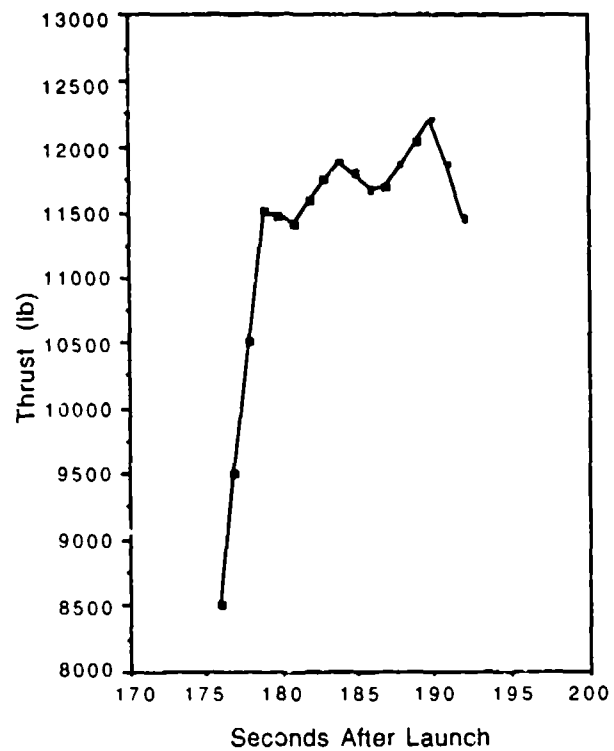


Fig. 10 - Nihka thrust vs time

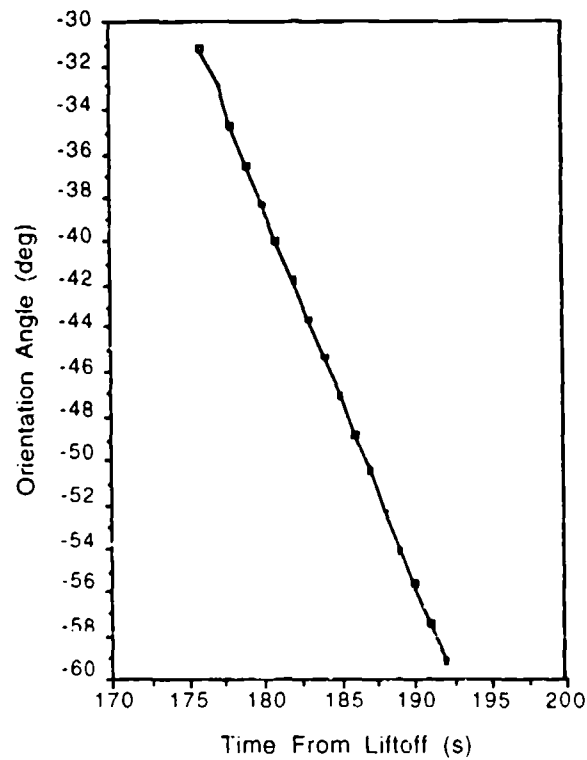


Fig. 11 - Orientation angle in UVPI tracker camera vs time

## 2.2 Tracking and Pointing Performance Data

### 2.2.1 Mode Sequencing Overview

The tracker was commanded to the mass/intensity centroid track mode throughout the Nihka observation. Figure 12 shows the sequencing of the various mission modes during the observation.

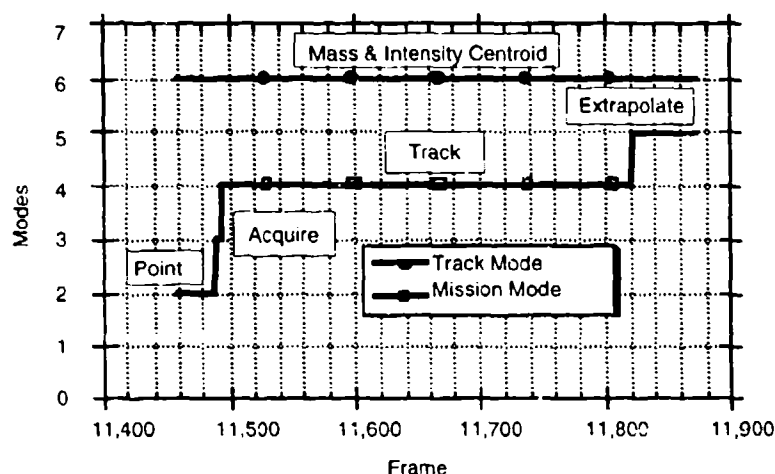


Fig. 12 - Track and mission modes vs frame

The Nihka rocket burned for approximately 17 s. The POINT mode was used to scan for the Nihka until it was within the tracker camera's field of view, at which time the ACQUIRE mode was commanded from the ground station. The tracker then locked onto the target in less than 0.1333 s and tracked for approximately 11 s. Therefore, approximately 6 s were required before the target appeared and was recognized in the tracker camera's field of view and TRACK mode could be achieved. The important events are tabulated in Table 4.

Table 4 - Sequence of Tracking Events During Nihka Burn

Frame	Mission Mode	Time (s)	Comment
11489	POINT	0.0	
11490	ACQUIRE	0.0333	
11491	ACQUIRE	0.0667	
11492	ACQUIRE	0.1	
11493	TRACK	0.1333	track lock
11524	.	1.1667	change track gate
11539	.	1.6667	change track gate
11614	.	4.1667	auto track gate
11820	TRACK	11.0333	
11821	EXTRAPOLATE	11.0667	lose track lock

The time column in Table 4 is arbitrarily chosen to support the servo response analysis that will be provided later in this section. For this observation, the linear equation for time is: TIME =

(FRAME-11489)/30. Note that there is  $1/30$ th of a second between frames. Figure 13 is a graph showing the relationship between time and frame number.

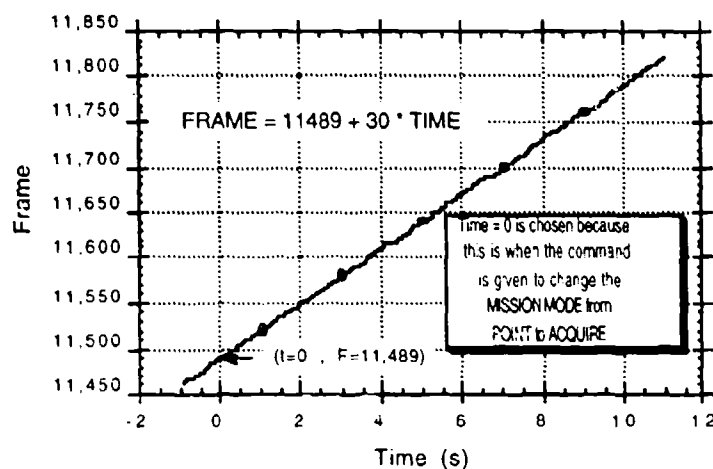


Fig. 13 - Frame vs time

Figures 14 and 15 show the azimuth and elevation gimbal angles, respectively, as a function of the frame number. Since the satellite's ground track was approximately toward the northeast and the rocket trajectory was approximately due east, the elevation gimbal angle only varied by about  $1^\circ$  during the engagement. The azimuth gimbal angle was initially looking ahead of the satellite and was looking behind the satellite at the end of the encounter. The azimuth angle varied about  $9^\circ$  during the encounter. The azimuth and elevation gimbal rates were calculated as  $0.7^\circ/\text{s}$  and  $0.1^\circ/\text{s}$ , respectively, which were well within the tracker's capability. The dashed lines in these plots represent the SC-1 commanded gimbal angles. At the beginning of the encounter, while operating in the POINT and ACQUIRE modes, the SC-1 commanded the gimbal angles. When the tracker locked onto the target image, the mode was set to TRACK and the tracker controlled the gimbal angles. Note that the SC-1 commanded gimbal angles remained fixed to the last commanded value. There was a noticeable transient as the tracker brought the track errors to zero. At the end of the encounter when the tracker lost the target image and went into the EXTRAPOLATE mode, the SC-1 extrapolated the immediately previous gimbal angles according to their respective rates. Also, note that the gimbal motion at this time exhibited a transient that was a result of the extrapolation function implementation. The windowing logic, shown in block form in Fig. 16, shows that the track gate size goes through fixed steps at 1.0, 1.5, and 4.0 s after initial tracker lockon.

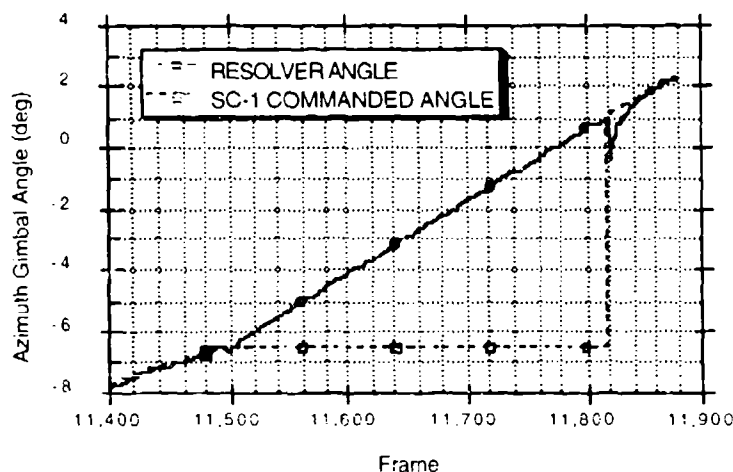


Fig. 14 - Azimuth gimbal angles vs frame

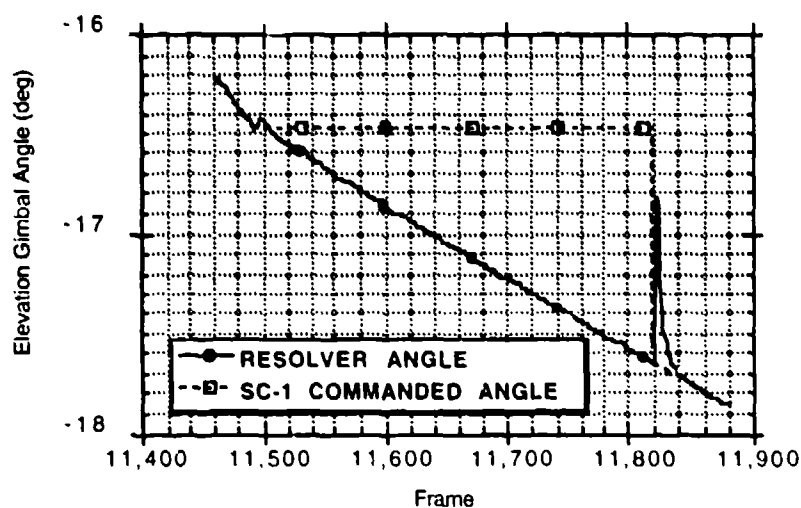


Fig. 15 - Elevation gimbal angles vs frame

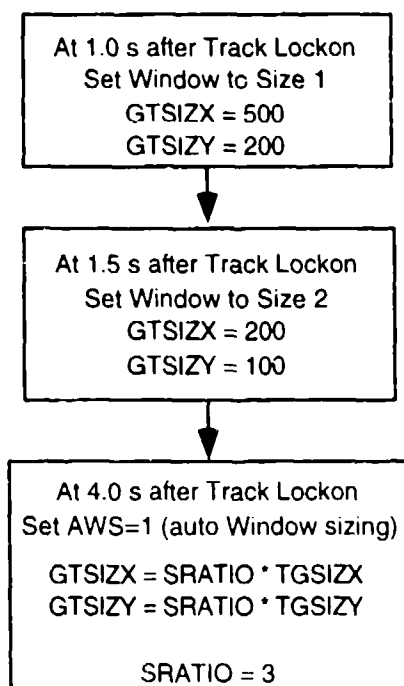


Fig. 16 - Block diagram of tracking sequence

Figures 17 and 18 present the tracking window (or track gate) size, and target size as a function of the frame number. The initial track gate size is set to 2046 in X and 1022 in Y, which is equivalent to a fully open track gate equal to the total field of view.

The target size remained within the track gate at all times during the time that the tracker was locked onto the Nihka rocket.

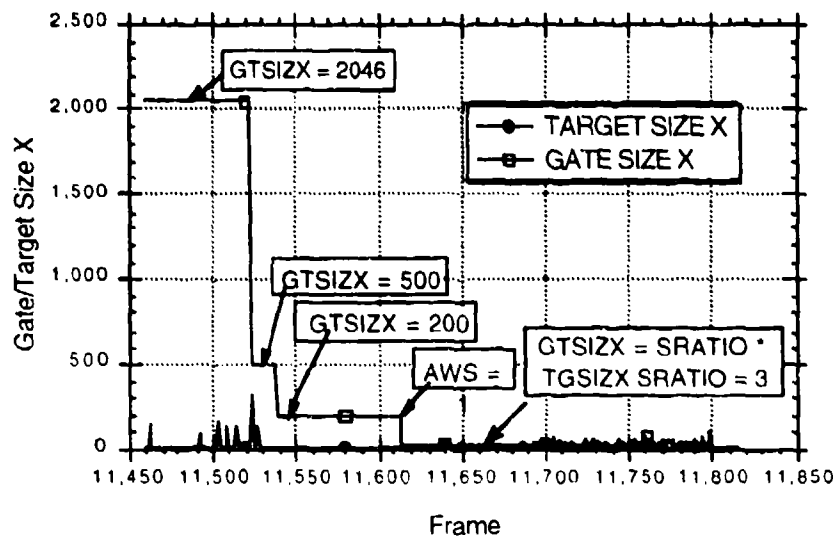


Fig. 17 - Track gate/target size X vs frame

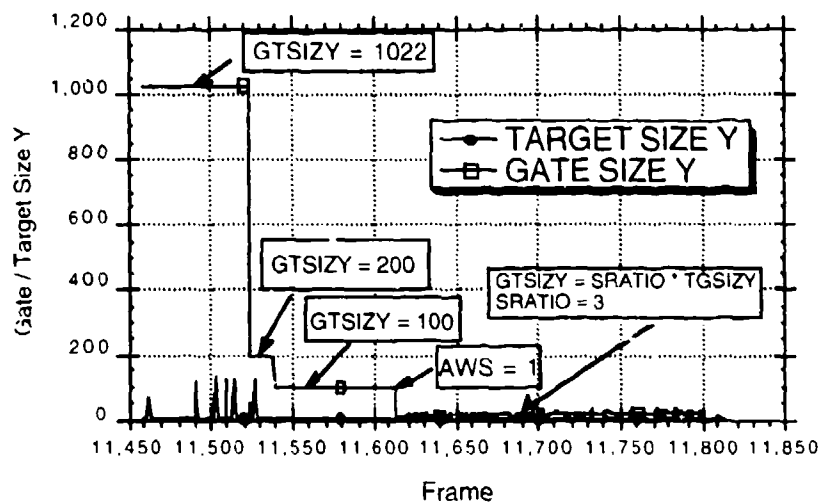


Fig. 18 - Track gate/target size Y vs frame

### 2.2.2 Tracker Servo Response

Figure 19 shows the error gain corrections for converting the focal plane tracker errors into gimbal commands. A comparison with the actual equations shows that these curves agree with the error gain equations given below:

$$\begin{bmatrix} A & B \\ D & E \end{bmatrix} = \begin{bmatrix} -1 & -\frac{\tan(\Theta) \tan(\Phi)}{2} \\ \frac{1}{2 \cos^2(\Phi)} & 0 \end{bmatrix}$$

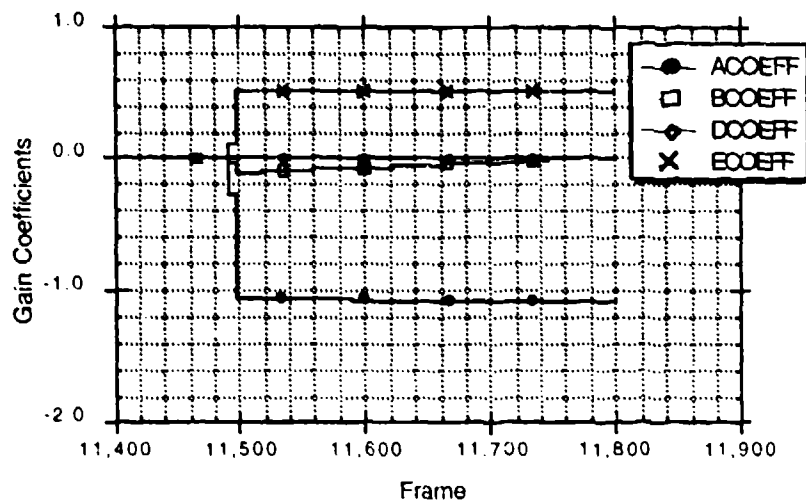


Fig. 19 - Gain coefficients vs frame

The tracker errors are plotted as a function of time in Fig. 20. Table 5 shows the tracker servo response determined from this plot.

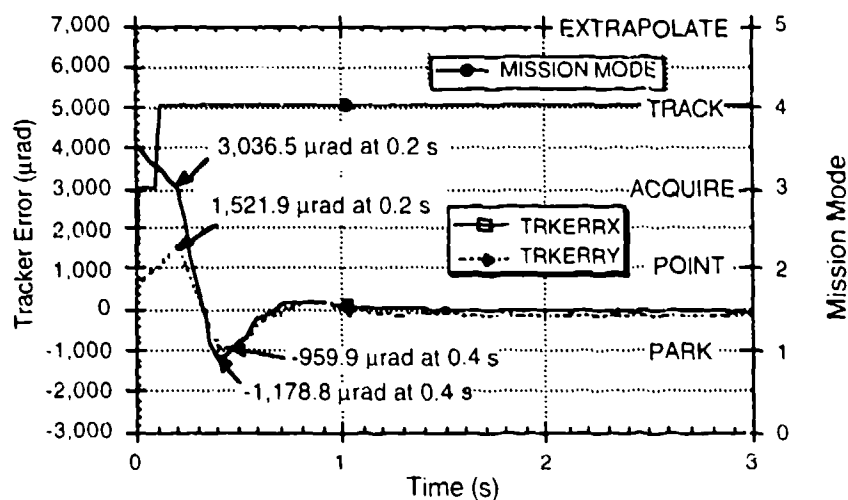


Fig. 20 - Tracker error response vs time

Table 5 - Tracker Servo Response

	TRKERRX	TRKERRY
Rise time	< 0.2 s	< 0.2 s
% Overshoot	~ 40%	~ 28%
Settling time	< 1.0 s	< 1.0 s

These results compare favorably with the prior laboratory tests and tracker simulation results. The large overshoot is attributed to the "type 3" servo implementation, which provides zero steady state tracking error when tracking an accelerating target.

### 2.2.3 Tracker Jitter

The tracker jitter is determined between frames 11550 and 11800. Figure 21 shows the tracking errors plotted as pixels or television lines vs the frame numbers; Fig. 22 plots the tracking error in  $X$  vs the tracking error in  $Y$ . These two different perspectives show that the tracker is biased approximately half a pixel in  $Y$  with an elongated scattering in the  $X$  direction that oscillates between  $\pm 1$  pixel. Statistics on this set of data are shown in Table 6.

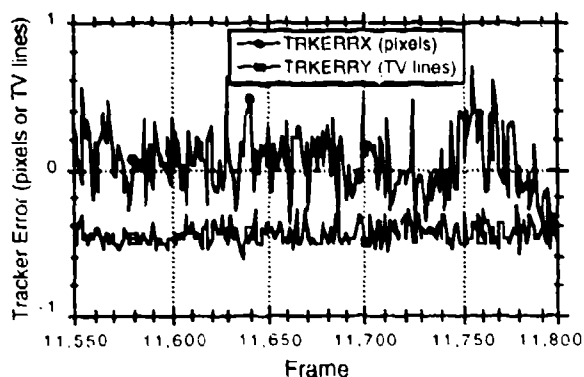


Fig. 21 - X and Y tracker errors vs frame

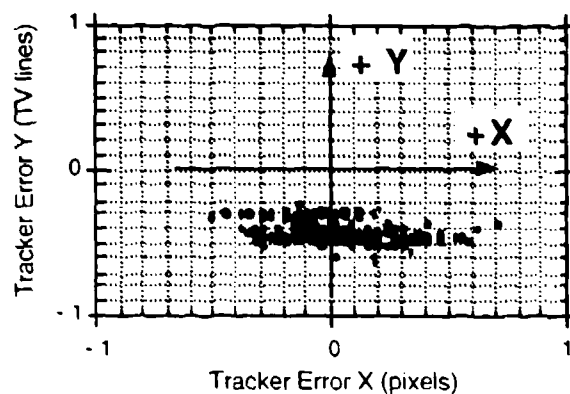


Fig. 22 - Y tracker error (TV lines) vs X tracker error (pixels)

Table 6 - Tracker Jitter Statistics

	TRKERRX (pixel)	TRKERRY (TV line)	TRKERRX ( $\mu$ rad)	TRKERRY ( $\mu$ rad)
Minimum	-0.50	-0.625	-30.00	-89.38
Maximum	0.72	-0.25	43.14	-35.75
Sum	12.44	-110.25	746.58	-15765.75
Points	251	251	251	251
Mean	0.050	-0.44	2.97	-62.81
Median	0.031	-0.47	1.86	-67.07
RMS	0.22	0.44	13.12	63.56
Std Deviation	0.21	0.068	12.81	9.77
Variance	0.046	0.0047	163.97	95.44

A more representative picture is shown in Figs. 23 and 24 where the pixels and television lines have been converted to microradians. The statistical results from these plots are also shown in Table 6. The conversion from  $x$ -pixels to microradians is  $60 \mu$ rad per pixel; the conversion from  $y$ -TV lines to microradians is  $143 \mu$ rad per TV line. Note that the bias in the  $Y$  direction is approximately  $-63 \mu$ rad. The standard deviation is the RMS value about the mean. Hence, the  $X$  and  $Y$  tracker RMS about their respective means is  $13 \mu$ rad in  $X$  and  $10 \mu$ rad in  $Y$ . These values are better than the tracker jitter specification of  $15 \mu$ rad RMS.

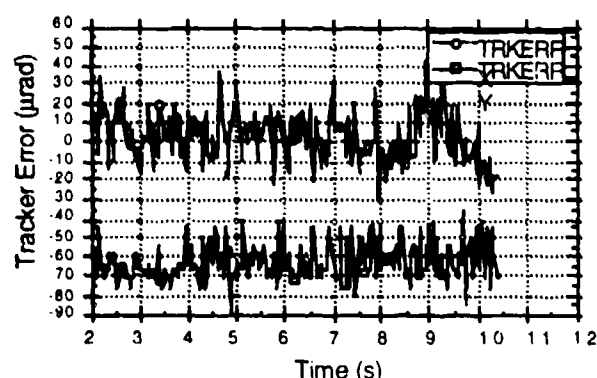


Fig. 23 - X and Y tracker errors vs time

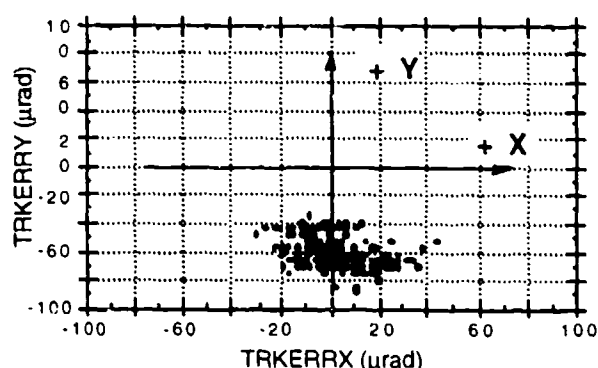


Fig. 24 - Y tracker error vs X tracker error

### 3.0 EXTRACTION OF RADIOMETRIC QUANTITIES

Three levels of data reduction are useful for any radiometric experiment. At the first level, data are reduced to instrument readings or counts at the image plane; at the second level, readings are converted by instrument-specific factors, which may be approximate, into quantitative measures of physical quantities, e.g., radiance, with no assumed spectral shape for the source being used; and, at the third level of reduction, a spectral shape is assumed to reduce data and present it.

It is necessary to assume a spectral shape because instrument efficiency is a function of wavelength within each band. Therefore, the spectral distribution of incident photons is needed to provide the appropriate weighting at each wavelength within the passband of integrated response. Since the spectral shape is not known from the data, a spectral shape must be assumed to determine this weighted distribution. Once a spectral shape has been assumed, the number of photoevents measured is used to infer the amplitude or intensity of the emission with that spectral shape.

#### 3.1 Data Calibration Procedure

The raw image data transmitted from the satellite are in the form of arrays of 8-bit binary numbers  $Q_k$ , which represent the intensity of light falling on the  $k$ th pixel of the CCD. From  $Q_k$ , an estimate of the number of photoevents  $P_k$  occurring at the corresponding photocathode pixel during the image frame can be obtained by using:

$$P_k = (Q_k - D_k)/(U_k G_g) \quad (1)$$

where

$G_g$  is the gain conversion factor for gain step  $g$ , i.e., the value of  $Q_k$  for a single photoevent, assumed to be the same for all pixels  $k$ ;

$D_k$  is the dark value for the  $k$ th pixel; and

$U_k$  is the gain nonuniformity correction factor for the  $k$ th pixel.

The pulse height distribution of the image intensifier will cause noninteger values for  $P_k$ . The conversion of CCD response peaks to integral photoevent counts is possible only on the weakest images because of the overlap of photoevent images. Hence,  $P_k$  values are treated as continuous variables. The  $G_g$ ,  $D_k$ , and  $U_k$  factors are discussed in detail with the data calibration procedure in Section 2.0 of the UVPI data reduction methodology report [1].

### 3.1.1 Statistical Discrimination Of Photoevents

When a single photoevent is generated in the microchannel plate (MCP) of the UVPI plume camera, it is registered as a spatial distribution of charge in the CCD focal plane array (FPA). In general, a photoevent gets registered within a  $3 \times 3$  pixel region with the largest FPA response at the center pixel. Note that the blurring of a single photoevent over the  $3 \times 3$  pixel region is a relatively small component of the overall system point spread function.

When UVPI is looking at a source that is dim compared to the instrument sensitivity, the instrument gain is automatically set high, for example, gain 13. At these high gains the calibration procedure, i.e., the estimation of photoevents from the measured digital number (DN), is sensitive to any mismatch between the estimated dark field level used for calibration and the actual dark field level. Although a small bias error in the dark field estimate would have a small impact on the photoevent estimate for a single pixel, it could have a large impact on the results when summing the contribution of groups of pixels. Hence for dim signal levels, such as the Nihka rocket plume, a statistical discrimination scheme was developed that fixes the probability of false alarm for every pixel. In the context of calibrating UVPI data, a false alarm occurs when the noise in a pixel that contains no target is large enough to be considered part of a photoevent.

Working with the already calibrated images, the discrimination scheme consists of estimating a statistical decision threshold for each image. The threshold is given in terms of background mean, standard deviation, and accepted probability of false alarm. Estimates for each image of the background mean and variance are made by using 4 image blocks located at each corner of the image and with dimensions of 8 by 8 pixels. The estimated threshold will exactly correspond to a probability of false alarm of  $PF$  if the following assumptions hold [10]:

- the local mean and local variance background statistics are the same over the whole FPA, and
- the density function of the background follows a Gaussian distribution.

Mathematically the decision threshold is given by:

$$t' = \mu + \sigma \cdot t',$$

where

- $\mu$  is the estimated background mean,
- $\sigma$  is the estimated background standard deviation, and
- $t'$  must satisfy the integral equation

$$PF = \text{erfc}(t').$$

where the standard complementary error function is used [10].

All the plume camera images used in this report to estimate radiance or radiant intensities were subjected to the above discrimination scheme by using a probability of false alarm of 0.0001. False alarms were, in fact, observed in approximately 1 out of every 10000 pixels, indicating that the two assumptions stated above are generally representative of these data. Because a photoevent may spread over a  $3 \times 3$  pixel region, immediate neighbors were also included as possible signal contributors for all those pixels where a photoevent took place. A new estimate for the number of photoevents from the  $k$ th pixel was computed based on the following rule,

$$P_k = \max(0, P_k - \mu) \quad \text{if condition (A) holds, or} \\ P_k = 0, \text{ otherwise.}$$

In the above, condition (A) states that if any pixel in the local neighborhood of the  $k$ th pixel exceeds  $t'$  then the value at the  $k$ th pixel is adjusted to be the maximum of zero or  $P_k - \mu$ . Thus, pixels containing no photoevent contribution are set to exactly zero, eliminating the possibility of an "erroneous" contribution resulting from uncertainties in the dark field estimate for that pixel. This adjustment can be significant when large numbers of pixels contain no photoevents, i.e., few photoevents per image.

Figure 25 is a composite image created with no statistical discrimination; Fig. 26 is one created by using statistical discrimination.

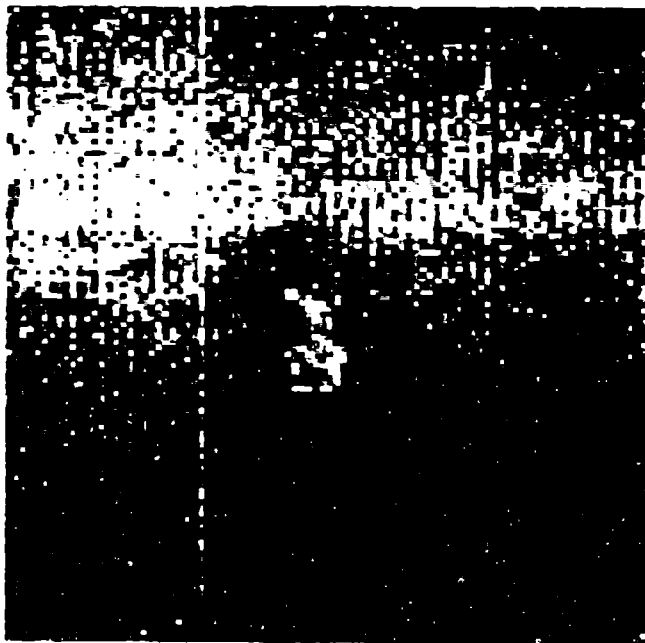


Fig. 25 Composite image using no statistical discrimination



Fig. 26 Composite image using statistical discrimination

### 3.2 Relation of Photoevents to Source Radiance

Presumably, the photoevents at the image plane are a result of a radiation source in the field of view. If the radiation source is isotropic and uniform over an emitting region of area  $A_s$ , then an expression for the photon flux  $\phi_{in}$  incident on the face of the telescope in photons/second is:

$$\phi_{in} = (A_s \Omega_s / hc) \int \lambda L(\lambda) d\lambda, \quad (2)$$

where

- $L(\lambda)$  is source spectral radiance in W/m<sup>2</sup>-nm-sr,
- $A_s$  is area of emitting region,
- $\Omega_s$  is solid angle of emission subtended by the telescope,
- $h$  is Planck's constant, and
- $c$  is speed of light.

The factor  $\lambda/hc$  converts the spectral radiance  $L(\lambda)$  to a photon radiance (photons/s-m<sup>2</sup>-nm-sr).

By setting the size of the emitting region equal to the footprint area of a pixel, the following reciprocity relation results:

$$A_s \Omega_s = A_s A_c / R^2 = A_c \Omega_p,$$

where

- $A_c$  is system aperture area,
- $\Omega_p$  is pixel field of view, and
- $R$  is range from the detector to the emitting region.

The general expression for the number of photoevents  $P_k$  in pixel  $k$  at the image plane that result from an emitting source of spectral radiance  $L(\lambda)$  filling the pixel field of view is then given by [11]:

$$P_k = (A_c \Omega_p \tau / hc) \int \lambda Q(\lambda) L(\lambda) d\lambda, \quad (3)$$

where

- $\tau$  is exposure time and,
- $Q(\lambda)$  is wavelength-dependent photoelectronic conversion efficiency, or net quantum efficiency, of the optics and detector.

In general, the exposure time  $\tau$  is 1/30th s for the plume camera and variable to a maximum of 1/30th s for the tracker camera. The pixel field of view  $\Omega_p$  is 12.5 by 9.8  $\mu$ rad =  $1.22 \times 10^{-10}$  sr for the plume camera, and 182 by 143  $\mu$ rad =  $2.6 \times 10^{-8}$  sr for the tracker camera. At the typical range of 500 km, these pixel fields of view correspond to 6.2 by 4.9 m and 91 by 72 m, respectively.

For further insight into the relationship of photoevents to source radiance, several forms of approximation can be helpful. Eq. (3) can be rearranged as follows:

$$\int \lambda Q(\lambda) L(\lambda) d\lambda = (P_k / \tau) (hc / A_c \Omega_p). \quad (4)$$

Now note that the integral on the left is similar to the source radiance integral,  $\int L(\lambda) d\lambda$ , except for the  $\lambda$  and  $Q(\lambda)$  factors. One quick and simple approximation involves substituting constant values for  $\lambda$  and  $Q(\lambda)$ , allowing them to come out from under the integral and move to the right side. For example,  $\lambda_o = (\lambda_1 + \lambda_2)/2$  and  $Q_o = Q_{max}/2$  provide estimated "average" values that allow

reduction of the integral to an approximate radiance. The sensitivity of this approximate radiance to  $\lambda$  and  $Q(\lambda)$  for various assumed spectra is discussed in Section 4.6 of Ref. 1. A more frequently used approximation (the peak normalized radiance) is discussed in the next section.

### 3.3 Peak Normalized Radiance Approximation

The second level of data reduction involves manipulation of instrument-specific factors to obtain approximate measures of radiance and other similar quantities. In one common method, peak normalization, both sides of Eq. (4) are divided by the quantities  $\lambda_m$  and  $Q(\lambda_m)$ . The definition of  $\lambda_m$  is the wavelength of peak net quantum efficiency; that of  $Q(\lambda_m)$  is the peak net quantum efficiency. The result is the peak normalized radiance  $L_{pn}$ , which is defined as:

$$L_{pn} = \int \lambda Q(\lambda) L(\lambda) d\lambda / \lambda_m Q(\lambda_m). \quad (5)$$

In practice, the evaluation of  $L_{pn}$  is based on the measured  $P_k$ , using:

$$L_{pn} = (P_k/\tau) (hc/\lambda_m) / [A_c \Omega_p Q(\lambda_m)]. \quad (6)$$

Table 7 gives the values of  $\lambda_m$ ,  $Q(\lambda_m)$  and  $\lambda_m Q(\lambda_m)$  for each of the filters and the quantity  $hc/A_c \Omega_p = 2.07 \times 10^{-8}$  J-nm/cm<sup>2</sup>-sr.

Table 7 - Plume Camera Filter,  $\lambda_m$ , and Peak Quantum Efficiency

Filter	$\lambda_m$ (nm)	$Q(\lambda_m)$	$\lambda_m Q(\lambda_m)$ (nm)
Plume PC-1	270	.00606	1.64
Plume PC-2	305	.00182	0.555
Plume PC-3	250	.00284	0.710
Plume PC-4	280	.0131	3.67
Tracker	355	.0200	7.10

Although Eq. (5) is an exact expression, it is not a true radiance because the integral contains terms other than  $L(\lambda)$ .  $L_{pn}$  approaches the true radiance as  $[\lambda Q(\lambda)/\lambda_m Q(\lambda_m)]$  approaches 1. For UVPI,  $\lambda/\lambda_m$  is usually about equal to 1, but  $Q(\lambda)/Q(\lambda_m) \ll 1$  for efficiency curves like PC-1 and PC-3 with long, low wings. On the other hand, efficiency curves for PC-2 and the tracker camera are more box-like, and  $Q(\lambda)/Q(\lambda_m)$  is close to one. This is discussed further in Ref. 1.

Table 8 presents peak normalized radiance values and reference spectrum values obtained from an observation of the Nihka rocket by using estimated  $P_k$  from the brightest pixel only. The ratio of the two radiances is included in the last column. For PC-1, the peak normalized approximation underestimates the reference spectrum result by almost a factor of 10 because of the low efficiency wings.

Table 8 -  $P_k/\tau$  and  $L_{pn}$  for Brightest Pixel

Filter	$P_k/\tau$ (photoevents/s)	$L_{pn}$ ( $\mu$ W/sr-cm <sup>2</sup> )	$L_e$ ( $\mu$ W/sr-cm <sup>2</sup> )	$L_{pn}/L_e$
Plume PC-1	5.29	$6.68 \times 10^{-2}$	$5.47 \times 10^{-1}$	0.12

Thus, the peak normalized radiance is an approximate measure of the total radiance in the passband of the filter. A corrected radiance can be obtained if the true spectrum is used to evaluate the integral [11]. In particular, the peak radiance approximation is exact only for a line spectrum

peaked at  $\lambda_m$  [12]. To gain a better estimate of the true in-band radiance, the approximate shape of the plume spectrum must be known.

### 3.4 Reference Spectrum for Aluminum-Loaded Propellants

The third level of data reduction requires the assumption of a spectrum of the emitting region. The amplitude of the assumed spectrum plays no role, but the shape acts as a weighting function within the passband to determine the distribution of photons as a function of wavelength. This is important because the instrument efficiency is different at each wavelength within a passband and, thus, the implied photon flux at the telescope face for a fixed measurement of photoevents  $P_k$  will depend on how the photons are distributed across that wavelength interval. What is needed is the spectral shape. Such a spectral shape is not provided by the instrument. Fortunately, previous measurements and theoretical predictions can aid in making the assumption, as explained below. The sensitivity of the resulting radiometric numbers to several different spectral shapes is discussed in Section 4.5 of Ref. 1.

The solid rocket motors under consideration contain powdered aluminum in their propellant. This aluminum oxidizes and emerges as an incandescent mist in the rocket exhaust. It is this mist of oxidized aluminum particles or droplets that emits much of the UV radiation seen by UVPI in the plume central region. This mist is optically thin. The plumes are, thus, partially transparent. Because the heat of fusion for aluminum oxide is very high, and the rate of cooling for micron-sized particles is relatively low, the particles remain at roughly their melting temperature throughout the length of the plume. Thus, most of the light in the plume will be from this nearly transparent cloud of micron-sized  $Al_2O_3$  particles at their melting point, 2320 K.

The assumed spectral shape used is that of a 2300 K blackbody times an emissivity function  $\epsilon_{Al}(\lambda)$ , shown in Fig. 27 [13]. This emissivity curve is basically characteristic of hot alumina particles of the size found in rocket exhaust plumes [9].

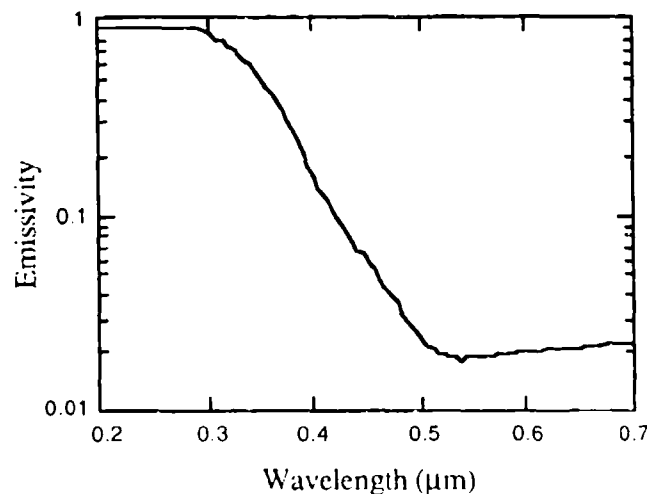


Fig. 27 - Emissivity curve for aluminum particles in rocket plumes

The resulting normalized spectral shape is fairly generic to all solid-fueled boosters with aluminum-loaded fuel and is termed the reference spectrum  $R(\lambda)$ . Mathematically,

$$R(\lambda) = \epsilon_{Al}(\lambda) L_{BB}(\lambda), \quad (7)$$

where  $L_{BB}(\lambda)$  is the 2300 K blackbody spectrum. Figure 28 shows the reference spectrum compared to a blackbody spectrum.

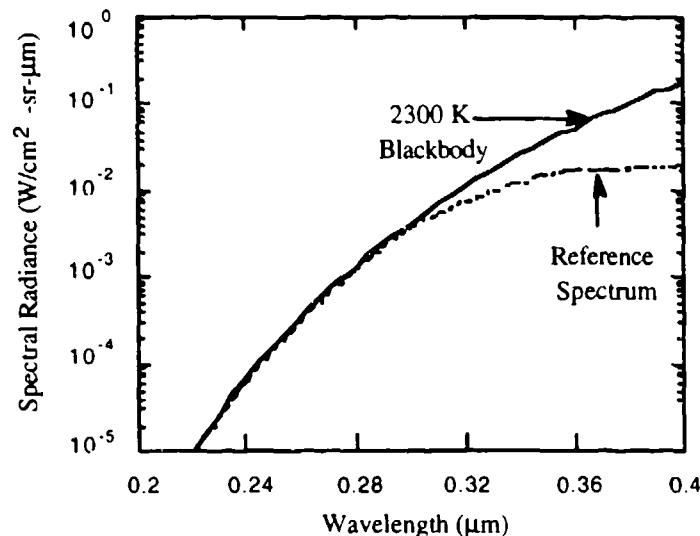


Fig. 28 - Assumed reference spectrum

The spectral shape is a good approximation to actual rocket plume spectra as verified by on-board spectrometers looking back into rocket plumes [14].

### 3.5 Use of the Reference Spectrum to Calculate a Scaling Constant

Assuming that the reference spectrum  $R(\lambda)$  gives the proper spectral shape for  $L(\lambda)$  is equivalent to saying that  $L(\lambda)$  and  $R(\lambda)$  are related by a scaling constant  $\alpha$ , which is independent of  $\lambda$ :

$$\alpha = L(\lambda)/R(\lambda). \quad (8)$$

The scaling factor  $\alpha$  for a pixel can be obtained by first calculating the number of photoevents expected for the unscaled reference spectrum  $P_k'$  by using the expression

$$P_k' = (A_c \Omega_p \tau / hc) \int \lambda Q(\lambda) R(\lambda) d\lambda, \quad (9)$$

where the calculated value is the same for all  $k$  (i.e.,  $k$  is superfluous). Then, by using the ratio of Eq. (3) to Eq. (9), namely,

$$\frac{P_k}{P_k'} = \frac{\int \lambda Q(\lambda) L(\lambda) d\lambda}{\int \lambda Q(\lambda) R(\lambda) d\lambda} = \frac{\alpha \int \lambda Q(\lambda) R(\lambda) d\lambda}{\int \lambda Q(\lambda) R(\lambda) d\lambda} = \alpha_k \quad (10)$$

Therefore,  $\alpha_k$  can be estimated for each passband and for each pixel by comparing the measured value of  $P_k$  to the calculated value,  $P_k'$ :

$$\alpha_k = P_k / P_k' \quad (11)$$

which gives an in-band, effective value of  $\alpha_k$  for that pixel. Actually, these plumes are optically thin, and  $\alpha_k$ , in some sense, provides a measure of the thinness or density of emitters along the line of sight of that pixel.

After  $\alpha$  is known, the source spectral radiance function  $L(\lambda)$  can be calculated by using Eq. (8) and this, in turn, is used to calculate in-band total radiance for the plume data in various filter bandpasses. All the radiometric values presented in this paper can be obtained from the source

function  $L(\lambda)$  defined by Eqs. (8) and (11). The values for  $P_k/\tau$  and  $P_k'/\tau$ , obtained as an average for the brightest pixel over several frames for the Nihka plume, are given in Table 9.

Table 9 - Photoevents per Second from Nihka Plume and Reference Spectrum Model for Brightest Pixel and Ratios of These Values

Filter	$P_k/\tau$ (PE/s)	$P_k'/\tau$ (PE/s)	$\alpha_k$
Plume PC-1	5.29	$1.81 \times 10^3$	$2.92 \times 10^{-3}$

### 3.6 Centroid Wavelength Determination

The procedure above yields a function  $L(\lambda)$  describing the amplitude of the spectral shape that corresponds to the observed number of photoevents. Describing this function with a single numerical value is difficult because of the extremely rapid variation of the spectral radiances evident in Figs. 31, 32, and 33 (found in Section 4). It is sometimes desirable to provide single numerical values of plume spectral radiance and spectral radiant intensity despite this rapid variation. This is achieved simply by taking  $L(\lambda)$  of Eq. (8) at a specific characteristic wavelength  $\lambda_c$  for each filter passband. This might have been selected to be the center of each filter passband, but this choice would neglect the shift in the effective response resulting from the spectrally varying source. A response centroid wavelength, weighted by the reference spectral function, was defined:

$$\lambda_c \equiv \int \lambda^2 R(\lambda) Q(\lambda) d\lambda / \int \lambda R(\lambda) Q(\lambda) d\lambda. \quad (12)$$

This describes the wavelength of average contribution to the UVPI response for each filter. These centroid wavelengths were computed for various spectral shapes and are shown in Table 10. The integrals of Eq. (12) have been evaluated as discrete summations over the range of  $Q(\lambda)$  that is not negligible. *The numbers in parentheses under the exact reference spectrum values are the rounded values that are actually used throughout this report.*

Table 10 - Centroid Wavelength,  $\lambda_c$ , for Various Spectra

	PC-1 (nm)	Tracker (nm)
1800 K Blackbody	282.4	416.2
2300 K Blackbody	279.2	409.7
Reference spectrum (rounded)	279.1 (280)	389.4 (390)
Flat spectrum	270.7	369.5
Peak normalized	270.0	355.0

Defining  $\lambda_c$  is simply a means of selecting a nominal characteristic wavelength for describing the result of the fitting of the spectral shape to the instrument measurement as single numerical values. Other procedures might have been used for selecting a reference wavelength to describe the spectral radiance function. One might, for example, have taken the central wavelength for each filter and cited the numerical value of the fit function at those wavelengths. This would yield different values for the nominal spectral radiances without changing the function  $L(\lambda)$  at all. In short, these single numerical values for the rapidly varying spectral radiometric parameters must be treated with caution.

### 3.7 Calculations of Radiance and Radiant Intensity

After the spectral radiance is known, the spectral integrals can be evaluated to obtain values for the radiance:

$$L_e \equiv \int_{\lambda_L}^{\lambda_U} L(\lambda) d\lambda = \alpha \int_{\lambda_L}^{\lambda_U} R(\lambda) d\lambda. \quad (13)$$

The units of  $L_e$  are (power)/(area)(solid angle), or W/m<sup>2</sup>-sr. The evaluation of these integrals is limited to the nominal bandwidth of the pertinent filter. Note that the integrand of Eq. (13) does not include the response function  $Q(\lambda)$  and, therefore, does not become small outside the filter passbands. The values obtained for  $L_e$  depend very strongly on the limits of integration.

Conversion to radiant intensity can be achieved from the preceding expressions by multiplying by  $R^2\Omega_p$ , where  $R$  is the range to the source and  $\Omega_p$  is the pixel field of view. This is then summed over the pixels containing signal. The result is equivalent to summing the apparent radiance or spectral radiance over the projected pixel area and attributing it to a point source within the field of view of the pixel. The spectral radiant intensity  $I(\lambda)$  and the radiant intensity  $I_e$  can be obtained directly from the corresponding expressions for the spectral radiance and radiance, Eq. (8) and Eq. (13), respectively:

$$I(\lambda) = R^2\Omega_p L(\lambda) = R^2\Omega_p \alpha R(\lambda), \quad (14)$$

and

$$I_e \equiv \int_{\lambda_L}^{\lambda_U} I(\lambda) d\lambda = R^2\Omega_p L_e. \quad (15)$$

The units of  $I(\lambda)$  are (power)/(spectral bandwidth)(solid angle), or W/nm-sr, and the units of  $I_e$  are (power)/(solid angle), or W/sr. As with the radiance, the radiant intensity is an integral across a limited portion of the spectrum defined by the nominal filter edges. The value so obtained is far smaller than that for the full-spectrum radiant intensity. It will also be very sensitive to the limits of integration chosen for Eq. (15).

### 3.8 Summary of Radiometric Conversion Constants

Table 11 summarizes the definitions of conversion constants most often encountered in calculating one radiometric quantity from another. Table 12 gives the specific values for the conversion constants based on the assumed reference spectrum. Any revised spectral shape assumption will lead to a different set of conversion constants. Table 13 lists the radiometric values corresponding to one photoevent per second. The radiant intensity values refer to a range of 500 km. The values of the spectral radiance  $L(\lambda_c)$  and the radiance  $L_e$  are based on a single photoevent per second per pixel. Any arbitrary number of photoevents measured in a particular pixel is multiplied by the value in the table to determine the radiance of the source in that pixel's field of view. The values of the spectral radiant intensity  $I(\lambda_c)$  and radiant intensity  $I_e$  are per pixel, even though these terms are used more often to refer to the total number of photoevents measured in the entire plume image.

Note that the conversion constants associated with  $I(\lambda_c)$  and  $I_e$  use the rounded reference spectrum centroid wavelength values shown in parentheses in Table 10.

Table 11 - Summary of Formulas Defining Conversion Constants

From	To	Operation	Formula
$P_k/\tau$ (photoevents/s)	$\phi_{in}$ (photons/s)	*C1	$C_1 = \frac{\int \lambda R(\lambda) d\lambda}{\int \lambda R(\lambda) Q(\lambda) d\lambda}$
$\phi_{in}$ (photons/s)	$P_{in}$ (W)	*C2	$C_2 = \frac{hc \int R(\lambda) d\lambda}{\int \lambda R(\lambda) d\lambda}$
$P_{in}$ (W)	$I_e$ (W/sr)	+C3	$C_3 = A_c/R^2$
$L_e$ (W/sr-cm <sup>2</sup> ) $I_e$ (W/sr)	$L(\lambda_c)$ (W/cm <sup>2</sup> -sr-nm) $I(\lambda_c)$ (W/sr-nm)	+C4	$C_4 = \frac{\int \lambda L(\lambda) d\lambda}{L(\lambda_c)}$
$I_e$ (W/sr) $I(\lambda_c)$ (W/sr-nm)	$L_e$ (W/cm <sup>2</sup> -sr) $L(\lambda_c)$ (W/cm <sup>2</sup> -sr-nm)	+C5	$C_5 = R^2 \Omega_p$

Table 12 - Conversion Constants for the Reference Spectrum

Constant	Units	PC-1 ( $\lambda_c = 280$ nm)	Tracker ( $\lambda_c = 390$ nm)
C1	photons/PE	1510	66.2
C2	joules/photon	$6.61 \times 10^{-19}$	$5.11 \times 10^{-19}$
C3	steradians	$3.12 \times 10^{-14}$	$3.12 \times 10^{-14}$
C4	nm	150.2	125.2
C5	cm <sup>2</sup>	$30.6 \times 10^4$	$6507 \times 10^4$

Table 13 - Radiometric Values for One Photoevent Per Second

Units	PC-1 ( $\lambda_c = 280$ nm)	Tracker ( $\lambda_c = 390$ nm)
$P_k/\tau$ (photoevents/s)	1	1
$\phi_{in}$ (photons/s)	1510	66.2
$P_{in}$ (W)	$9.95 \times 10^{-16}$	$3.38 \times 10^{-17}$
$I_e$ (W/sr)	$3.17 \times 10^{-2}$	$1.08 \times 10^{-3}$
$I(\lambda_c)$ (W/sr-nm)	$2.11 \times 10^{-4}$	$8.60 \times 10^{-6}$
$L_e$ (W/sr-cm <sup>2</sup> )	$1.04 \times 10^{-7}$	$1.66 \times 10^{-11}$
$L(\lambda_c)$ (W/sr-cm <sup>2</sup> -nm)	$6.90 \times 10^{-10}$	$1.32 \times 10^{-13}$

#### 4.0 PLUME DATA

In this section the observed plume data are presented. The data interval used in this report is defined in 4.1, and an overview of the intensity history for each camera is given in 4.2. Examples of single-plume camera images are given in 4.3. Composite images with corresponding contour plots for the defined data interval for the plume and tracker cameras are presented in 4.4 and 4.5, respectively. Subsection 4.6 discusses the error in the radiometric observations. The concluding subsection, 4.7, discusses the noise-equivalent radiance for the UVPI.

## 4.1 Data Collection Interval

### 4.1.1 Description

Table 14 summarizes the Nihka data collection interval used in this report. Also included are the number of plume camera images and tracker camera images analyzed. Table 15 reports important calibration parameters associated with the interval. The UVPI-Nihka range is used to determine source radiant intensity, as discussed in 4.2. The image angle variation associated with a sequence of frames is a measure of the variation in plume image axis orientation with respect to TV lines in the image display. This parameter is relevant to the spatial analysis presented in Section 5.0.

Table 14 - Definition of the Data Interval

GMT	TALO (s)	Plume Camera Filter	Telemetry Frame Range	No. of Plume Images	No. of Tracker Images
7:07:15.03- 7:07:22.24	185.0-- 192.9	PC-1	11603- 11810	96	40

Table 15 - Parameters Associated with the Data Interval

Plume Camera Filter	Bandpass (nm)	Plume to Tracker Ratio	UVPI- Nihka Range (km)	Image Angle Variation (deg)
PC-1	220-320	8:2	450.7	12.1

The Nihka plume was first observed in the plume camera around frame 11500. Because of gain changes and ensuing transients in the plume camera, data analysis was limited to the interval summarized in Table 14. Approximately 3.2 s of filter 1 data were collected during this time. Analysis of tracker-camera data was restricted to the same interval.

### 4.1.2 Calibration Parameters Associated with the Data Interval

Appendix B provides basic camera parameters pertinent to the radiometric calibration of the data for all frames during which the Nihka was observed. Parameters provided include time, telemetry frame number, gain level for both cameras, and exposure time for both cameras. The plume camera has a constant  $1/30$ th of a second exposure time for each frame. The tracker camera has an electronic gate that can vary the exposure time to a maximum of  $1/30$ th of a second. Figure 29 shows the camera gain levels for both tracker and plume cameras. Figure 30 shows exposure time for both cameras as a function of telemetry frame number. Reference 1 provides additional information used for radiometric calibration.

## 4.2 Intensity History Overview

As a quick overview, Figs. 31 and 32 show plume-camera long-term trends in the central region and total spectral radiant intensity, respectively. The values plotted were derived by assuming the reference spectral shape. Figure 33 shows similar results for the tracker-camera total spectral radiant intensity in a 19 by 19 pixel region containing the plume-camera field of view. For these figures, all curves specify spectral radiant intensity at the reference centroid wavelength for each interval. Note that both the plume and the tracker camera total radiant intensities show pronounced upward trends. This trend is much less pronounced in the plume central region spectral radiant intensity. The fact that the upward trend is greater in the plume camera than in the tracker camera total spectral radiant intensity, roughly 50% vs 20%, can be interpreted to mean that the increasing emission is peaked in the far-UV rather than the near-UV or visible.

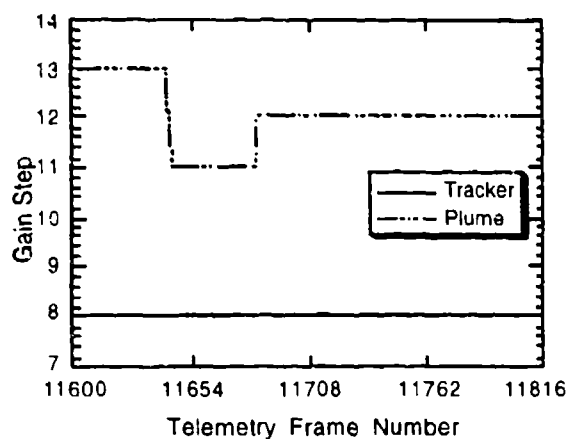


Fig. 29 - Tracker and plume camera gain

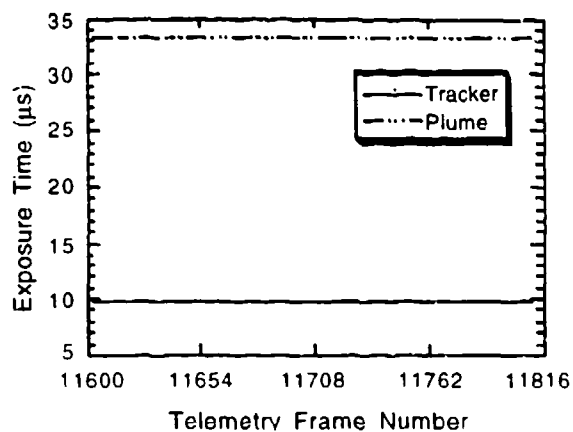


Fig. 30 - Tracker and plume camera exposure times

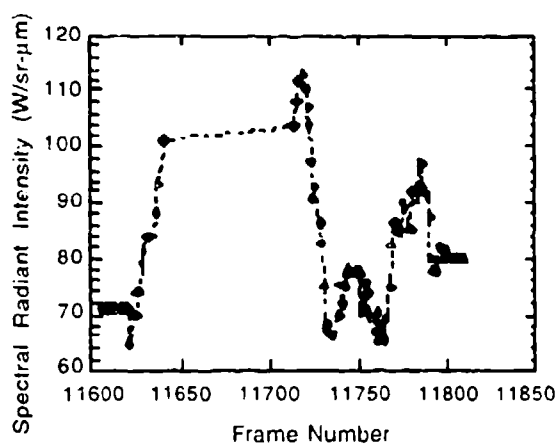


Fig. 31 - Spectral radiant intensity, plume camera, central region

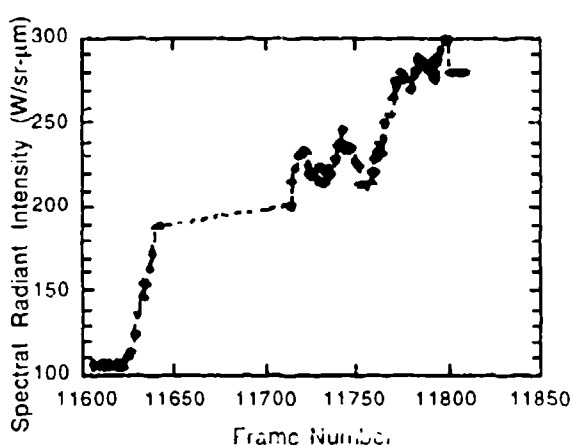


Fig. 32 - Spectral radiant intensity, plume camera, total region

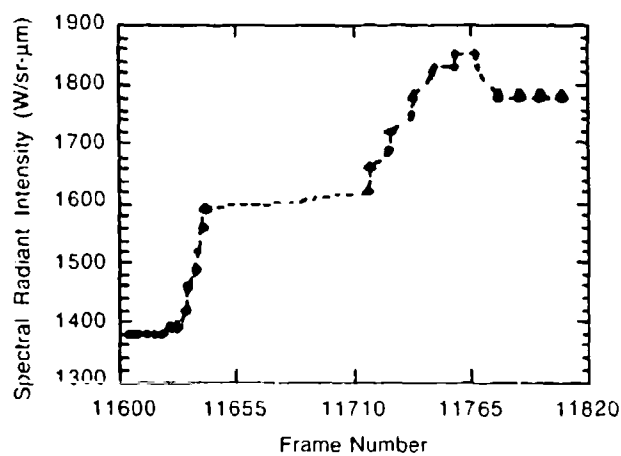


Fig. 33 - Spectral radiant intensity, tracker camera

### 4.3 Single Images

This subsection presents raw plume image data. Given the characteristics of the UVPI cameras, e.g., exposure time, optics aperture, and the rocket plume radiant intensity, the number of photoevents that are registered within the focal plane array of a camera can be individually counted as isolated events. In this respect, UVPI can be used as a photon-counting instrument.

Figure 34 shows single images, in zoom image transmission rate, of the Nihka burn. Pixel radiance is encoded as image brightness, where dark and bright are, respectively, relatively smaller and larger radiance. The images demonstrate that the shapes of the plume central region and outer region are not necessarily clearly delineated in a single frame.

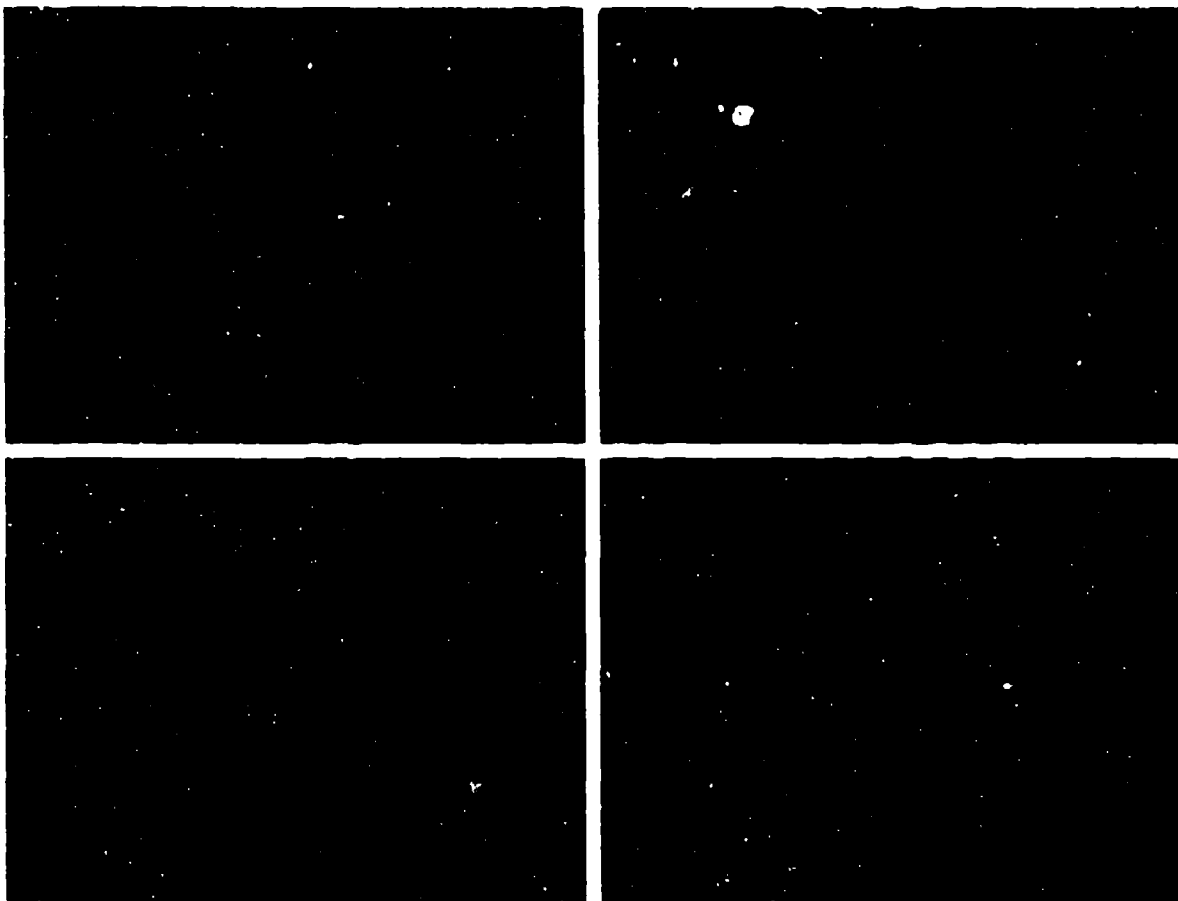


Fig. 34 - Single unprocessed plume camera images of the Nihka plume

Every bright spot on the image corresponds to one or more photoevents that pile up at that particular pixel during the exposure time of the camera. Figure 35 illustrates the number of photoevents per second measured at each pixel location in the center 64 by 64 pixels of the lower-left-corner image shown in Fig. 34. The  $z$  axis corresponds to the number of photoevents per second while the  $x$  and  $y$  axes correspond to row and column indices. The actual procedure used to compute the number of photoevents from the measured digital number in the UVPI telemetry stream was discussed in Section 3 and in Ref. 1.

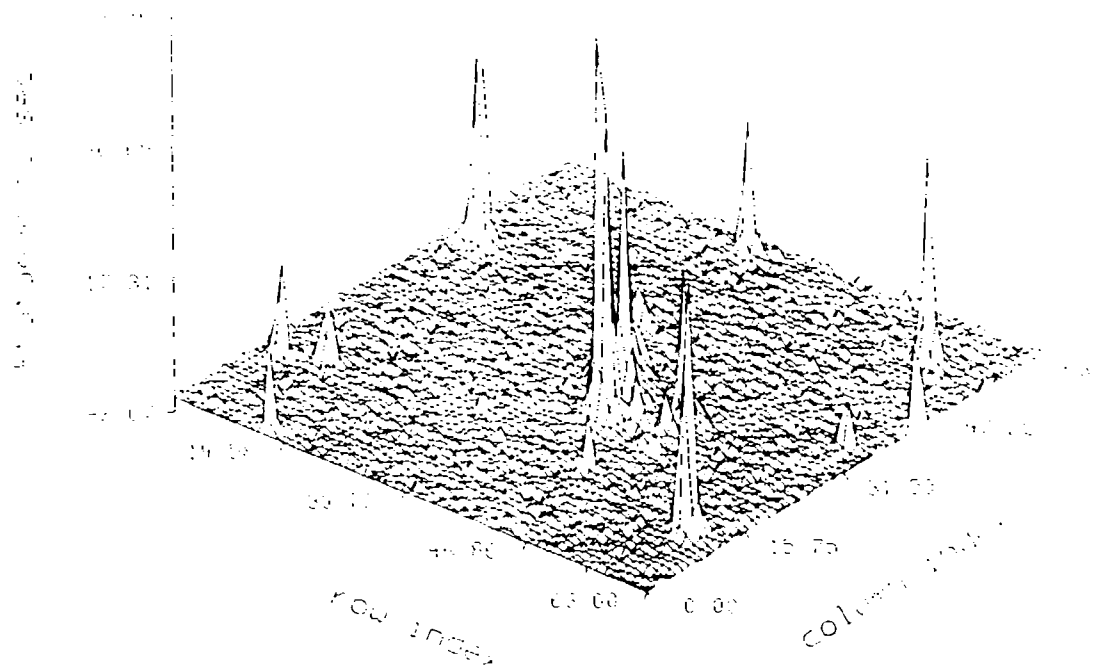


Fig. 35 - Single image of the Nihka plume

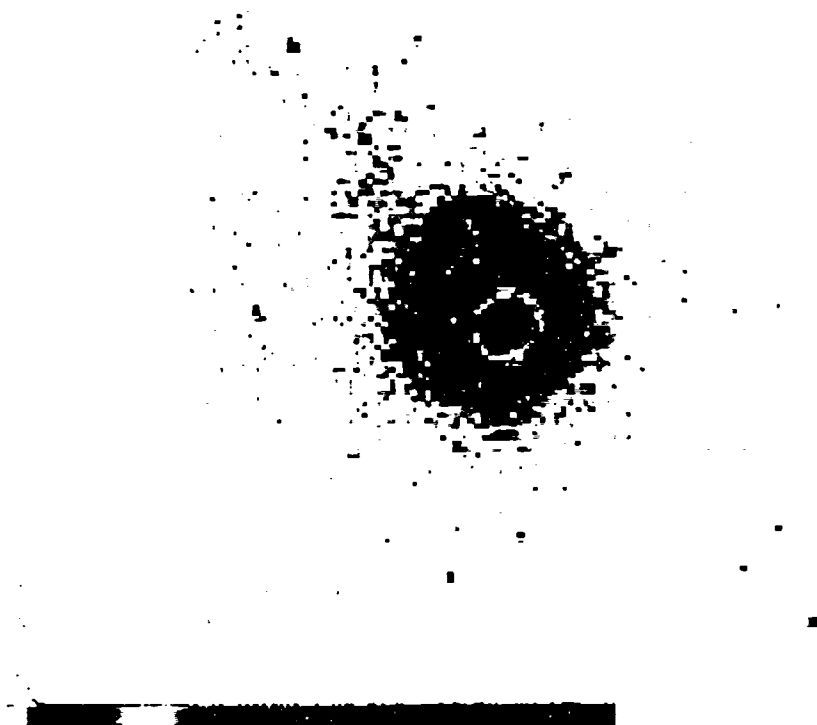
#### 4.4 Composite Plume Camera Images and Contour Plots

In this subsection a composite plume-camera image and its corresponding contour plot are presented, showing the spatial distribution of the time-averaged plume radiance. The composite image is made from calibrated versions of images formed while observing the Nihka during the data interval summarized in Table 14 of Section 4. As explained in Section 3, the reference emission spectrum is assumed to convert UVPI measurements into units of radiance, i.e.,  $W/sr\text{-cm}^2$ . The plume-to-tracker image ratio is 8:2, and the exposure time for individual plume camera images is  $1/30$ th of a second. Many individual images are superposed to form the composite image.

The limiting resolution of the UVPI cameras is described by the point spread function. Observation of a ground-based beacon, a source less than 5 m across, shows that the full-width-half-maximum of the point source response in the plume camera is about 9 pixels, or about  $90 \mu\text{rad}$ , which is equivalent to 40 m at a 450-km range. Figure 36 shows a plume-camera image of the beacon on the same scale as the plume image that follows. This is representative of the plume camera's point spread function. Figure 37 shows the contour plot for the ground beacon, a point source, on the same scale as Fig. 38. Figure 37 shows the resolution of the plume camera contour plots that result from the point spread function.

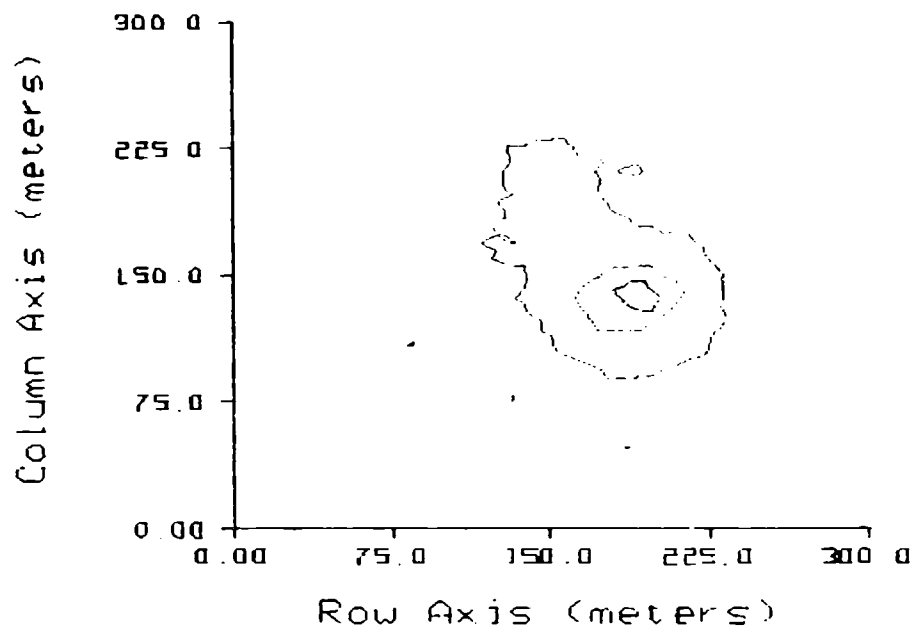
Figure 38 shows the calibrated plume-camera PC-1 composite image acquired during the interval defined in Table 14 of Section 4. In this image the radiant intensity has been mapped to a false-color scale, with black representing the highest intensity, light blue the middle intensity, and white the lowest intensity. A horizontal color bar depicting the mapping of radiant intensity into colors is shown on the lower left corner. A histogram of the image intensity values is shown above the color bar in the form of dark dots.

Figure 39 shows the contour plot for the data interval. The black, blue, and red contours represent, respectively, plume radiance contours at 95%, 50%, and 9.5% of the maximum radiance in the image. The radiance units are watts per steradian per square centimeter, and the horizontal and vertical axes are scaled in meters.



Observing sensor:	UVPI
Target observed:	UVPI ground-based beacon
Orbit number:	1173
Range of frames used:	12778-12778
Camera:	Plume
Displayed image size (pixels):	112 (vertical) x 91 (horizontal)
Average range (km):	450

Fig. 36 - Plume camera image of ground-based beacon illustrating the point spread function



**| =0.095\*max | =0.50\*max | =0.95\*max**

Observing sensor:	UVPI
Target observed:	UVPI ground-based beacon
Orbit:	1173
Range of frames used:	12778-12778
Camera:	Plume
Average range (km):	450

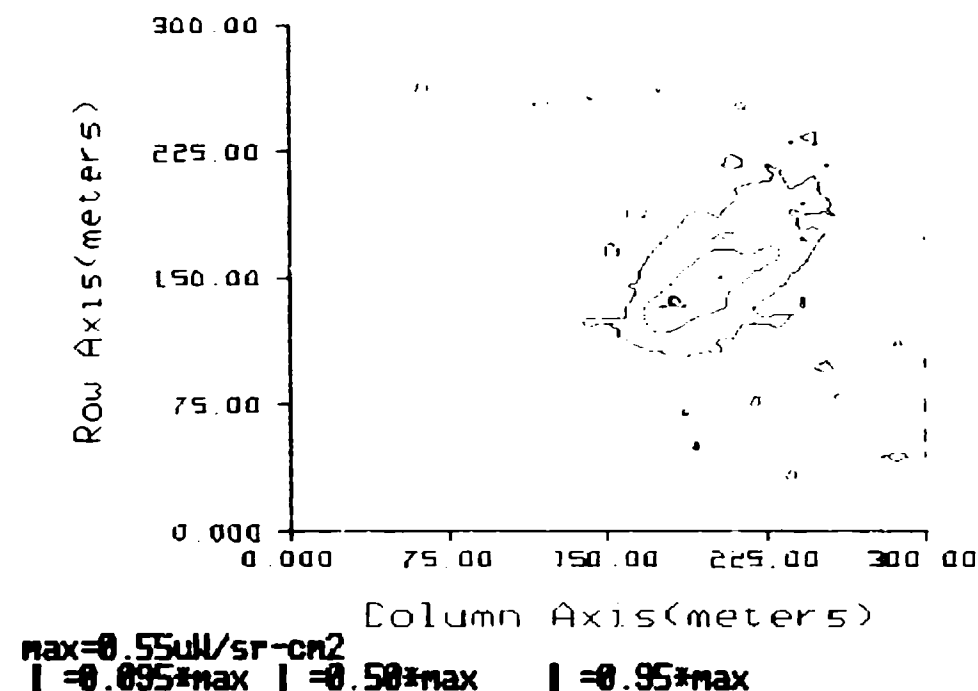
Fig. 37 - Plume camera contour plot for ground-based beacon



Observing sensor:	UVPI (Aug. 25, 1990)
Target observed:	Nihka
Range of frames used:	11603-11810
Number of superposed images:	96
Camera:	Plume
Spectral band (nm):	220-320 (PC-1)
Displayed image size (pixels):	112 (vertical) x 91 (horizontal)
Average range (km):	450.7
Pixel footprint (m) @ range:	4.42 (vertical) x 5.63 (horizontal)
Aspect angle (deg):	56.7
*Total photoevents/s:	$1.35 \times 10^3$
*Total radiant intensity (W/sr):	34.6
*Total spectral radiant intensity @ 270 nm (W/sr- $\mu\text{m}$ ):	231.0
*Error (%):	11.5%

\*For full image.

Fig. 38 - Composite plume-camera image



Observing sensor:	UVPI (Aug. 25, 1990)
Target observed:	Nihka
Range of frames used:	11603-11810
Number of superposed images:	96
Camera:	Plume
Spectral band (nm):	220-320 (PC-1)
Displayed image size (pixels):	90.6 (vertical) x 71.0 (horizontal)
Average range (km):	450.7
Pixel footprint (m) @ range:	4.42 (vertical) x 5.63 (horizontal)
Aspect angle (deg):	56.7
*Photoevents/s:	5.29
*Apparent peak radiance ( $\mu\text{W}/\text{sr}\cdot\text{cm}^2$ ):	$5.47 \times 10^{-1}$
*Apparent peak spectral radiance @ 280 nm ( $\mu\text{W}/\text{sr}\cdot\text{cm}^2\cdot\mu\text{m}$ ):	3.65

\*For brightest pixel.

Fig. 39 - Plume camera contour plot

Because of the UVPI's dynamic range of 256 levels in the analog-to-digital converter, it is difficult to get well-defined plume contours at levels below 9.5% of the maximum radiance unless a large number of images are superposed. With each picture or plot, a companion summary table provides relevant information for the quantitative interpretation of the image or plot. The parameters presented in these tables are described in Table 16.

Table 16 - Basic Parameters

Aspect angle	Angle, in degrees, between the line of sight and the rocket body longitudinal vector.
Average range	Average distance, in kilometers, between UVPI and the plume target.
Camera	Camera used, either tracker or plume.
Displayed image size	Size in pixels (picture elements) of the image being displayed.
Number of superposed images	Number of images averaged together to generate the composite image. Because of the tracker-to-plume image ratio, this number is not equal to the number of frames in the range.
Pixel footprint	Projected pixel dimensions, in meters, at target range. This number does not account for any spreading introduced by the optics or jitter since it incorporates only the instantaneous field of view.
Range of frames used	Range of frames containing the set of tracker or plume camera images superposed.
Spectral band	Spectral band, in nanometers, covered by all images within the set. This band includes more than 99% of the net quantum efficiency response curve.
Target observed	Nihka
Total photoevents/s	Sum of all photoevent-per-second pixel values over the specified region of the focal plane.
Total radiant intensity (W/sr)	Radiant intensity associated with total photoevents per second.
Total spectral radiant intensity (W/sr- $\mu\text{m}$ )	Spectral radiant intensity at the specified centroid wavelength associated with the total photoevents per second.
Apparent peak radiance ( $\mu\text{W/sr-cm}^2$ )	Apparent radiance measured at the brightest pixel in an image. Because of the size and structure of UVPI's point spread function, the value given is not likely to be a good measure of the true peak radiance at the source. The value is useful for rough comparisons and order-of-magnitude estimates.
Apparent peak spectral radiance ( $\mu\text{W/sr-cm}^2\text{-}\mu\text{m}$ )	Apparent spectral radiance at the specified centroid wavelength measured at the brightest pixel in an image. Because of the size and structure of UVPI's point spread function, the value given is likely not to be a good measure of the true peak spectral radiance at the source. The value is useful for rough comparisons and order-of-magnitude estimates.
Error (%)	Total error associated with the above radiometric values. This error includes gain conversion factor error and the error attributable to photon shot noise and detector noise. The error estimate is based on the total number of images superposed. See Section 4.6 for in-depth discussion.

Table 17 shows the maximum apparent pixel radiance measured for the brightest pixel and also the apparent peak spectral radiance reported at the specified centroid wavelength. The values given are primarily useful for rough comparisons and order-of-magnitude estimates due to the size and structure of UVPI's point spread function. Estimates of true source peak radiance require further analysis. A comparison of UVPI apparent radiance measurements with CHARM 1.3 code predictions is presented in Section 5.3.

Table 17 - Plume Camera Apparent Peak Radiometric Values

Filter	Apparent Peak Radiance ( $\mu\text{W/sr-cm}^2$ )	Apparent Peak Spectral Radiance ( $\mu\text{W/sr-cm}^2\text{-}\mu\text{m}$ )	Centroid Wavelength (nm)
PC-1	$5.47 \times 10^{-1}$	3.65	280

During the data interval the apparent rocket velocity vector changes slightly. The velocity is directed out of the page towards the viewer at an angle that is the complement of the aspect angle shown in Fig. 8. Over the observation period, the direction of the rocket velocity vector projected on the image plane changed by  $12.07^\circ$ . The mean direction of the motion is given in Table 18.

Table 18 - Apparent Velocity Vector Direction During Observation

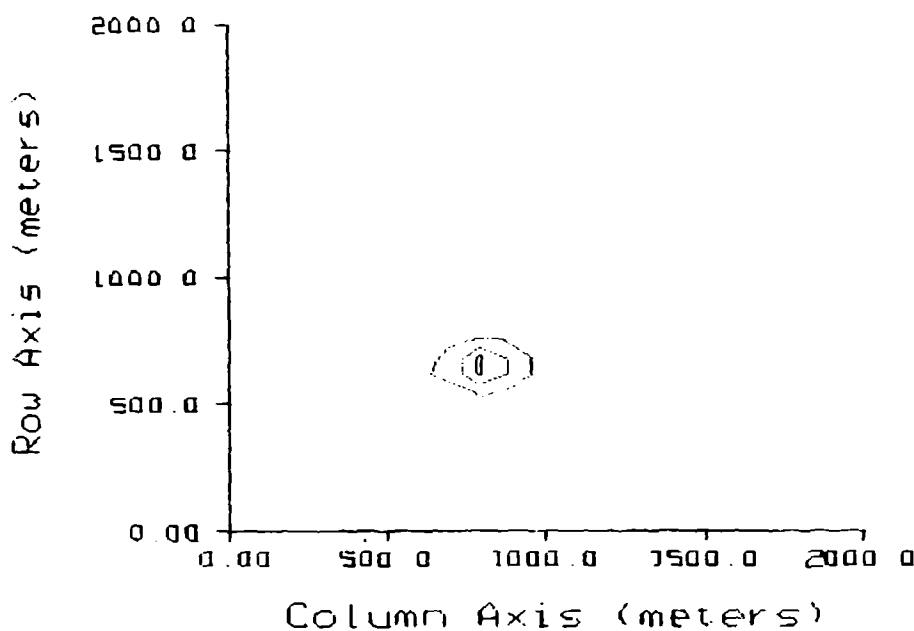
Filter	Mean Direction of Motion Relative to Tracker Camera X Axis	Change in Direction
PC-1	-53.5°	12.07°

#### 4.5 Calibrated Tracker Camera Images

While the plume camera gathered a lower rate because of the plume

rocket plume images, the tracker camera gathered images at a higher image ratio. The tracker camera's exposure time was 9.66 ms during the data interval.

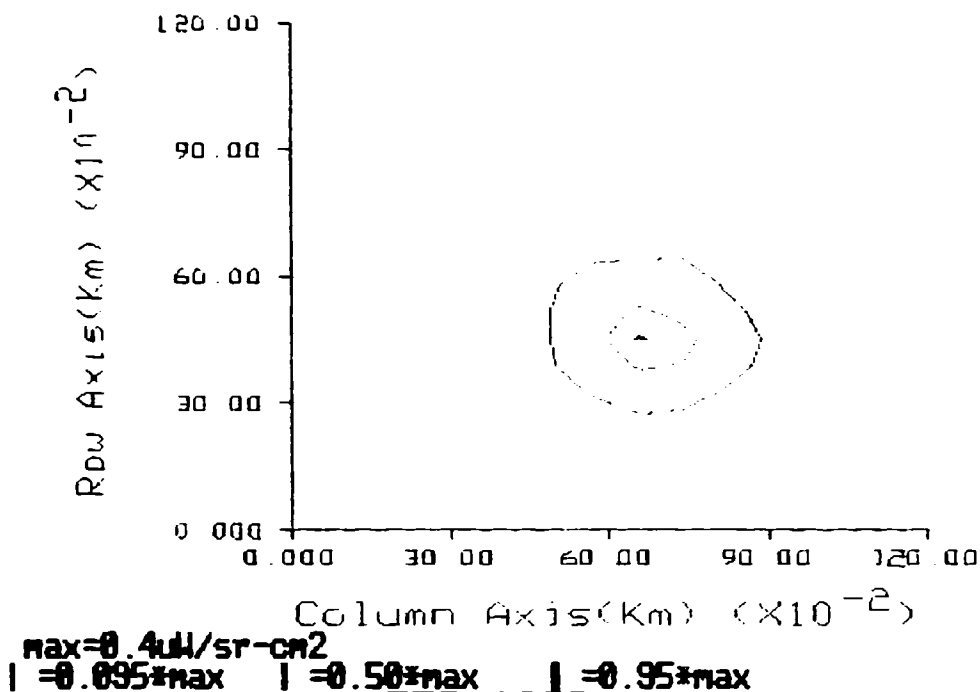
The limiting resolution of the UVPI cameras is described by the point spread function. Observation of the ground-based beacon, a source less than 5 m across, showed that the full-width-half-maximum of the point source response in the tracker camera is about 1.5 pixels, or about 230  $\mu$ rad. This is equivalent to 104 m at 450-km range. Figure 40 is a tracker camera contour plot of the ground-based beacon. This is representative of the tracker camera's point spread function and can be compared with the tracker camera contour plot shown in Fig. 41. Figure 42 shows a tracker camera image of the ground-based beacon on the same scale as the composite tracker-camera image shown in Fig. 43.



$I = 0.095 \times \max$     $I = 0.50 \times \max$     $I = 0.95 \times \max$

Observing sensor:	UVPI
Target observed:	UVPI ground-based beacon
Orbit number:	1173
Range of frames used:	12772-12772
Camera:	Tracker
Displayed image size (pixels):	112 (vertical) x 91 (horizontal)
Average range (km):	450

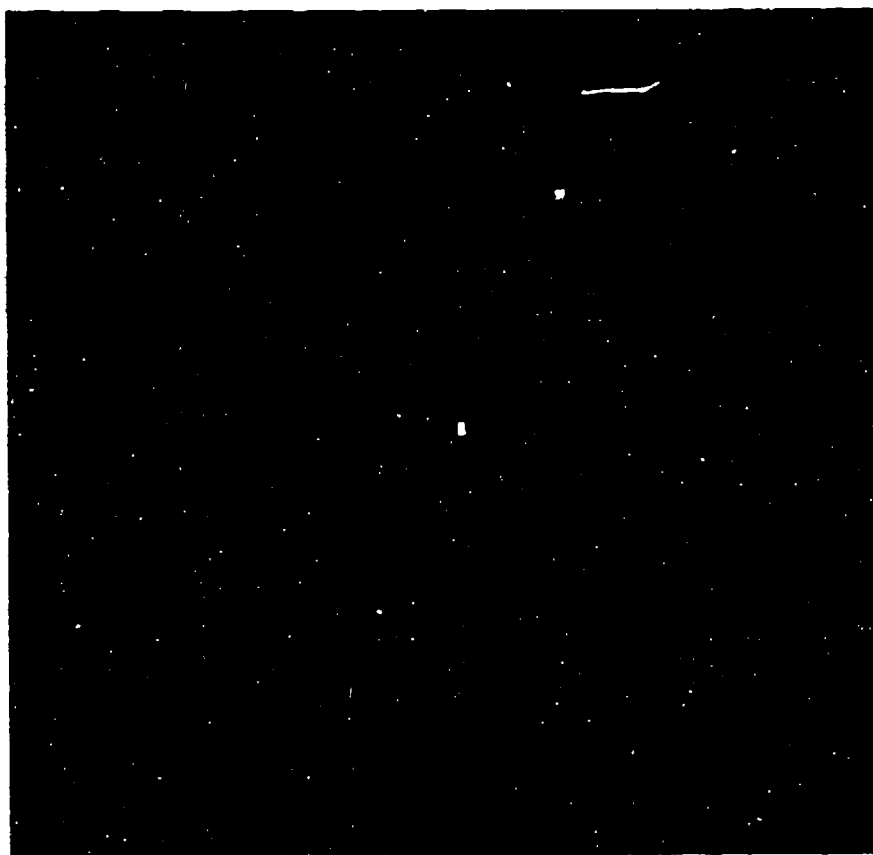
Fig. 40 - Tracker camera contour plot for ground-based beacon



Observing sensor:	UVPI (Aug. 25, 1990)
Target observed:	Nihka
Range of frames used:	11603-11810
Number of superposed images:	40
Camera:	Tracker
Spectral band (nm):	255-450
Displayed image size (km):	2 (vertical) x 2 (horizontal)
Average range (km):	450.7
Pixel footprint (m) @ range:	64.4 (vertical) x 82.0 (horizontal)
Aspect angle (deg):	56.7
*Photoevents/s:	$2.44 \times 10^4$
*Apparent peak radiance ( $\mu\text{W}/\text{sr}\cdot\text{cm}^2$ ):	$4.04 \times 10^{-1}$
*Apparent peak spectral radiance @ 390 nm ( $\mu\text{W}/\text{sr}\cdot\text{cm}^2\cdot\mu\text{m}$ ):	3.22

\*For brightest pixel.

Fig 41 - Tracker camera contour plot



<b>Observing sensor:</b>	UVFI
<b>Target observed:</b>	UVPI ground-based beacon
<b>Orbit number:</b>	1173
<b>Range of frames used:</b>	12772-12772
<b>Camera:</b>	Tracker
<b>Displayed image size (pixels):</b>	112 (vertical) x 91 (horizontal)
<b>Average range (km):</b>	450

Fig. 42 - Tracker camera image of ground-based beacon illustrating the point spread function



<b>Observing sensor:</b>	UVPI (Aug. 25, 1990)
<b>Target observed:</b>	Nihka
<b>Range of frames used:</b>	11603-11810
<b>Number of superposed images:</b>	40
<b>Camera:</b>	Tracker
<b>Spectral band (nm):</b>	255-450
<b>Displayed image size (pixels):</b>	112 (vertical) x 91 (horizontal)
<b>Average range (km):</b>	450.7
<b>Pixel footprint (m) @ range:</b>	64.4 (vertical) x 82.0 (horizontal)
<b>Aspect angle (deg):</b>	56.7
<b>*Total photoevents/s:</b>	$1.97 \times 10^5$
<b>*Total radiant intensity (W/sr):</b>	$1.72 \times 10^2$
<b>*Total spectral radiant intensity @ 390 nm (W/sr-<math>\mu\text{m}</math>):</b>	$1.37 \times 10^3$
<b>*Error (%):</b>	15.8

\*For central 19 x 19 pixels.

Fig. 43 - Composite tracker camera image

With each picture or plot a companion summary table provides relevant information for quantitative interpretation. The parameters presented in these tables are described in Table 16. Radiometric values reported in the table accompanying each figure are for the central 19 by 19 pixels of the tracker camera. This field of view approximately matches the total field of view of the plume camera. It contains the plume central region and a portion of the outer region. Therefore, it cannot reliably be converted to radiant intensity or spectral radiant intensity. However, to provide estimates of the radiant intensity and spectral radiant intensity, values based on reference spectral energy distribution assumptions are reported for the tracker camera observations. These results have been reduced by 16.3% to account for red leakage in the tracker-camera filter.

#### 4.6 Error Analysis for Radiometric Observations

The complete estimate of the error in determining radiometric values from the digital numbers reported by the UVPI cameras observing a rocket plume is composed of two components: measurement noise, summarized in 4.6.1, which includes photon shot noise and other intrinsic sensor noise sources; and calibration error (summarized in 4.6.2), which is the error contained in the gain conversion factor. Section 4.6.3 summarizes the calculation of the total error based on the error components presented in 4.6.1 and 4.6.2. Detailed discussions of error estimates are found in Ref. 1.

##### 4.6.1 Error Resulting from Measurement Noise

As a result of photon shot noise, the error in the calculated number of photoevents changes as a function of the plume radiant intensity, which could change as a function of time. This error analysis assumes that the radiant intensity statistics are not affected by a small shift in time. A window size of 15 consecutive images was selected for the statistical analysis of the plume-camera data, and a window of 15 consecutive images was selected for the tracker-camera analysis. A larger time window could be used but with the risk of making the locally constant assumption invalid.

Given the number of photoevents as a function of image, the following quantities are defined:

- $M$  - number of images in data interval,
- $N$  - number of images used within the window,
- $\mu_i$  - local mean over  $N$  images around  $i$ th image,
- $\sigma_i$  - local standard deviation around  $i$ th image,
- $t_i$  -  $3.1\sigma_i + \mu_i$ , detection threshold,
- $\epsilon_i$  -  $\sigma_i / \mu_i$ , local error around the  $i$ th image,
- $G_g$  - gain conversion factor for gain step  $g$ , in units of sensor output per photoevent,
- $\epsilon_{1/G}$  - error in  $1/G_g$ ,
- $\epsilon_N$  - average local error in the measured number,

$$\epsilon_N = \frac{1}{M} \sum_i \left( \frac{\sigma_i}{\mu_i} \right), \quad (16)$$

- $\epsilon_\mu$  - upper bound error in the measured number for the case of  $M$  averaged images,

$$\epsilon_\mu = \frac{\max(\epsilon_i)}{\sqrt{M}}, \text{ over all } i. \quad (17)$$

To prevent extreme values from affecting the local statistics, the maximum and minimum values within the  $N$  window samples were rejected. That is, only  $N-2$  images were used for the local mean and local standard deviation computation. Under the assumption that the mean radiant intensity

is high enough for the radiant intensity fluctuations to be modeled by a gaussian distribution, the probability of exceeding the threshold  $t_i$  is no more than 0.001.

Table 19 lists  $M$ , the number of images averaged, and  $\epsilon_N$ , the error caused by measurement in the values averaged over the window that consists of  $N$  images. There are three columns of  $\epsilon_N$  values corresponding to plume-camera central region measurements, plume camera central region plus outer region, and tracker camera 19 by 19 pixel field of view. The 19 by 19 tracker-camera pixels approximately cover the full field of view of the plume camera. The central region and outer region as used in this report are defined in Section 5.1.

Table 19 - Percent Error per Image Resulting from Measurement Noise,  $\epsilon_N$

Images ( $M$ )	Plume Camera Central Region	Plume Camera Central Region + Outer Region	Tracker Camera 19 x 19
96	34.3	20.0	6.28

#### 4.6.2 Error in Gain Conversion Factor

The gain conversion factor  $G_g$  derived from on-orbit calibration [1], is based on calibration star measurements. On the basis of measurements of several calibration stars over the full set of UVPI camera gains, an estimate of error associated with  $G_g$  can be obtained for each camera configuration by calculating the deviations of individual calibration star measurements about a mean calibration curve.

Table 20 tabulates the error associated with the gain conversion factor for the plume and tracker cameras. The average deviation is a good error estimate; the maximum deviation gives a worst-case estimate.

Table 20 - Error in  $1/G_g$  for Tracker and Plume Cameras

Camera/Filter	Average Deviation from Mean Calibration Curve (%)	Maximum Deviation from Mean Calibration Curve (%)
Tracker	15.6	17.3
Plume, PC-1	10.5	33.3
Plume, PC-2	15.9	25.2
Plume, PC-3	9.9	24.7
Plume, PC-4	13.5	26.0

#### 4.6.3 Calculation of Total Error

The estimated total calibration error depends on the number of images averaged together,  $M$ . In this report the total error is defined as the ratio of the standard deviations of the number of photoevents to the mean value of the number of photoevents. Assuming that the digital number reported by UVPI for a calibration star and the gain conversion factor  $G_g$  are uncorrelated, or weakly correlated, then the total error per image  $\epsilon_F$  can be obtained from the relation [15]:

$$\epsilon_F = \sqrt{\epsilon_N^2 \cdot \epsilon_{1/G}^2 + \epsilon_N^2 + \epsilon_{1/G}^2} \quad (18)$$

where  $\epsilon_N$  is the average local error in the number of measured photoevents presented in Table 19 and  $\epsilon_{1/G}$  is the error in the gain conversion factor tabulated in Table 20.

For the case of  $M$  averaged images, an upper bound estimate of the total error is given by

$$\epsilon_T = \sqrt{\epsilon_u^2 \cdot \epsilon_{1/G}^2 + \epsilon_u^2 + \epsilon_{1/G}^2}. \quad (19)$$

Notice that  $\epsilon_T$  can never be smaller than  $\epsilon_{1/G}$  no matter how many images are averaged together.

Table 21 summarizes the overall error analysis results for the plume central region radiant intensities. The first column contains the number of images within the data interval. The column under the  $K$  heading contains the ratio of the average standard deviation of photoevents to the square root of the average number of photoevents, i.e.,

$$K = \frac{1}{N} \sum_i \left( \frac{\sigma_i}{\sqrt{\mu_i}} \right). \quad (20)$$

Table 21 - Plume Central Region Radiometric Percent Errors for Plume Camera

$M$	$K$	$\epsilon_F$	$\epsilon_T$
96	1.35	36.1	11.5

Under the assumption that the signal is not changing rapidly in time,  $K$  relates the measured noise to the theoretical performance of a background-limited system, where the dominant source of noise is shot noise. A ratio of  $K = 1$  implies pure background-limited performance. Hence, the values obtained indicate that although UVPI is close to background-limited performance, other sources of sensor noise are present.

The third and fourth columns show, respectively, the total percent error on an image-by-image basis and the total percent error resulting after averaging all  $M$  images.

Similar to Table 21, Tables 22 and 23 show, respectively, the radiant intensity errors for the total plume camera field of view and those for the 19 by 19 tracker camera pixels that overlay the plume camera field of view.

Table 22 - Central Region Plus Outer Region Radiometric Percent Errors for Plume Camera

$M$	$K$	$\epsilon_F$	$\epsilon_T$
96	1.25	22.7	11.5

Table 23 - Radiometric Percent Errors: Tracker Camera Over 19 x 19 Pixel Window

$M$	$K^*$	$\epsilon_F^*$	$\epsilon_T^*$
40	2.96	16.8	15.8

\*Not redleak-corrected

Table 24 lists  $\epsilon_T$  for the plume camera observing the central region only, for the plume camera observing the central region and the outer region, and for the 19 by 19 pixel field in the tracker camera that corresponds to the full plume-camera field of view.

Table 24 - Total Radiometric Percent Errors,  $\epsilon_T$ 

Plume Camera Central Region	Plume Camera Central Region + Outer Region	Tracker Camera 19 x 19*
11.5	11.5	15.8

\*Not redleak-corrected

#### 4.7 Noise-Equivalent Radiance

Following the noise-equivalent radiance (NER) definition given in the Infrared Handbook [16], the UVPI NER is defined as the source radiance level that will result in a signal-to-noise ratio of 1 at the output of a single pixel. The NER can be interpreted as the sensitivity limit for an imaging system. For UVPI, a single NER number does not fully characterize the sensitivity of the system since this is a function of integration time, spectral filter, camera gain level, number of images superposed, and the assumed source spectrum.

The following discussion is based on empirical estimates of the signal and noise within the UVPI cameras as opposed to a theoretical discussion. Reference 17 provides a theoretical expression for the signal-power to noise-power ratio applicable to the microchannel plate image intensifier of the UVPI. A single pixel in the plume or tracker camera can be treated as a photoevent counting device. The signal-to-noise ratio (SNR) definition from which the empirical UVPI NER is derived is

$$(\text{SNR})^2 = M^2 \cdot S^2 / (M \cdot N^2 + M \cdot N_S^2), \quad (21)$$

where

- $M$  is the number of images superposed. This affects the effective integration time.
- $S$  is the mean number of signal-related photoevents collected in a pixel during the integration time.
- $N$  is the signal-independent noise standard deviation for a single pixel in a single image expressed in photoevents/pixel-image. This noise source is constant. When expressed in photoevents/pixel-image, its level depends on the camera gain setting used.
- $N_S$  is the signal-dependent photon shot noise standard deviation in a pixel during the integration time expressed in photoevents/pixel-image. Based on extensive measurements made on UVPI data, the signal-dependent noise can be expressed in terms of the mean number of signal related photoevents by using the equation:

$$N_S = 2S^{1/2}. \quad (22)$$

Note that this is two times higher than the photon shot noise prediction.

From Eq. (21) above, the mean number of signal-related photoevents/pixel-image in a pixel that will result in a SNR of 1 is

$$S' = 2 [1 + (1 + M \cdot N^2/4)^{1/2}] / M. \quad (23)$$

Notice that for the case of only one superposed image,  $M=1$ , and a negligible level of sensor noise  $N$ , the resulting sensitivity limit is 4 photoevents/pixel-image. The NER is related to  $S'$  by a multiplicative constant  $K$ , i.e.,

$$\text{NER} = K \cdot S' = 2K [1 + (1 + M \cdot N^2/4)^{1/2}] / M, \quad (24)$$

where  $K$  is the radiometric calibration constant that converts from photoevents/pixel-image to  $\mu\text{W}/\text{sr}\cdot\text{cm}^2$ .  $K$  is a function of the spectral filter used, the single image exposure time, and the assumed source spectrum.

The radiometric sensitivity could also be improved by performing spatial averaging at the expense of a lower spatial resolution.

Table 25 summarizes the estimated NER, or sensitivity level, for the plume camera under the assumption of the reference spectrum. Since, for the plume camera, the signal-independent noise is negligible compared to the signal-dependent noise, image superposition provides an increase in sensitivity that is linear with the number of superposed images.

Table 25 - Plume Camera NER Per Pixel for Data Interval

Filter	NER for Single Image (W/sr-cm <sup>2</sup> )	Number of Images Superposed	NER for Data Interval (W/sr-cm <sup>2</sup> )
PC-1	$1.24 \times 10^{-5}$	96	$1.30 \times 10^{-7}$

Table 26 summarizes the estimated NER, or sensitivity level, for the tracker camera under the assumption of the reference spectrum. The last column expresses the sensitivity level in photoevents/s. As opposed to the plume camera, the tracker camera signal-independent noise is not negligible, and the improvement in sensitivity is not linear with the number of images superposed.

Table 26 - Tracker Camera NER Per Pixel

NER for Single Image (W/sr-cm <sup>2</sup> )*	Number of Images Superposed	NER for Data Interval (W/sr-cm <sup>2</sup> )*	Minimum Detectable Number of Photoevents/s for Superposed Images*
$9.10 \times 10^{-8}$	40	$8.06 \times 10^{-10}$	48.6

\*Not redleak-corrected

## 5.0 SPATIAL FEATURES

This section concentrates on the spatial characterization of the measured plumes. First, definitions for the plume central region and outer region are presented. Second, the plume's spatial extent is discussed with consideration for the UVPI's point spread function (PSF). Finally, the observed plume is compared to CHARM 1.3 model predictions.

### 5.1 Delineation of Plume Central and Outer Regions

Because of the generally low signal statistics in a single image, an accurate delineation of the plume central or outer region is not possible from a single image. Hence, an average of superposed images (a composite image) is used to define the plume central region extent.

Definition of the central region was begun by selecting all pixels in the composite image for which the radiance was at least 25% of the brightest pixel radiance. The resulting region was expanded further by performing a dilation with a square window of 5 by 5 pixels. By using this criterion, the region defining the plume central region is depicted in Fig. 44. The image on the left is the composite image; in the image on the right, the corresponding central region is overlaid as a completely white region.

Table 27 summarizes the central region extent in pixels for the data interval.

Table 27 - Central Region Extent in Plume Camera

Filter	Central Region Extent (pixels)	Central Region Extent (m <sup>2</sup> )
PC-1	304	7563

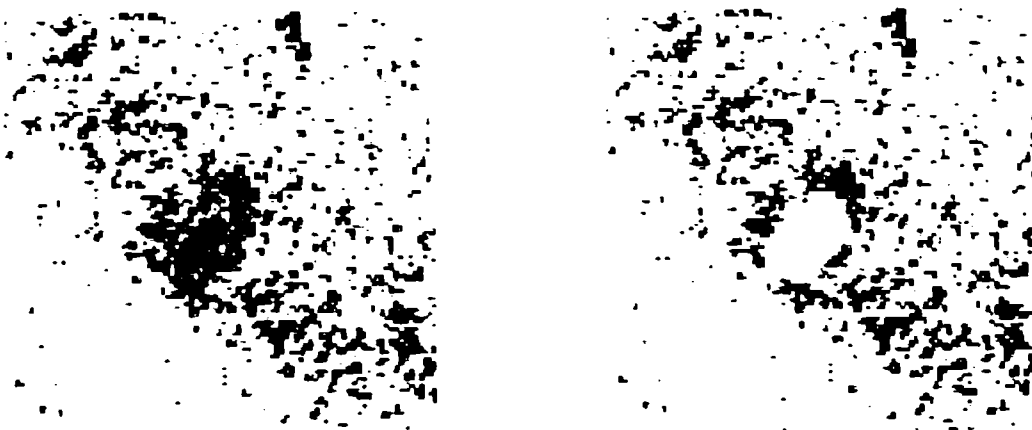


Fig. 44 - Highlighted plume central region for Nihka

For the tracker camera, the central region was defined as all those pixels that overlap the plume camera field of view. Hence, in this report, the central region for the tracker camera is not defined over the same area as for the plume camera.

From the point of view of phenomenology, an argument can be made that the central region definition above does not fully contain the plume core. To validate the definition of the plume central region, additional consecutive dilation operations were performed to force the defined central region to become larger. As an example, Fig. 45 shows the number of photoevents per image in the central and outer regions as a function of central region size. A vertical dashed line illustrates the central region size used in this report. This plot can be used to scale the results presented in this report if a different central region size is desired.

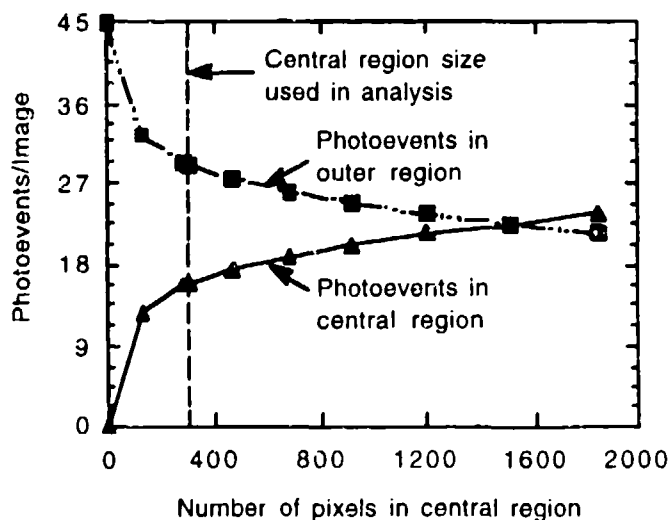


Fig. 45 - Photoevents as a function of defined central region size

## 5.2 Plume Extent and Point Spread Function

The effective UVPI point spread function (PSF) is defined as the response of the instrument to a point source, e.g., a star or a ground-based beacon. An understanding of the UVPI plume camera's PSF is critical in establishing the maximum size of the observed Nihka plume. Table 28 summarizes the estimated plume central region axial length, as defined from peak to either 50% or 10% of peak brightness. These plume length estimates do not incorporate corrections for the aspect angle or for the plume camera's PSF.

Table 28 - Observed Axial Length of Plume Central Region

Filter	Peak to 50% Maximum (m)	Peak to 10% Maximum (m)
PC-1	40.4	86.5

Based on UVPI data from many observations, the plume camera's PSF depends on the observation modality, i.e., downward-looking vs sideward-looking. Sideward-looking observations use the door-mounted mirror but downward-looking observations do not. The observation of the Nihka plume did not use the door-mounted mirror. The existing data for point sources indicate that the PSF is less circularly symmetric when using the door-mounted mirror. This could be the result of jitter in the door mirror.

Figure 46 shows a plume-camera image of a ground-based beacon. Reference 1 gives a scaled version of the plume camera's PSF for the beacon. Figure 46 shows a three-dimensional plot of the PSF that results from observation of the ground-based beacon. For the ground-based beacon, the axial length of the PSF from peak to 50% of the peak along the major axis is about 4 pixels or 20 m at a range of 450 km, as shown in Fig. 47. The full-width-half-maximum length is about 40 m.

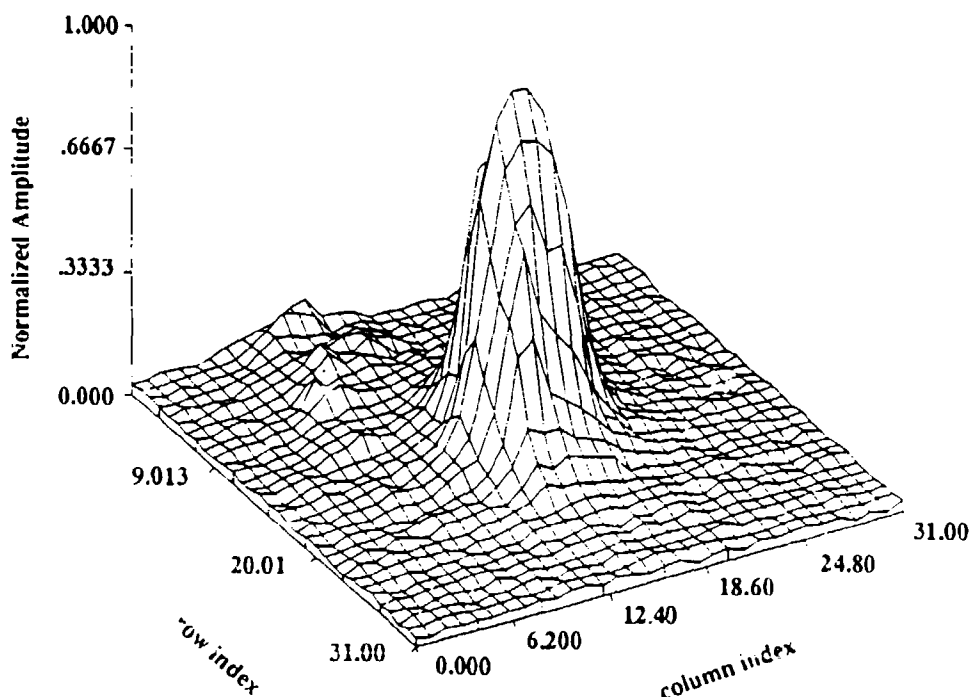


Fig. 46 - Plume camera PSF for ground-based beacon

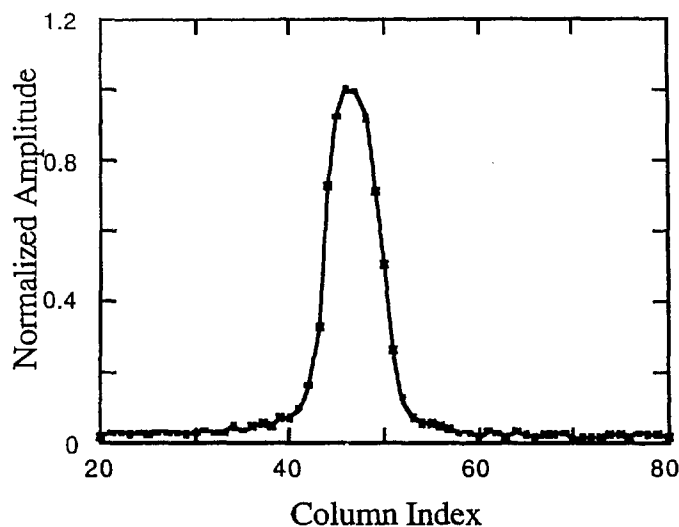


Fig. 47 - Axial profile through plume camera PSF for ground-based beacon

Figure 48 is a profile of the radiance along the major axis of the plume, measured by the plume camera. The horizontal line corresponds to the NER sensitivity limit after image superposition. It is evident from this figure that, after image superposition, good SNR was achieved.

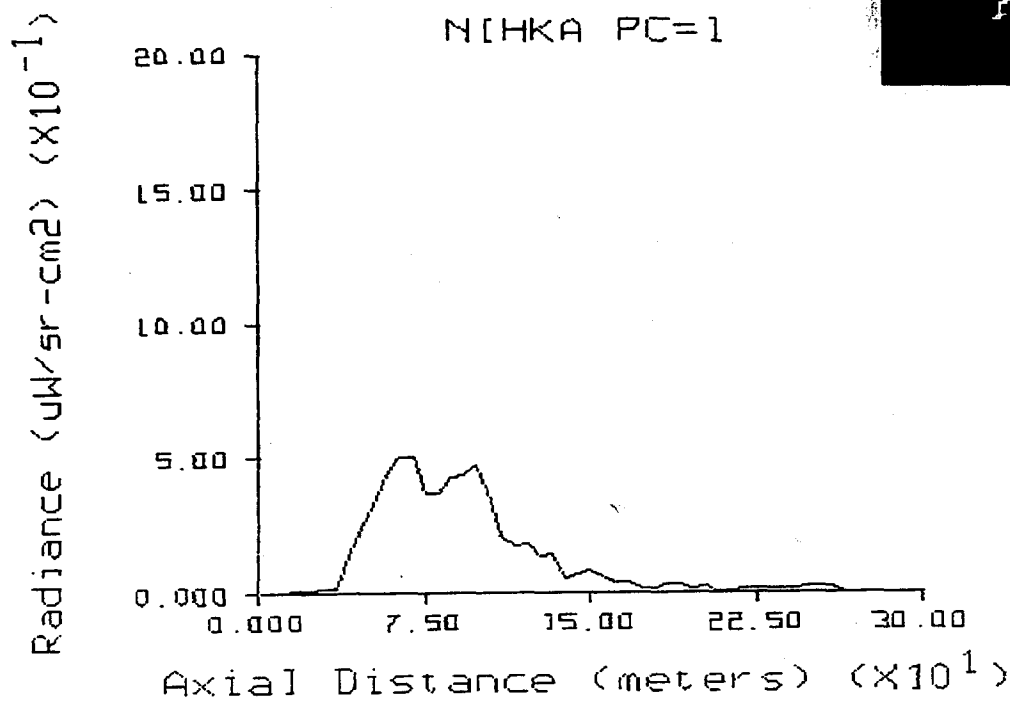


Fig. 48 - Axial profile along plume central region, plume camera

Figure 42 is a tracker camera image of a ground-based beacon. Reference 1 gives a scaled version of the tracker camera's PSF for the beacon. Figure 49 shows a three-dimensional plot of the PSF that results from observation of the ground-based beacon, and Fig. 50 is an axial profile of the beacon as seen by the tracker camera.

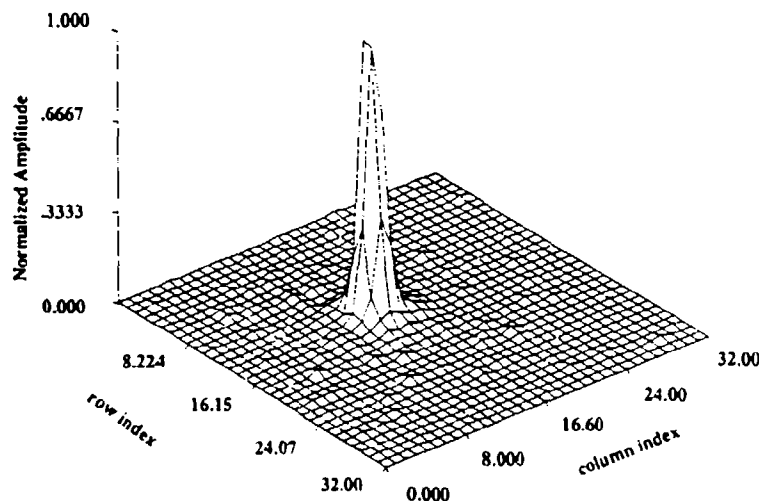


Fig. 49 - Tracker camera PSF for ground-based beacon

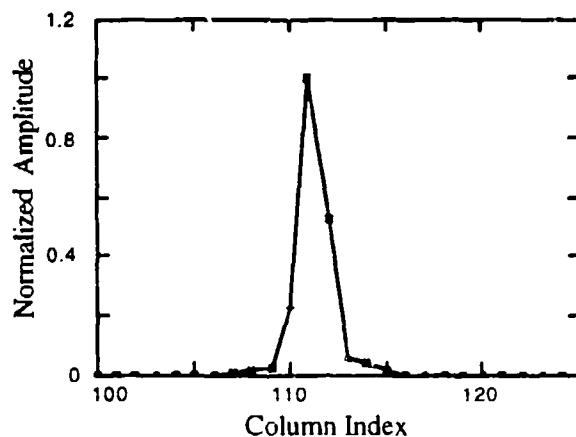


Fig. 50 - Axial profile through tracker camera PSF for ground-based beacon

### 5.3 Comparison of Results to CHARM 1.3 Predictions

This subsection compares the UVPI measurements to the predictions provided by a theoretical plume model. Research Support Instruments (RSI) (Alexandria, Virginia) generated a CHARM 1.3 run in which the Nihka stage was modeled and emission in the PC-1 waveband was summed, by using input parameters provided by Grumman Corp. [18]. The CHARM 1.3 input deck is included as Appendix C. The following basic parameters were used for the run:

Model:	CHARM 1.3
Object modeled:	Intrinsic Core
Aspect angle for data interval:	56°
Horizontal resolution:	5.0 m
Vertical resolution:	5.0 m

In RSI's run, a 5 by 5 m pixel resolution was used. To get a comparison between the CHARM 1.3 predictions and the UVPI measurement, the CHARM 1.3 predictions were convolved with an estimate of the UVPI's PSF. A normalized version of the ground-beacon image, Frame 12778, Orbit 1173, was used as the best UVPI plume-camera PSF estimate.

Figures 51 and 52 show an example of the CHARM 1.3 prediction convolved with the UVPI point spread function (PSF). The left image in Fig. 51 shows a false-color CHARM 1.3 image prediction with 5-m resolution for the Nihka motor, assuming it is being observed with PC-1. The right image shows the same CHARM 1.3 prediction, except that it is convolved with the UVPI point spread function. Figure 52 is the corresponding contour plot for the image prediction, again assuming UVPI PC-1 and convolution with UVPI PSF. For the Nihka data interval, Fig. 53 shows: the CHARM 1.3 high-resolution prediction of the plume radiance as a function of axial distance; the CHARM 1.3 prediction convolved with the UVPI plume camera PSF; and a horizontal line depicting the interval noise-equivalent radiance (NER) of the plume camera.

The peak radiances and the plume lengths for the CHARM 1.3 image predictions are listed in Tables 29 and 30.

**CHARM1.3 Prediction  
Using 5 Meter Resolution**

**CHARM 1.3 Prediction  
Using UVPI's PSF**



**max=4.48 uW/sr-cm2**

**| =0.095\*max | =0.50\*max | =0.95\*max**

Fig 51 - CHARM 1.3 image prediction for PC-1 before and after smearing

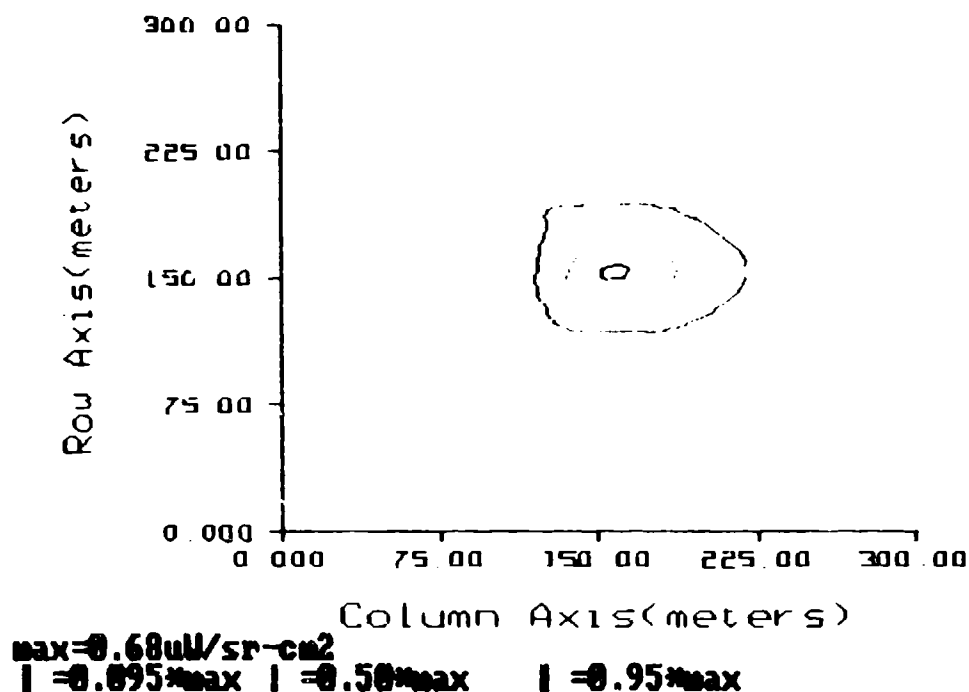


Fig. 52 - CHARM 1.3 contour plot prediction for PC-1 after smearing

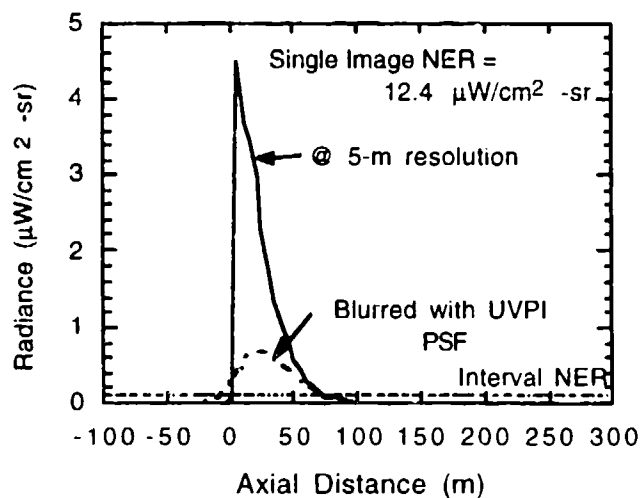


Fig. 53 - CHARM 1.3 predicted axial profile before and after smearing

Table 29 - Peak Radiance Comparison

Filter	CHARM 1.3 @ 5-m Resolution Peak Radiance ( $\mu\text{W}/\text{sr}\cdot\text{cm}^2$ )	CHARM 1.3 Convolved Peak Radiance ( $\mu\text{W}/\text{sr}\cdot\text{cm}^2$ )	UVPI Measured Peak Radiance ( $\mu\text{W}/\text{sr}\cdot\text{cm}^2$ )
PC-1	4.48	$6.82 \times 10^{-1}$	$5.47 \times 10^{-1}$

Table 30 - Comparison of Measured to Predicted Plume Length

Filter	Plume Length (m) Peak to 50% and Peak to 10%					
	CHARM 1.3 @ 5-m Resolution		CHARM 1.3 Using UVPI's PSF		UVPI Measured	
	50%	10%	50%	10%	50%	10%
PC-1	25	50	50	80	40.4	86.5

## 6.0 TEMPORAL FEATURES

This section presents calibrated photoevents per image and radiant intensity values for the Nihka data interval. The calibration procedure used is described in Section 3. The conversion to radiant intensity is performed by using a reference emission spectrum for incandescent alumina particles that is typical of the emission spectrum produced by solid-fuel rocket motors containing ammonium perchlorate/aluminum. The latter is similar to the model used in the CHARM 1.2 code and its later versions CHARM 1.3 and 1.4. Section 6.1 presents the plume-camera observations and 6.2 presents the tracker camera observations.

### 6.1 Plume Camera Intensity Plots

This section presents the number of photoevents observed in the plume camera, both central region and total, for each image during the data interval.

The separation of plume central region from total FOV is described in Section 5.1. During the telemetry frame range depicted in each plot, the plume-to-tracker image ratio was 8:2. Consequently, the plots show repeated groups consisting of eight consecutive plume camera images followed by a gap where the two tracker camera images occurred.

In addition to the intensities, the figures include: the estimated local mean, which is a running average of the intensity; and a threshold of 3.1 standard deviations above the local mean, which flags intensity values that are highly unlikely (probability less than 0.001) based on local statistics. The local statistics are computed by using a running window of 15 frames for plume camera data. Section 4.6 gives a more complete discussion of the computations of local statistics.

Figures 54 and 55 convey information useful for indexing those frames or times at which a significant statistical deviation in the intensity is observed, based on the local statistics, and for showing the intensity variation over both the plume central region and the total plume.

Figure 54 shows two instances in which the measured number of photoevents exceeds the local mean by more than 3.1 standard deviations. The probability of such an event is less than 0.001. Therefore, all instances in which the measured number of photoevents exceeded the threshold were investigated in great detail. No significant difference was observed in the composite images after disregarding the images where the measured number of photoevents exceeded the threshold. As can be seen from Figs. 54 and 55, the number of photoevents for the total plume-camera field of view

increases with time whereas the number of photoevents for the central region is fairly constant. This was seen in the plots of spectral radiant intensity depicted in Figs. 31 and 32.

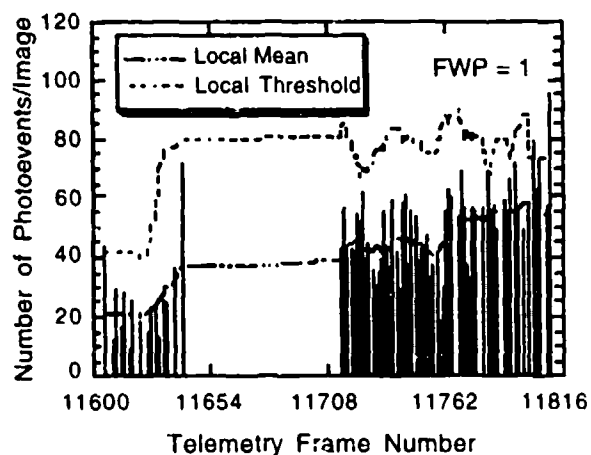


Fig. 54 - Nihka, plume camera, total field-of-view intensity

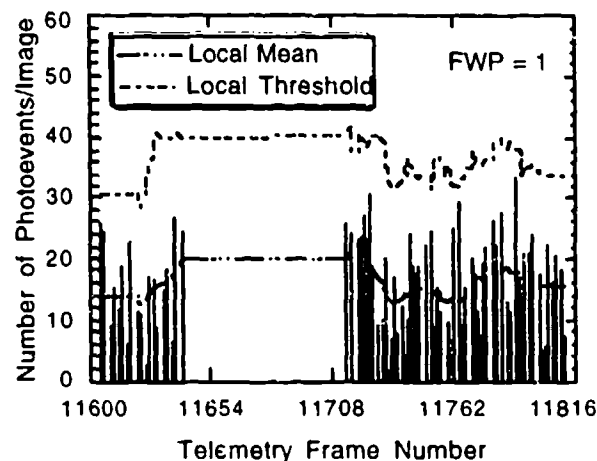


Fig. 55 - Nihka, plume camera, central region intensity

Table 31 summarizes the average radiant intensity (ARI) and average spectral radiant intensity (ASRI) for the plume-camera observation. The average radiant intensity reported is based on the reference spectral energy distribution assumption. It represents the average of all images in the interval.

Table 31 - Summary of Plume Camera Average Radiant Intensity

Band (nm)	Measured ARI*	Measured ASRI**		
	Central Region ARI (W/sr)	Total ARI (W/sr)	Centroid Wavelength (nm)	Total ASRI (W/sr-μm)
220-320	12.3	34.6	280	231.0

\* Average Radiant Intensity

\*\* Average Spectral Radiant Intensity

When operating in the zoom image transmission rate, each telemetry frame contains one image.

## 6.2 Tracker Camera Intensity Plots

Figure 56 presents total photoevents per image for the 19 by 19 pixel section of the tracker camera, corresponding approximately to the total field of view of the plume camera. This field of view contains plume central region and a portion of the outer region. Figure 56 is primarily intended to show image-to-image variations in the number of photoevents per image after redleak correction. To provide an estimate of the average radiant intensity, values based on reference spectral energy distribution assumptions are reported in Table 32 for the tracker-camera observation. These results have been reduced by 16.3% to account for red leakage in the tracker-camera filter. As can be seen in Fig. 56, a slight ramp up in photoevents occurs during the burn. However, this is not as strong as is seen in the total plume camera field of view in Fig. 54.

In addition to the intensities, the figure includes: the estimated local mean, which is a running average of the intensity; and a threshold of 3.1 standard deviations above the local mean, which flags

intensity values that are highly unlikely (probability less than 0.001) based on the local statistics. The local statistics are computed by using a running window of 15 frames for tracker camera data. Section 4.6 provides a more complete discussion of the computations of local statistics.

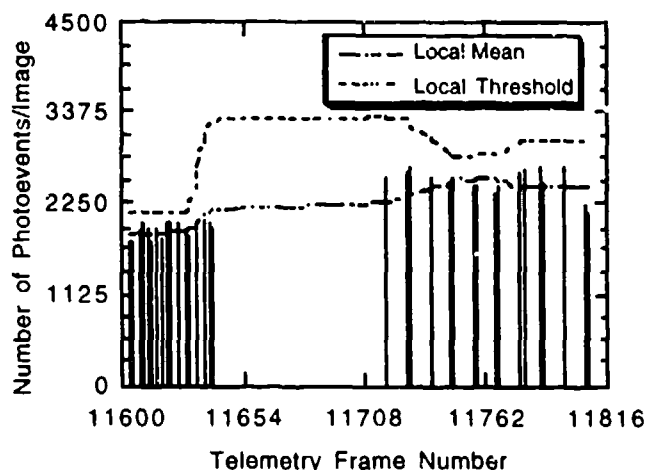


Fig. 56 - Nihka, tracker camera

Table 32 - Summary of Tracker Camera Average Radiant Intensity

Filter	Band (nm)	ARI* in 19 x 19 Pixel Region (W/sr)	ASRI** in 19 x 19 Pixel Region @ 390 nm (W/sr-μm)
PC-1	255 - 450	$1.72 \times 10^2$	$1.37 \times 10^3$

\* Average Radiant Intensity

\*\* Average Spectral Radiant Intensity

## 7.0 SPECTRAL ANALYSIS OF PLUMES

This section presents the spectral analysis of the emission from the Nihka stage plume. As summarized in Table 15, the UVPI plume and tracker cameras observed the Nihka stage at a range of approximately 451 km. The figures and tables in this section show: the computed spectral radiant intensity in W/sr-μm of the plume central region, and the spectral radiant intensity measured over the entire plume camera field of view.

### 7.1 Observed Spectral Radiant Intensities

The conversion of the plume and tracker camera data to radiometric values requires the assumption of a source spectrum, as described in Section 3.5. The reference spectral shape has been used in the analysis of the camera data presented in this section. The wavelength for which the spectral radiant intensity is reported is the centroid wavelength when the assumed source spectrum is convolved with the UVPI net quantum efficiency function, as described in Section 3.6.

In selecting the reference spectrum scaling factor, an effort was made to find a good arbitrary fit to the PC-1 and tracker-camera data points.

The plume-camera observation of the Nihka was made between 185.0 and 191.9 s after liftoff. The range from UVPI to the rocket was approximately 450 km during this time period. The spectral radiant intensity of the plume central region, as measured by UVPI using the PC-1 spectral filter and the tracker camera, is listed in Table 33.

Table 33 - Measured Spectral Radiant Intensity

Wavelength (nm)	Filter	Observed Central Region (W/sr- $\mu$ m)	Plume Camera Field of View (W/sr- $\mu$ m)
280	PC-1	82.1	231.0
390	Tracker	-	1370

The spectral radiant intensity for the Nihka stage, measured by UVPI over the entire plume camera field of view, is shown in Fig. 57. Note that the tracker-camera pixels analyzed in this section corresponded to the full field of view of the plume camera. Figure 57 also shows a scaled reference spectral shape and blackbody spectrum. The data are also listed in Table 33. The scaling of the reference spectrum, relative to the plume and tracker camera measurements, is arbitrary and is intended to give a measure of relative spectral radiant intensities compared to that predicted by the reference spectrum.

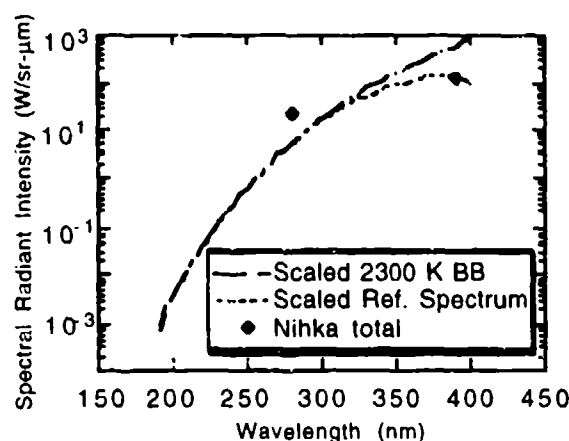


Fig. 57 - Measured spectral radiant intensity for the Nihka, plume camera field of view

## 7.2 Discussion

The reference model hypothesizes that the principal source of UV radiation is thermal emission from alumina particles at the fusion temperature of alumina, 2320 K. The spectral shape departs from that of a blackbody because of the decreasing effective emissivity of the particles with increasing wavelength. The plume camera data in the far UV are significantly higher than would be expected based on a reference spectrum scaled to match the tracker-camera signal. No obvious modification to the reference spectrum will yield the far UV excess evident in the UVPI data. A plausible hypothesis is that an additional emission mechanism is producing the excess UV emission. Spectral line emission by exhaust gases and by the mesospheric atmosphere disturbed by the rocket, e.g., CO Cameron and NO gamma bands, are possible sources. The possibility of a far-UV excess caused by luminous gases was discussed briefly in the Orbus preflight document [7].

## 8.0 ANOMALOUS EVENTS

### 8.1 Possible Earlier Explosion

At about 152 s after the launch of the Black Brant X and about 24 s before the Nihka ignition, the UVPI tracker camera recorded a large flash in the lower central portion of the field of view. From the intensity contours and circular symmetry of this image, it appears that the central portion of this flash may not be contained in the tracker camera's field of view, but is below the field of view. The plume-to-tracker camera frame interleaving ratio was 2:8 during this portion of the observation and the previous frame was a plume-camera frame that shows no unusual activity. The

following seven frames are tracker-camera frames with the first two of the seven showing no unusual activity. The third of the seven shows an image in the form of a short streak aligned with the central region of the previous flash. The next frame shows what appears to be the beginning of a similar streak at the upper edge of the field of view and extending outside the field of view. Figure 58 is a composite of the three frames showing the flash and the two streaks.

The MCP was on for the entire duration of the image integration, which was  $1/30$ th of a second. The length of the streak is measured to be  $2 \pm 0.3$  microradians, and the distance from the beginning of the first streak to the beginning of the second streak is  $11 \pm 0.3$  microradians. The time between two frames is 0.2 s. Assuming that the streaks are both caused by a luminous object moving with respect to the field of view, the length of the streak and the distance between the two streaks are both consistent with a speed of about 55 microradians/s. Using this velocity and measuring the direction in a straight line connecting the end points of the two streaks places the object within the flash seen two frames earlier.

## 8.2 Nihka Burnout Anomaly

Near the end of the Nihka burn a bright object appeared on one plume-camera frame, 11810. Figure 59 is a composite of frame 11810 and several previous frames showing the Nihka plume and the bright object. This object is brighter than and quite distant from the rocket plume. The immediately previous and subsequent frames were both from the plume camera, and neither frame, nor any other, showed a similar object. The tracker electronics had solid lock throughout the Nihka burn until the time of burnout, about six frames later.

The assumption that this object is incandescent material ejected from the rocket nozzle cannot be convincingly supported from the observed data. The time between successive frames is  $1/30$ th second, the range from the UVPI to the Nihka at burnout is about 448 km, and the aspect angle is about  $56^\circ$ . The distance from the center of the rocket plume to the center of the bright object is about 576 microradians as measured in the plume camera image. From this, the speed of the material can be estimated as:

$$V = 448 \text{ km} * 576 \text{ } \mu\text{rad} (\sin(56^\circ) * 1/30 \text{ s})$$

and is 9.3 km/s. Since the integration time of a plume camera image is  $1/30$ th second, the length of the bright object in this image because of its speed would be more than 500  $\mu\text{rad}$ , but the measured length is only about 100  $\mu\text{rad}$ . This could be explained only if the time of burning of the incandescent material is about  $(1/30 \text{ s}) * (1/5) = 1/150 \text{ s}$ . The orientation of the longitudinal axis of the rocket plume as measured in the UVPI plume camera is  $-44^\circ$  from the horizontal of the camera image. The bright object is about  $-33^\circ$  from the horizontal, which is not in line with the observed thrust direction of the Nihka plume.

Since this object was quite bright and appeared quite distant from the rocket plume, tracker electronics data related to the target size and centroid error were examined to determine if it would correlate with such an object. Figures 60 and 61 show plots of target size and centroid error during the time of stable Nihka tracking. The target size shows an increase predominantly in the  $x$  direction and the centroid error is growing in the  $x$  direction at the same time. Although both curves show some increase beginning about 2 s before Nihka burnout, neither shows any unusual behavior during the last few frames of valid tracking when the bright object appears in the plume camera.

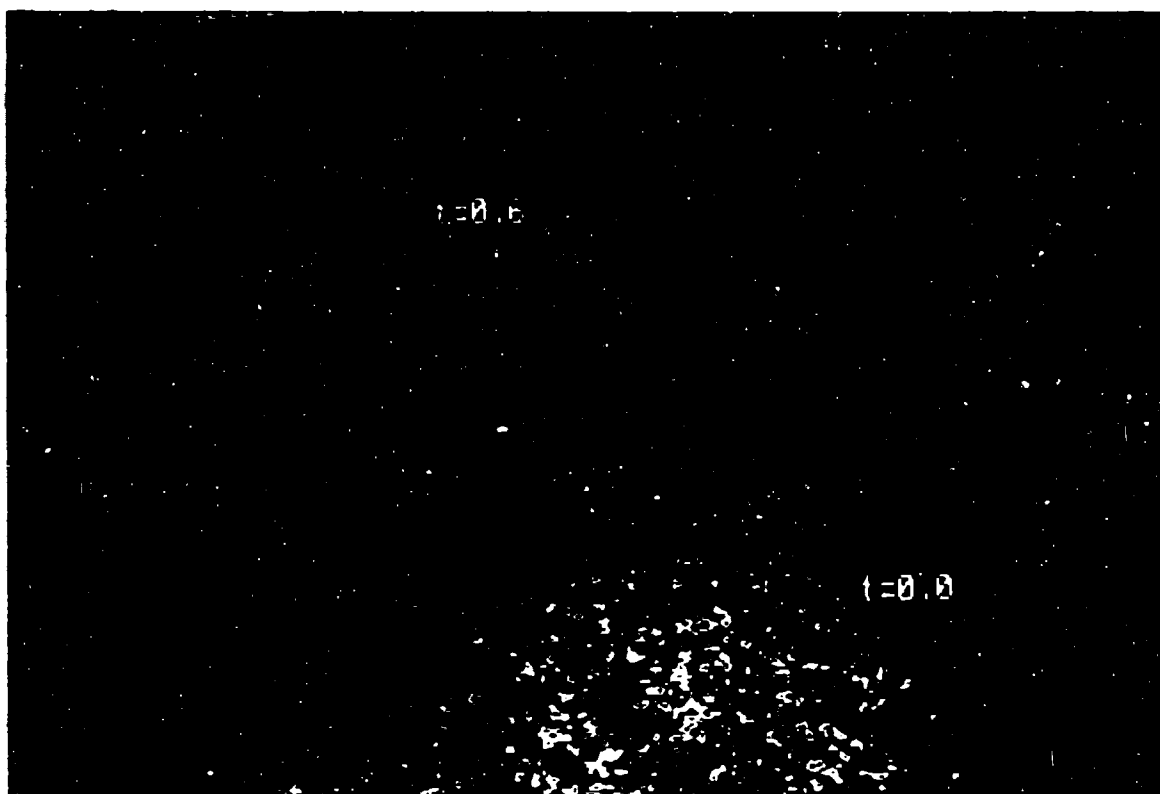


Fig. 58 - Composite tracker camera image showing flash and two streaks

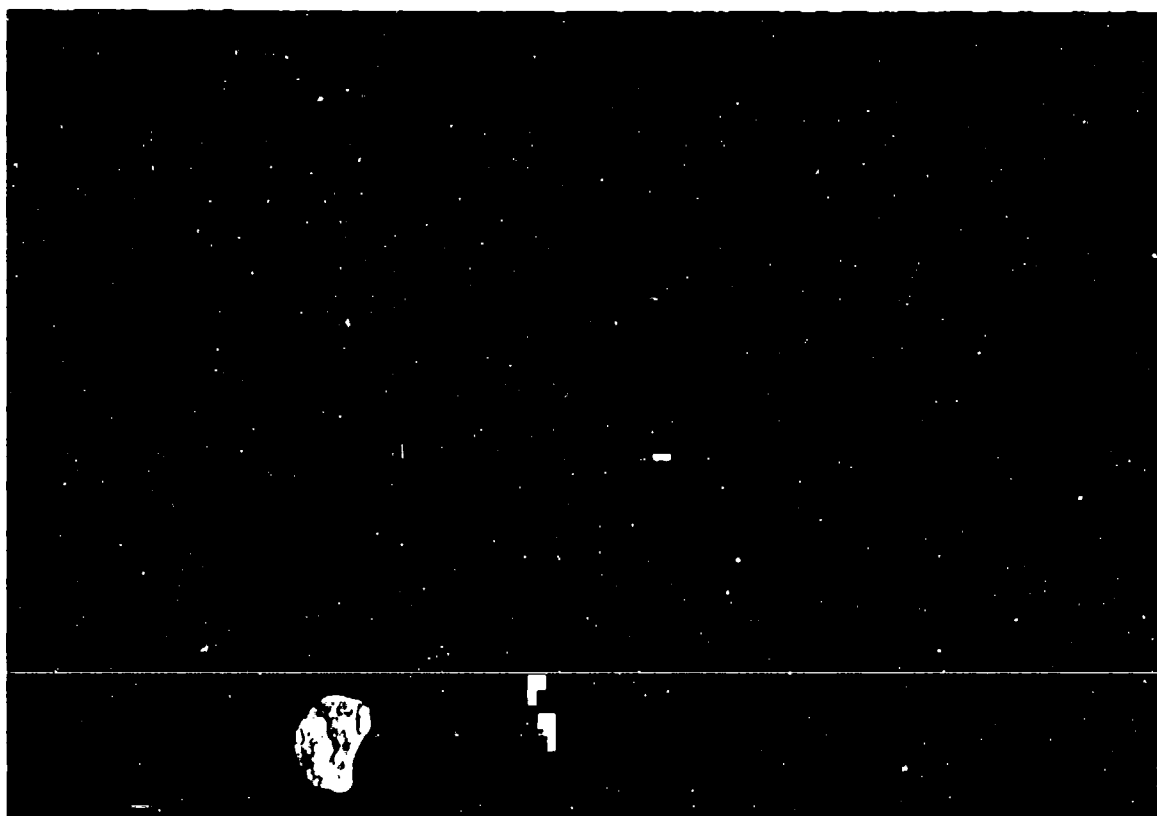


Fig. 59 - Composite plume camera image showing anomalous bright object and Nihka plume

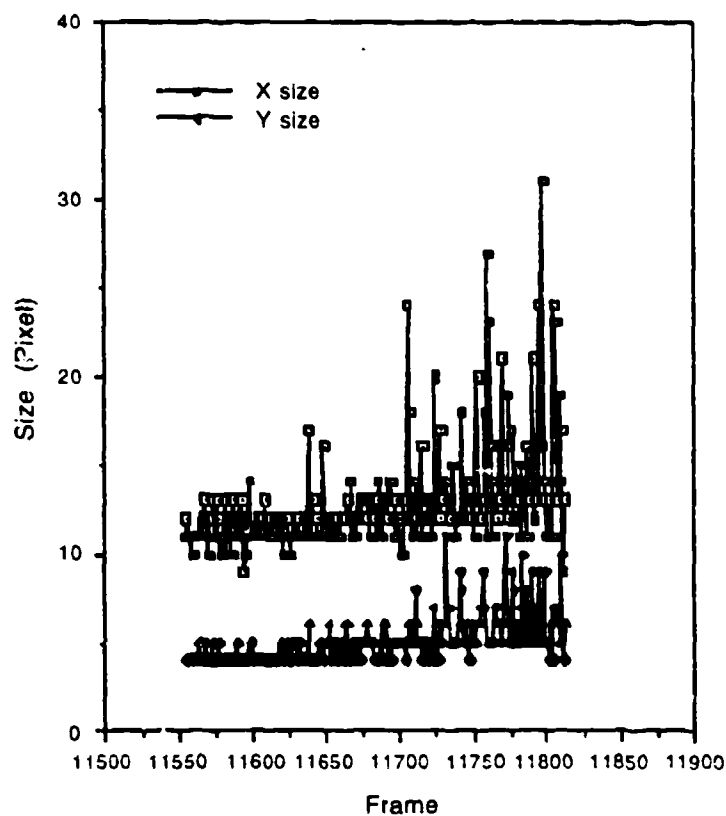


Fig. 60 - Target size during stable tracking of Nihka plume

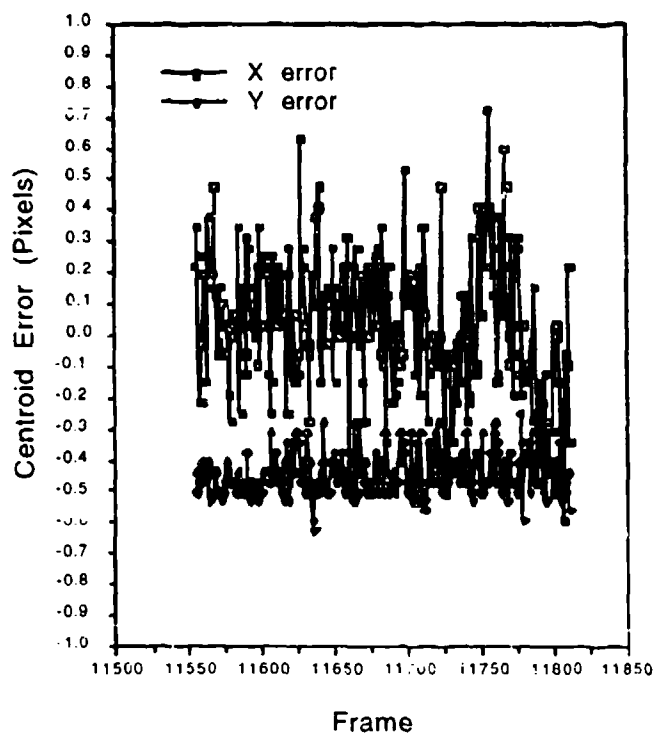


Fig. 61 - Centroid error during stable tracking of Nihka plume

## 9.0 SUMMARY AND CONCLUSIONS

### 9.1 Summary

The goal of the Nihka mission was the acquisition from space of radiometric UV plume data by using the UVPI onboard the LACE satellite. The UVPI plume camera is an imaging radiometer with four filters, centered at 250, 270, 280, and 305 nm. This instrument was designed to obtain radiometric data in a spectral region that is especially favorable for missile detection because of the very low solar background. Operation from space is necessary because the atmosphere is practically opaque to wavelengths below 300 nm. From 500-km range, the plume camera has a resolution of approximately 45 m.

The Black Brant X, a three-stage solid-propellant missile system, was obtained for this observation. The first stage (a Terrier motor) and the second stage (a Black Brant motor) operated at too low an altitude to be observed from space. The mission was designed for the observation of the third-stage plume produced by the Nihka rocket motor. The rocket trajectory was selected to permit observation from the LACE satellite during its pass near the Wallops Island launch site.

The Black Brant X was launched from Wallops Island, Virginia, before sunrise on 25 August 1990. The Nihka stage was successfully tracked by the UVPI camera from an average range of 451 km. The Nihka plume was tracked for 3.23 s, and plume data were acquired with one plume camera filter, PC-1, which spans the 220 to 320 nm band.

The 96 images of the Nihka plume from the plume camera were of sufficient quality and tracking accuracy to permit the superposition of images for increased radiometric accuracy.

The superposed images were analyzed to obtain the spectral radiance (evaluating the plume as a spatially resolved source) and the spectral radiant intensity (summing over space to treat the plume as a point source). The radiometric analysis requires a model spectral shape for which a reference spectrum of fusing aluminum particles was taken. The analysis procedure is described in Section 3. The spectral values were also integrated over the nominal filter bandwidth to obtain radiance and radiant intensity values.

Figure 38 is a false-color map of the spatial distribution of the time-averaged radiant intensities of the Nihka plume from the plume camera. A contour plot of the plume radiance was also generated from the superposed images and is presented in Fig. 39.

Figure 36 shows the plume camera image, and Fig. 37 shows the associated contour plot of the NRL ground-based UV beacon, which well represents a point source under these conditions. This image indicates the resolution limit of the instrument at 500-km range. The length of the rocket plume observed during this mission is less than or comparable to the 45-m resolution limit (Table 28), and the consequent smearing of the source over an increased effective area reduces the observed peak radiance of the plume. The observed radiance is denoted "apparent" to distinguish between the observed radiance values and these which would be obtained from an instrument with higher spatial resolution. An adjustment of the CHARM predicted peak radiance for this effect yields reasonable agreement between prediction and observation (Table 29).

Radiant intensity values, obtained by summing over the plume central region and over the plume-camera field of view, are not affected by this resolution effect. The plume central region was defined for these computations as the region in which the radiance exceeded 25% of the peak apparent value, with the addition of the area defined by a 5 by 5 pixel dilation of this region. The projected area of the central region so defined was approximately 7500 m<sup>2</sup> (Table 27). The remainder of the plume-camera image is denoted the outer region.

The outer region data from the Nihka showed strong far-UV radiance that increased in time. Like the Strypi data at lower altitude [2], an identifiable shock or mixing layer structure could be found in the Nihka outer region data and, thus, the outer region radiance can be causally connected to the Nihka plume central region and total radiant intensities measured by the plume camera are summarized in Table 31. The temporal behavior of the plume central region and total spectral radiant intensity measured by the plume camera are shown in Figs. 31 and 32. The plume camera saw a total field of view signal that increased strongly in time whereas, the plume central region signal did not change very much. This indicates that a UV luminous outer region existed around the plume and grew brighter with time.

The UVPI tracker camera provides wideband (255 to 450 nm) data that may complement the plume camera data. The wide field of view of the tracker camera clearly prevents resolution of the plume, but radiant intensity values can be obtained. A 19 by 19 pixel region of the tracker camera images, matching the total field of view of the plume camera, was taken for computation of radiant intensities. The values so obtained are summarized in Table 32, and the spectral radiant intensity time dependence is illustrated in Fig. 33.

The tracker camera saw only a weak increase over time for the total plume radiance. This suggests that the increasing luminosity seen in the plume camera total field of view was concentrated in the far to mid-UV rather than being a broadband spectrum such as the reference spectrum. If the luminosity at longer wavelengths detected by the tracker camera had grown by the same degree as the luminosity seen by the plume camera at shorter wavelengths, then the plume and tracker camera spectral radiant intensity profiles, shown in Figs. 32 and 33 respectively, would have shown the same percentage increase. Since they do not, it appears the growing luminosity was concentrated in the mid and far UV.

The spectral radiant intensities deduced from the UVPI observations can be compared to the reference model of plume emission by comparing the predicted ratio of PC-1 to tracker-camera measured emissions. The plume spectral radiant intensities, summed over the plume camera field of view, are roughly consistent with the reference spectrum prediction. However, the 220 to 320-nm values are higher, relative to the 255 to 450-nm values, than the reference spectrum predicts (Fig. 57). The spectral radiant intensities summed over the plume camera field of view appear to show an ultraviolet excess that grew with time. The data supports the tentative conclusion that the decrease in plume spectral radiant intensity as the wavelength decreases below 300 nm is less than expected on the basis of the reference model. This is similar to trends seen in the Strypi plume data [2].

The Nihka vehicle rose to higher altitudes than other vehicles. This allowed much greater expansion of exhaust gases into the plume outer region and also caused the Nihka to encounter areas where atomic oxygen was a major component of the atmosphere. Taken with the Strypi [2] and Starbird [19] data, the increasing UV luminosity of the Nihka plume outer region suggests that high-altitude rocket plumes may owe some of their UV luminosity to reactions of plume constituents with atomic oxygen, UV gases in the plume itself, or both.

## 9.2 Achievement of Objectives

The results of the UVPI observation of the Nihka missile can be compared to the objectives listed in Section 1.3.

### 9.2.1 General Objectives

- *Obtain isoradiance contours for the Nihka stage.* Spatially resolved images of the Nihka stage plume were obtained by using the PC-1 plume-camera filter. These images were scaled to radiance maps and contours, as illustrated in Sections 4 and 5.
- *Obtain radiant intensity measurements based on the entire field of view of the plume camera and on a subregion corresponding approximately to a plume core.* Radiant intensity measurements for the plume camera FOV and for a plume central region defined in Section 5.1 were extracted from the images. These results are presented in Section 6.
- *Compare radiometric measurements for the Nihka-stage plume with those generated by the CHARM computer codes.* The preliminary comparison undertaken here suggests that the

UVPI Nihka data presents a spectral shape somewhat different from that of the reference spectrum. The experimental results indicate that the emission at wavelengths in the 220-320-nm range are greater, relative to the emission at longer wavelengths seen with the tracker camera, than is predicted by the reference model. These results are described in Section 7. The detailed comparison of reference predictions to the UVPI observations is a task for the modelers.

- *Provide radiometric measurements for nonplume, transient phenomena, if any.* Transients were seen in the Nihka data but were too short-lived or loosely correlated to the plume itself to allow measurement.

#### 9.2.2 Spatial Features

- *Obtain the length of the Nihka plume central regions.* The resolution limit of the PSF-corrected UVPI corresponds, at this range, to about 40 m, which is comparable to the expected plume length. Thus, an accurate measurement of the plume length was not possible, but (as described in Section 5.3) the observations are consistent with the predicted plume length.
- *Determine the shape of the shock boundary/mixing layer for different rocket velocities.* The profile of the radiance of the outer region appears consistent with a shock or mixing layer structure in the radiance and suggests that, as in the Strypi tests, a UV luminous outer region formed during the Nihka burn.
- *Identify asymmetries in plume shape and investigate possible causes.* No plume shape asymmetries were observed. The resolution limit of the UVPI at this range is such that only large asymmetries could have been detected.

#### 9.2.3 Temporal Features

- *Identify temporal trends in radiometrics and investigate possible dependence on rocket velocity and altitude.* The time behavior of the radiant intensity of the Nihka plume is described in Section 6. Radiance in the PC-1 band was observed to rise in the outer region as rocket altitude and velocity were increasing.
- *Investigate radiometric fluctuations to determine whether short-term variations in brightness are observed.* The statistics of the variations in plume radiant intensity are described in Section 6. Two peaks beyond the range of statistical likelihood were observed. The data were carefully analyzed, and no reason was found to reject them.
- *Identify changes with time in the shape of the plume's outer region.* The radiance profile remained fairly consistent during the Nihka burn.
- *Identify persistence and cumulative effects, if any, in plumes or nonplume phenomena.* No clouds or trails were observed in the Nihka test.

#### 9.2.4 Spectral Features

- *Compare the shape of the plume central region's emission spectrum within a filter bandpass with the reference spectral shape normalized to the tracker camera's measured emission values.* As described in Section 7, the UVPI data indicate that the decrease in spectral radiance and radiant intensity in the 220 to 320-nm band, relative to the tracker measured emission in the 255 to 450-nm band, is less than indicated by the reference model. This is similar to data from the Strypi and Starbird tests. A comparison of the UVPI data with data acquired by other sensors is currently in progress.
- *Relate tracker-camera measurement to visible and infrared measurements made by other sensors.* The UVPI acquired plume radiometric data to 450-nm wavelength. These radiant intensity values can be compared to data at longer wavelengths from other sensors as those data become available.
- *Characterize the emission spectrum for the plume's outer regions, if any.* A UV luminous outer region was found in the Nihka test data, as in the Strypi test. As for the Strypi, the outer region seemed to be luminous in the far UV rather than the near UV, or visible as seen by the tracker camera.

It is clear from the above that most of the objectives were achieved. However, the instrumental limitations in resolution, as well as the uncertainty in the reference spectral shape, complicate the extraction of precise values.

### 9.3 Conclusions

The UVPI observation of the Nihka plume was the first demonstration of the capability of the instrument for tracking and imaging missiles in flight from 450-km range. The bright plume of the Nihka stage was successfully tracked throughout its burn.

The Nihka stage was acquired for a total of 96 plume-camera images by using one UVPI filter. The spectral radiance and spectral radiant intensities were extracted from these images. Absolute values are necessarily obtained on the basis of an assumed spectral shape, namely, the reference spectrum, which is the spectrum of micron-sized alumina particles near their melting point of 2320 K. The results indicate that the reference shape is not inaccurate, but the new data suggest a stronger component in the far UV,  $\lambda < 320$  nm, than the model predicts. This was especially true for the total plume radiance, which indicates a UV luminous outer region. This result is similar to that obtained in the Strypi test.

Like the Strypi test, the images reveal a radiant plume with an identifiable outer region of UV radiance such as might be associated with a shock or mixing layer produced by the plume. The measured outer region radiance is strong in the far-UV and weaker in the near-UV and visible.

The time-dependence of the Nihka plume central region radiant intensity showed no pronounced trends or variations. The outer region, however, showed an upward ramp in time from ignition. This could correlate with either increasing rocket velocity or altitude or both.

The tracker camera obtained radiant intensity data in the 255 to 450-nm wavelength range. These data, taken with the plume camera data in the 220 to 320-nm range, support the conclusion that the central region spectrum is quite close to the reference model. A UV enhancement over the reference spectrum was seen in the total plume-camera field of view. This indicated a UV luminous outer region corresponding to a shock or mixing layer associated with the Nihka plume. A similar enhancement was seen in the Strypi data and was also associated with the outer region. It has been suggested that the Nihka's higher altitude allows great expansion of gaseous plume products into the far field where they can radiate in the far-UV, or they can react with atomic oxygen at high altitudes and produce the excess UV emissions.

This base of UV radiometric data is the foundation for further analysis to provide refined interpretations and evaluation. Comparison with models, with data from sensors on other platforms, and UVPI data from other tests will also yield improved radiometric results and an enhanced phenomenological understanding of UV emission by solid rocket motors in the upper atmosphere.

### ACKNOWLEDGMENTS

The successful observation of the Nihka rocket plume by the Ultraviolet Plume Instrument and preparation of the data was due to the efforts of many. Within the NRL LACE Program, engineering and testing personnel carefully prepared and tested the command sequence specified by the UVPI Encounter Manager (Richard Campion), revised it many times until it was satisfactory, and then successfully executed the sequence to obtain the Nihka data. Particular mention must be made of the efforts of Michael M. Horan, Robert J. Prescott, and Marianne Werz. The UVPI Encounter Manager was paralleled in all of his duties by Triet Tran to ensure that this first observation would be successful. LACE satellite operations personnel, directed by J.J. (Jeff) Devine, coordinated the transmission of delayed execution commands and pointing functions, the overall satellite operations during the observation, and the transmission of the data stored in the UVPI's memory. Data processing personnel then verified the quality of the transmitted data and prepared it for the image processing team. Particular mention must be made of the efforts of Kenneth D. Fields and Vincent G. Hickey. John E. Ivory and Dean Bakeris made accurate predictions of the attitude of the LACE satellite for use in the UVPI pointing function generation.

Joseph Nicholas of The Analytic Sciences Corporation served as the SDIO Science Manager for this observation. As such, he interacted with the Black Brant X launch and payload teams, identified the SDIO's objectives for this UVPI observation, and helped the UVPI Encounter Manager

specify the command sequence to achieve the SDIO's objectives. The management of the Black Brant X payload team held their launch for several minutes until the LACE satellite could get into position for the UVPI to observe the Nihka plume. The Navy Space Surveillance Center made a special calculation of the precision ephemeris for the LACE satellite needed for successful pointing of the UVPI. William Jeffrey, then with the Institute for Defense Analyses, provided CHARM code-generated predictions of the expected radiant intensity and radiance for comparison with the UVPI measurements.

In addition to these acknowledgments which are specific to the Nihka observation, some general acknowledgments are also in order. The Directed Energy Directorate of the Strategic Defense Initiative Organization (SDIO/TND) sponsored the NRL LACE Program, including the UVPI, in its entirety. Specific mention must be made of the supportive efforts of Col. Thomas Meyer, USAF, Col. William Browning, USAF, and Maj. David Dimiduk, USAF. Loral Electro Optical Systems designed and built the UVPI for NRL. Finally, acknowledgment is due to the outstanding efforts of many NRL and contractor personnel who designed, built, and tested the LACE satellite. Although so many were involved in the LACE satellite effort they cannot all be mentioned by name, Robert E. Palma, Program Manager for the NRL LACE Program, must be mentioned. Robert E. Palma has provided noteworthy management and sound technical guidance since the start of the program in 1985 and unwavering patience and moral support as the UVPI and its supporting data-processing capability slowly matured.

## REFERENCES

1. H.W. Smathers, D.M. Horan, J.G. Cardon, E.R. Malaret, M.R. Corson, and J.E. Brandenburg, "Ultraviolet Plume Instrument Description and Plume Data Reduction Methodology", NRL Report 9531, May 12, 1993.
2. H.W. Smathers, D.M. Horan, J.G. Cardon, E.R. Malaret, M. Singh, T. Sorensen, P.M. Laufer, M.R. Corson, J.E. Brandenburg, J.A. McKay, and R.R. Strunce, Jr., "UVPI Imaging From The LACE Satellite: The Strypi Rocket Plume" NRL Report 9526, July 15, 1993.
3. J.T. Wright, "Ultraviolet Plume Instrument (UVPI) Subsystem Users Manual," SDRL 068, Loral EOS Document No. 3731, Loral Electro Optical Systems, Pasadena, California, January, 1989.
4. H.W. Smathers, D.M. Horan, L.H. Reynolds, W. Ramsey and H.D. Wolpert, "Design and Description of the Ultraviolet Plume Instrument (UVPI)", *Proc. SPIE* **1158**, 196 (1989).
5. H.W. Smathers, G.R. Carruthers, W. Ramsey, G. Steiner and W. Louissaint, "Calibration and Performance of the Ultraviolet Plume Instrument (UVPI)", *Proc. SPIE* **1158**, 212 (1989).
6. J. Nicholas, "Experiment Requirements Document for UVPI Observations of SDIO Special Projects (SPFE) Launches Rev 3," The Analytic Sciences Corporation, Arlington, Virginia, August 1990.
7. W.A. Jeffrey, M. Slack and L. Laux, "Orbus Preflight Predictions", IDA document D-755, Institute for Defense Analyses, April, 1990.
8. J.A. Marqusee, "The State of Knowledge of UV/V Boost and Post-Boost-Phase Phenomenology and a Preliminary Assessment of Its Utility to SDI (U)", IDA Paper P-2232, Institute for Defense Analyses, Alexandria, Virginia, July 1989.
9. R.A. Reed and V.S. Calia, "Review of Rocket Particle Properties Research," Final Report AEDC-TR-89-11, Arnold Engineering Development Center, Tullahoma, Tennessee, November 1989.
10. K. Fukunaga, *Introduction to Statistical Pattern Recognition*, (Academic Press, 1972).

11. C.L. Wyatt, *Radiometric System Design* (MacMillan, New York, 1987).
12. F.E. Nicodemus "Normalization in Radiometry," *Applied Optics*, 12(12) 2960-2973 (1973).
13. J.A. Marqusee, Institute for Defense Analyses (private communication, 14 March 1991).
14. P.W. Erdman, E. Zipf, P. Espy, C. Howlett, D.A. Levin, and G.V. Candler, "In-Situ Measurements of UV and VUV Radiation from a Rocket Plume and Re-entry Bow Shock," AIAA Paper No. 92-0124, January 1992.
15. A. Papoulis, *Probability, Random Variables, and Stochastic Processes*, 2nd ed. (McGraw Hill, New York, 1984).
16. W.L. Wolfe and G.J. Zissis, editors, *The Infrared Handbook* (Environmental Research Institute of Michigan, 1978).
17. R.H. Kingston, *Detection of Optical and Infrared Radiation*, pp. 43-51 (Springer-Verlag, New York, 1978).
18. W. Jeffrey, Institute for Defense Analyses (private communication, August, 1992).
19. H.W. Smathers, D.M. Horan, J.G. Cardon, E.R. Malaret, L. Perez, T. Tran, J.E. Brandenburg, and R.R. Strunce, Jr., "UVPI Imaging From The LACE Satellite. The Starbird Rocket Plume", NRL Report 9546, August 18, 1993.

## Appendix A NIHKA TRAJECTORY PARAMETERS

The following tables present various Nihka trajectory related parameters as a function of time. The first column in each table is TALO, time after lift-off, in seconds. Table A1 shows the rocket's position in Earth center-fixed (ECF) coordinates and the rocket's speed. Table A2 shows the aspect angle and the distance between the satellite and the rocket. The aspect angle is defined as the angle between the line-of-sight (LOS) vector from the satellite to the target point and the longitudinal axis of the rocket. Table A3 shows the rocket's altitude, geodetic latitude, and longitude.

Table A1 - Rocket Position and Speed in ECF Coordinates

TALO (s)	XPOS (km)	YPOS (km)	ZPOS (km)	SPEED (km/s)
120.0	1358.162	-4963.924	3956.000	1.246
121.0	1359.095	-4964.609	3956.463	1.239
122.0	1360.019	-4965.264	3956.965	0.988
123.0	1360.872	-4965.654	3957.277	0.916
124.0	1361.700	-4965.956	3957.525	1.121
125.0	1362.590	-4966.483	3957.956	1.202
126.0	1363.507	-4967.107	3958.419	0.983
127.0	1364.363	-4967.509	3958.687	0.915
128.0	1365.193	-4967.815	3958.921	1.120
129.0	1366.084	-4968.342	3959.347	1.197
130.0	1366.996	-4968.944	3959.837	0.976
131.0	1367.845	-4969.316	3960.145	0.918
132.0	1368.679	-4969.633	3960.361	1.126
133.0	1369.578	-4970.187	3960.752	0.957
134.0	1370.423	-4970.543	3961.026	0.907
135.0	1371.249	-4970.833	3961.262	0.892
136.0	1372.070	-4971.100	3961.484	0.886
137.0	1372.889	-4971.360	3961.703	1.113
138.0	1373.783	-4971.895	3962.094	0.959
139.0	1374.633	-4972.266	3962.338	0.932
140.0	1375.491	-4972.552	3962.564	1.124
141.0	1376.393	-4973.072	3962.987	0.957
142.0	1377.239	-4973.416	3963.272	0.908
143.0	1378.067	-4973.701	3963.511	0.874
144.0	1378.866	-4973.997	3963.705	0.887
145.0	1379.684	-4974.288	3963.884	0.885
146.0	1380.503	-4974.555	3964.087	0.885
147.0	1381.322	-4974.814	3964.299	0.885
148.0	1382.141	-4975.070	3964.514	0.890
149.0	1382.966	-4975.348	3964.700	0.893
150.0	1383.794	-4975.633	3964.876	0.887
151.0	1384.616	-4975.898	3965.078	0.886
152.0	1385.436	-4976.155	3965.290	0.885
153.0	1386.256	-4976.411	3965.504	0.891
154.0	1387.082	-4976.688	3965.690	0.893
155.0	1387.910	-4976.972	3965.866	0.888
156.0	1388.733	-4977.236	3966.068	0.886
157.0	1389.554	-4977.494	3966.279	0.885
158.0	1390.374	-4977.749	3966.494	0.885

Table A1 - Rocket Position and Speed in ECF Coordinates (Cont'd)

TALO (s)	XPOS (km)	YPOS (km)	ZPOS (km)	SPEED (km/s)
159.0	1391.195	-4978.002	3966.709	0.867
160.0	1391.992	-4978.287	3966.895	0.749
161.0	1392.740	-4978.318	3966.867	0.827
162.0	1393.537	-4978.498	3967.001	0.840
163.0	1394.320	-4978.735	3967.190	0.901
164.0	1395.164	-4978.997	3967.367	0.921
165.0	1396.027	-4979.267	3967.540	0.764
166.0	1396.791	-4979.271	3967.537	0.806
167.0	1397.564	-4979.449	3967.680	0.833
168.0	1398.340	-4979.685	3967.872	0.735
169.0	1399.075	-4979.678	3967.876	0.829
170.0	1399.873	-4979.866	3967.991	0.872
171.0	1400.693	-4980.120	3968.143	0.750
172.0	1401.443	-4980.118	3968.134	0.827
173.0	1402.240	-4980.286	3968.274	0.846
174.0	1403.031	-4980.540	3968.435	0.747
175.0	1403.777	-4980.561	3968.398	0.879
176.0	1404.632	-4980.719	3968.530	0.964
177.0	1405.558	-4980.938	3968.688	1.019
178.0	1406.536	-4981.167	3968.854	0.960
179.0	1407.446	-4981.425	3969.023	1.122
180.0	1408.535	-4981.635	3969.193	1.342
181.0	1409.859	-4981.780	3969.363	1.367
182.0	1411.209	-4981.941	3969.504	1.579
183.0	1412.697	-4982.346	3969.838	1.683
184.0	1414.262	-4982.822	3970.236	1.798
185.0	1415.945	-4983.320	3970.626	1.887
186.0	1417.726	-4983.808	3971.013	1.968
187.0	1419.598	-4984.276	3971.399	2.073
188.0	1421.587	-4984.712	3971.785	2.334
189.0	1423.747	-4985.374	3972.374	2.504
190.0	1426.057	-4986.108	3973.001	2.462
191.0	1428.432	-4986.586	3973.437	2.674
192.0	1430.967	-4987.239	3973.982	2.771
193.0	1433.584	-4987.940	3974.564	2.830
194.0	1436.259	-4988.648	3975.158	2.850
195.0	1438.954	-4989.357	3975.756	2.831
196.0	1441.626	-4990.074	3976.355	2.825
197.0	1444.292	-4990.793	3976.954	2.824
198.0	1446.957	-4991.512	3977.553	2.824
199.0	1449.621	-4992.230	3978.152	2.662
200.0	1452.213	-4992.692	3978.548	2.767
201.0	1454.854	-4993.323	3979.079	2.775
202.0	1457.478	-4993.996	3979.685	2.655
203.0	1460.060	-4994.561	3979.932	2.771
204.0	1462.707	-4995.245	3980.383	2.785
205.0	1465.337	-4995.835	3981.083	2.812
206.0	1467.994	-4996.504	3981.715	2.823
207.0	1470.662	-4997.199	3982.324	2.665
208.0	1473.258	-4997.647	3982.723	2.771
209.0	1475.906	-4998.266	3983.254	2.784
210.0	1478.543	-4998.950	3983.829	2.627
211.0	1481.101	-4999.401	3984.216	2.492
212.0	1483.588	-4999.512	3984.336	1.522

Table A1 - Rocket Position and Speed in ECF Coordinates (Cont'd)

TALO (s)	XPOS (km)	YPOS (km)	ZPOS (km)	SPEED (km/s)
213.0	1485.106	-4999.417	3984.286	0.413
214.0	1485.518	-4999.389	3984.299	3.194
215.0	1488.536	-5000.118	3985.048	4.341

Table A2 - Rocket Aspect Angle and Range from Satellite

TALO (s)	Aspect Angle (deg)	Target Range (km)
120.0	83.000	640.638
121.0	82.730	635.848
122.0	82.460	631.072
123.0	82.180	626.325
124.0	81.820	622.223
125.0	81.540	617.539
126.0	81.250	612.885
127.0	80.950	608.281
128.0	80.580	604.323
129.0	80.280	599.770
130.0	79.980	595.252
131.0	79.670	590.767
132.0	79.290	586.966
133.0	78.980	582.578
134.0	78.660	578.207
135.0	78.260	574.534
136.0	77.940	570.243
137.0	77.530	566.661
138.0	77.200	562.454
139.0	76.860	558.315
140.0	76.440	554.875
141.0	76.110	550.863
142.0	75.750	546.772
143.0	75.330	543.542
144.0	74.960	539.548
145.0	74.530	536.394
146.0	74.170	532.562
147.0	73.730	529.490
148.0	73.360	525.762
149.0	72.910	522.805
150.0	72.530	519.220
151.0	72.070	516.382
152.0	71.690	512.878
153.0	71.230	510.164
154.0	70.830	506.778
155.0	70.370	504.229
156.0	69.970	500.967
157.0	69.500	498.514
158.0	69.090	495.378
159.0	68.630	493.062
160.0	68.220	490.058
161.0	67.730	487.878
162.0	67.250	485.824
163.0	66.830	482.984
164.0	66.350	481.031

Table A2 - Rocket Aspect Angle and Range from Satellite (Cont'd)

TALO (s)	Aspect Angle (deg)	Target Range (km)
165.0	65.940	478.471
166.0	65.460	476.669
167.0	64.970	474.947
168.0	64.540	472.480
169.0	64.050	470.915
170.0	63.560	469.432
171.0	63.150	467.292
172.0	62.670	465.972
173.0	62.190	464.736
174.0	61.770	462.788
175.0	61.290	461.740
176.0	60.820	460.791
177.0	60.420	459.126
178.0	59.970	458.431
179.0	59.580	456.961
180.0	59.120	456.349
181.0	58.800	455.238
182.0	58.390	454.953
183.0	58.070	453.993
184.0	57.760	453.108
185.0	57.460	452.321
186.0	57.180	451.715
187.0	56.910	451.117
188.0	56.660	450.693
189.0	56.420	450.292
190.0	56.270	449.245
191.0	56.070	449.093
192.0	55.890	449.019
193.0	55.790	448.299
194.0	55.640	448.360
195.0	55.560	447.779
196.0	55.410	447.957
197.0	55.340	447.489
198.0	55.200	447.785
199.0	55.150	447.443
200.0	55.020	447.857
201.0	54.900	448.402
202.0	54.860	448.174
203.0	54.750	448.757
204.0	54.690	449.856
205.0	54.630	449.514
206.0	54.540	450.278
207.0	54.540	450.438
208.0	54.460	451.318
209.0	54.400	452.332
210.0	54.400	452.599
211.0	54.350	453.729
212.0	54.300	454.834
213.0	54.180	456.784
214.0	53.850	458.485
215.0	53.550	460.360

Table A3 - Rocket Altitude, Geodetic Latitude and Longitude

TALO (s)	Altitude (km)	Longitude (deg)	Latitude (deg)
120.0	120.987	285.302	37.732
121.0	121.987	285.310	37.730
122.0	122.987	285.318	37.729
123.0	123.654	285.326	37.728
124.0	124.209	285.334	37.727
125.0	125.061	285.342	37.726
126.0	126.012	285.350	37.725
127.0	126.662	285.358	37.723
128.0	127.212	285.366	37.722
129.0	128.062	285.374	37.721
130.0	129.012	285.382	37.720
131.0	129.662	285.390	37.719
132.0	130.211	285.398	37.718
133.0	131.061	285.406	37.716
134.0	131.678	285.414	37.715
135.0	132.217	285.422	37.714
136.0	132.730	285.430	37.713
137.0	133.235	285.438	37.712
138.0	134.069	285.446	37.711
139.0	134.681	285.454	37.709
140.0	135.218	285.462	37.708
141.0	136.064	285.470	37.707
142.0	136.679	285.479	37.706
143.0	137.218	285.487	37.705
144.0	137.730	285.494	37.704
145.0	138.235	285.502	37.702
146.0	138.736	285.510	37.701
147.0	139.236	285.518	37.700
148.0	139.737	285.526	37.699
149.0	140.237	285.534	37.698
150.0	140.737	285.542	37.696
151.0	141.237	285.550	37.695
152.0	141.737	285.558	37.694
153.0	142.237	285.566	37.693
154.0	142.737	285.574	37.692
155.0	143.237	285.582	37.690
156.0	143.737	285.590	37.689
157.0	144.237	285.598	37.688
158.0	144.737	285.606	37.687
159.0	145.237	285.614	37.686
160.0	145.737	285.622	37.685
161.0	145.903	285.630	37.683
162.0	146.292	285.638	37.682
163.0	146.755	285.645	37.681
164.0	147.243	285.653	37.680
165.0	147.739	285.662	37.678
166.0	147.904	285.670	37.677
167.0	148.293	285.678	37.676
168.0	148.755	285.685	37.675
169.0	148.910	285.693	37.674
170.0	149.294	285.701	37.673
171.0	149.756	285.709	37.671
172.0	149.910	285.717	37.670
173.0	150.295	285.725	37.669

Table A3 - Rocket Altitude, Geodetic Latitude and Longitude (Cont'd)

TALO (s)	Altitude (km)	Longitude (deg)	Latitude (deg)
174.0	150.756	285.733	37.668
175.0	150.910	285.741	37.666
176.0	151.295	285.749	37.665
177.0	151.756	285.758	37.664
178.0	152.243	285.768	37.662
179.0	152.739	285.777	37.661
180.0	153.237	285.788	37.659
181.0	153.737	285.802	37.658
182.0	154.237	285.816	37.656
183.0	155.070	285.830	37.654
184.0	156.015	285.845	37.652
185.0	156.996	285.862	37.650
186.0	157.990	285.879	37.647
187.0	158.988	285.898	37.645
188.0	159.987	285.918	37.642
189.0	161.320	285.939	37.640
190.0	162.765	285.961	37.637
191.0	163.912	285.985	37.634
192.0	165.295	286.010	37.631
193.0	166.756	286.035	37.627
194.0	168.243	286.061	37.624
195.0	169.739	286.088	37.620
196.0	171.237	286.114	37.617
197.0	172.737	286.140	37.613
198.0	174.237	286.166	37.610
199.0	175.736	286.192	37.606
200.0	176.903	286.218	37.603
201.0	178.292	286.244	37.599
202.0	179.755	286.270	37.596
203.0	180.909	286.295	37.591
204.0	182.294	286.321	37.587
205.0	183.756	286.347	37.585
206.0	185.243	286.373	37.582
207.0	186.739	286.399	37.578
208.0	187.904	286.425	37.575
209.0	189.292	286.451	37.571
210.0	190.755	286.477	37.568
211.0	191.909	286.502	37.564
212.0	192.628	286.528	37.561
213.0	192.867	286.544	37.559
214.0	192.947	286.549	37.558
215.0	194.639	286.578	37.555

# **Appendix B** **TELEMETRY FRAMES AND CAMERA PARAMETERS**

UMT	Telemetry Frame	Filter	Tracker Exp. Time (ms)	Plume Exp. Time (ms)	Tracker Gain Step	Plume Gain Step
7:07:15.33	11603T	0	9.663	33.3	8	13
7:07:15.37	11604T	0	9.663	33.3	8	13
7:07:15.40	11605P	1	9.663	33.3	8	13
7:07:15.43	11606P	1	9.663	33.3	8	13
7:07:15.47	11607T	0	9.663	33.3	8	13
7:07:15.50	11608T	0	9.663	33.3	8	13
7:07:15.53	11609P	1	9.663	33.3	8	13
7:07:15.57	11610P	1	9.663	33.3	8	13
7:07:15.60	11611T	0	9.663	33.3	8	13
7:07:15.63	11612T	0	9.663	33.3	8	13
7:07:15.67	11613P	1	9.663	33.3	8	13
7:07:15.70	11614P	1	9.663	33.3	8	13
7:07:15.73	11615T	0	9.663	33.3	8	13
7:07:15.77	11616T	0	9.663	33.3	8	13
7:07:15.80	11617P	1	9.663	33.3	8	13
7:07:15.83	11618P	1	9.663	33.3	8	13
7:07:15.87	11619T	0	9.663	33.3	8	13
7:07:15.90	11620T	0	9.663	33.3	8	13
7:07:15.93	11621P	1	9.663	33.3	8	13
7:07:15.97	11622P	1	9.663	33.3	8	13
7:07:16.00	11623T	0	9.663	33.3	8	13
7:07:16.03	11624T	0	9.663	33.3	8	13
7:07:16.07	11625P	1	9.663	33.3	8	13
7:07:16.10	11626P	1	9.663	33.3	8	13
7:07:16.13	11627T	0	9.663	33.3	8	13
7:07:16.17	11628T	0	9.663	33.3	8	13
7:07:16.20	11629P	1	9.663	33.3	8	13
7:07:16.23	11630P	1	9.663	33.3	8	13
7:07:16.27	11631T	0	9.663	33.3	8	13
7:07:16.30	11632T	0	9.663	33.3	8	13
7:07:16.33	11633P	1	9.663	33.3	8	13
7:07:16.37	11634P	1	9.663	33.3	8	13
7:07:16.40	11635T	0	9.663	33.3	8	13
7:07:16.43	11636T	0	9.663	33.3	8	13
7:07:16.47	11637P	1	9.663	33.3	8	13
7:07:16.50	11638P	1	9.663	33.3	8	13
7:07:16.53	11639T	0	9.663	33.3	8	13
7:07:16.57	11640T	0	9.663	33.3	8	13
7:07:16.60	11641P	1	9.663	33.3	8	13
7:07:19.04	11714P	1	9.663	33.3	8	12
7:07:19.07	11715P	1	9.663	33.3	8	12
7:07:19.10	11716P	1	9.663	33.3	8	12
7:07:19.14	11717T	0	9.663	33.3	8	12
7:07:19.17	11718T	0	9.663	33.3	8	12
7:07:19.20	11719P	1	9.663	33.3	8	12

UMT	Telemetry Frame	Filter	Tracker Exp. Time (ms)	Plume Exp. Time (ms)	Tracker Gain Step	Plume Gain Step
7:07:19.24	11720P	1	9.663	33.3	8	12
7:07:19.27	11721P	1	9.663	33.3	8	12
7:07:19.30	11722P	1	9.663	33.3	8	12
7:07:19.34	11723P	1	9.663	33.3	8	12
7:07:19.37	11724P	1	9.663	33.3	8	12
7:07:19.40	11725P	1	9.663	33.3	8	12
7:07:19.44	11726P	1	9.663	33.3	8	12
7:07:19.47	11727T	0	9.663	33.3	8	12
7:07:19.50	11728T	0	9.663	33.3	8	12
7:07:19.54	11729P	1	9.663	33.3	8	12
7:07:19.57	11730P	1	9.663	33.3	8	12
7:07:19.60	11731P	1	9.663	33.3	8	12
7:07:19.64	11732P	1	9.663	33.3	8	12
7:07:19.67	11733P	1	9.663	33.3	8	12
7:07:19.70	11734P	1	9.663	33.3	8	12
7:07:19.74	11735P	1	9.663	33.3	8	12
7:07:19.77	11736P	1	9.663	33.3	8	12
7:07:19.80	11737T	0	9.663	33.3	8	12
7:07:19.84	11738T	0	9.663	33.3	8	12
7:07:19.87	11739P	1	9.663	33.3	8	12
7:07:19.90	11740P	1	9.663	33.3	8	12
7:07:19.94	11741P	1	9.663	33.3	8	12
7:07:19.97	11742P	1	9.663	33.3	8	12
7:07:20.00	11743P	1	9.663	33.3	8	12
7:07:20.04	11744P	1	9.663	33.3	8	12
7:07:20.07	11745P	1	9.663	33.3	8	12
7:07:20.10	11746P	1	9.663	33.3	8	12
7:07:20.14	11747T	0	9.663	33.3	8	12
7:07:20.17	11748T	0	9.663	33.3	8	12
7:07:20.20	11749P	1	9.663	33.3	8	12
7:07:20.24	11750P	1	9.663	33.3	8	12
7:07:20.27	11751P	1	9.663	33.3	8	12
7:07:20.30	11752P	1	9.663	33.3	8	12
7:07:20.34	11753P	1	9.663	33.3	8	12
7:07:20.37	11754P	1	9.663	33.3	8	12
7:07:20.40	11755P	1	9.663	33.3	8	12
7:07:20.44	11756P	1	9.663	33.3	8	12
7:07:20.47	11757T	0	9.663	33.3	8	12
7:07:20.50	11758T	0	9.663	33.3	8	12
7:07:20.54	11759P	1	9.663	33.3	8	12
7:07:20.57	11760P	1	9.663	33.3	8	12
7:07:20.60	11761P	1	9.663	33.3	8	12
7:07:20.64	11762P	1	9.663	33.3	8	12
7:07:20.67	11763P	1	9.663	33.3	8	12
7:07:20.70	11764P	1	9.663	33.3	8	12
7:07:20.74	11765P	1	9.663	33.3	8	12
7:07:20.77	11766P	1	9.663	33.3	8	12
7:07:20.80	11767T	0	9.663	33.3	8	12
7:07:20.84	11768T	0	9.663	33.3	8	12
7:07:20.87	11769P	1	9.663	33.3	8	12
7:07:20.90	11770P	1	9.663	33.3	8	12
7:07:20.94	11771P	1	9.663	33.3	8	12
7:07:20.97	11772P	1	9.663	33.3	8	12
7:07:21.00	11773P	1	9.663	33.3	8	12

UMT	Telemetry Frame	Filter	Tracker Exp. Time (ms)	Plume Exp. Time (ms)	Tracker Gain Step	Plume Gain Step
7:07:21.04	11774P	1	9.663	33.3	8	12
7:07:21.07	11775P	1	9.663	33.3	8	12
7:07:21.10	11776P	1	9.663	33.3	8	12
7:07:21.14	11777T	0	9.663	33.3	8	12
7:07:21.17	11778T	0	9.663	33.3	8	12
7:07:21.21	11779P	1	9.663	33.3	8	12
7:07:21.24	11780P	1	9.663	33.3	8	12
7:07:21.27	11781P	1	9.663	33.3	8	12
7:07:21.31	11782P	1	9.663	33.3	8	12
7:07:21.34	11783P	1	9.663	33.3	8	12
7:07:21.37	11784P	1	9.663	33.3	8	12
7:07:21.41	11785P	1	9.663	33.3	8	12
7:07:21.44	11786P	1	9.663	33.3	8	12
7:07:21.47	11787T	0	9.663	33.3	8	12
7:07:21.51	11788T	0	9.663	33.3	8	12
7:07:21.54	11789P	1	9.663	33.3	8	12
7:07:21.57	11790P	1	9.663	33.3	8	12
7:07:21.61	11791P	1	9.663	33.3	8	12
7:07:21.64	11792P	1	9.663	33.3	8	12
7:07:21.67	11793P	1	9.663	33.3	8	12
7:07:21.71	11794P	1	9.663	33.3	8	12
7:07:21.74	11795P	1	9.663	33.3	8	12
7:07:21.77	11796P	1	9.663	33.3	8	12
7:07:21.81	11797T	0	9.663	33.3	8	12
7:07:21.84	11798T	0	9.663	33.3	8	12
7:07:21.87	11799P	1	9.663	33.3	8	12
7:07:21.91	11800P	1	9.663	33.3	8	12
7:07:21.94	11801P	1	9.663	33.3	8	12
7:07:21.97	11802P	1	9.663	33.3	8	12
7:07:22.01	11803P	1	9.663	33.3	8	12
7:07:22.04	11804P	1	9.663	33.3	8	12
7:07:22.07	11805P	1	9.663	33.3	8	12
7:07:22.11	11806P	1	9.663	33.3	8	12
7:07:22.14	11807T	0	9.663	33.3	8	12
7:07:22.17	11808T	0	9.663	33.3	8	12
7:07:22.21	11809P	1	9.663	33.3	8	12
7:07:22.24	11810P	1	9.663	33.3	8	12

## Appendix C

### CHARM INPUT FILE FOR NIHKA

```

*** charm run identification :
*   path name to library & *.dft files           (a70)
*   header line                                   (a80)
DUB0:[CHARM.REV13]
charm rev1.3 NIHKA (orig charm.par)
*** run options :
*   include radiance transport calculations       (0 or 1)
*   include pixel map output:
*   0=no, 1=radiance, 2=transmission, 3=both      (0, 1, 2, 3)
*   monte carlo cpu time limit                   (seconds)
1 1 0
*** code selection :
*   intrinsic core - charm-ic                     (0, 1, 2)
*   continuum shock layer - charm-sl               (0, 1, 2)
*   2d transitional farfield - tramp              (0, 1, 2)
*   3d transitional farfield - chimera            (0, 1, 2)
*   free-molecular farfield - hapair              (0, 1, 2)
*   missile body                                  (0, 1, 2)
1 0 0 0 0 0
*** hard-body specifications :
*   number of hard-body segments                  (none)
*   last segment spherical cap? 0=no, 1=yes       (none)
*   beginning temperature of segment i           (k)
*   ending temperature of segment i              (k)
*   emissivity of segment i                      (none)
*   length of segment i                          (meters)
*   radius of segment i                          (meters)
*   half-angle of segment i                      (degrees)
0
*** engine/nozzle configuration :
*   engine library id number                     (none)
*   number of nozzles                            (none)
*   throat area                                  (m**2)
*   area ratio                                    (none)
*   nozzle lip angle                             (degrees)
*   nozzle divergence angle                      (degrees)
*   nozzle throat radius of curvature            (non-dimensional:rc/rt)
*   nozzle throat to exit length                 (non-dimensional:ze/rt)
0 1 0.00413 27.26 19.61 19.61 1.0 11.85
*** one-dimensional nozzle gas dynamics :
*   throat gas temperature                       (k)
*   throat gas pressure                          (atm)
*   throat gas velocity                          (m/s)
*   throat gas specific heat ratio               (none)
*   exit gas temperature                         (k)
*   exit gas pressure                            (atm)
*   exit gas velocity                            (m/s)

```

Best Available Copy

3253.8 29.2 1045.9 1.1712 1734.5 0.207 2835.2

\*\*\* one-dimensional nozzle chemistry :

\* specie name (none)  
 \* specie conc. at throat (mole fraction)  
 \* specie conc. at area ratio = 2.0 (mole fraction)  
 \* specie conc. at exit (mole fraction)

H2O 0.119696 0.123183 0.120896

CO2 0.012345 0.014207 0.017509

CO 0.227552 0.228606 0.226241

OH 0.005164 0.001736 0.000222

HCL 0.133173 0.138700 0.142045

HF 0.000000 0.000000 0.000000

O2 0.000093 0.000094 0.000094

H2 0.288700 0.297685 0.304112

N2 0.077808 0.078772 0.079078

H 0.031052 0.016157 0.010187

O 0.000336 0.000061 0.000006

AL2O3 0.081829 0.082825 0.083146

\*\*\* particulate conditions :

\* # particle bins (1 - 10)  
 \* particle radius in each bin (microns)  
 \* particle concentration in each bin (mass fraction)

5 1.0 2.0 3.0 4.0 5.0 .227 .36 .24 .113 .060

\*\*\* trajectory conditions :

\* trajectory id (1 - 99)  
 \* altitude (km)  
 \* velocity (m/sec)  
 \* angle of attack (degrees)  
 \* more trajectories (1 or 0)

1 155.0 1000. 0.0 0

\*\*\* atmospheric conditions for each trajectory condition :

\* atmospheric id number (>0 if table lookup)  
 \* ambient temperature (k)  
 \* ambient pressure (atm)  
 \* ambient density (kg/m\*\*3)  
 \* ambient specie concentrations (mole fraction)  
 \* for n2, o2, o, he, h, ar

1

\*\*\* sensor configuration for each trajectory condition :

\* bandpass - beginning (microns)  
 \* bandpass - ending (microns)  
 \* x sun position (none)  
 \* y sun position (none)  
 \* z sun position (none)  
 \* x earth position (none)  
 \* y earth position (none)  
 \* z earth position (none)  
 \* azimuth angle (degrees)  
 \* elevation angle (degrees)  
 \* image rotation angle (clockwise) (degrees)  
 \* x pixel resolution (m)  
 \* y pixel resolution (m)  
 \* # pixels in horizontal direction (none)  
 \* # pixels in vertical direction (none)  
 \* # pixels left of origin (none)  
 \* # pixels below origin (none)  
 \* image format binary or ascii (1 or 0)  
 \* does grid this trajectory (1 or 0)

Best Available Copy

0.277	0.320	0 0 0	0 0 0	56.0	0 0 5.	5.	100	100	10	50	0 1
0.245	0.277	0 0 0	0 0 0	56.0	0 0 5.	5.	100	100	10	50	0 1
0.220	0.245	0 0 0	0 0 0	56.0	0 0 5.	5.	100	100	10	50	0 0

## Glossary

### ABBREVIATIONS AND ACRONYMS

AOS	acquisition of signal
ARI	average radiant intensity
ASRI	average spectral radiant intensity
CCD	charge-coupled device
CHARM	Composite High Altitude Radiation Model
DN	digital number
FOV	field of view
FPA	focal plane array
FWHM	full-width-half-maximum
GMT	Greenwich Mean Time
HTPB	hydroxyl terminated polybutadiene
Hz	Hertz
K	degrees Kelvin
LACE	Low-power Atmospheric Compensation Experiment
LOS	loss of signal; line of sight
Mbps	megabits per second
MCP	microchannel plate
MHz	megaHz
NER	noise-equivalent radiance
NQE	net quantum efficiency
NRL	Naval Research Laboratory
PC-N	Plume camera filter, $N = 1, 2, 3, 4$
PE	photoevent
PSF	point spread function
RF	radio frequency
RMS	root mean square
RSI	Research Support Instruments
SDIO	Strategic Defense Initiative Organization
SR	steradian
TALO	time after lift-off
UMT	UVPI mission time
UV	ultraviolet
UVPI	Ultraviolet Plume Instrument
VAFB	Vandenberg Air Force Base
W	Watt